

Dissertation  
submitted to the  
Combined Faculties of the Natural Sciences and Mathematics  
of the  
Ruperto-Carola-University of Heidelberg, Germany  
for the degree of  
Doctor of Natural Sciences

Put forward by  
Sebastian Bock  
born in Neumünster, Germany  
Oral examination: 3rd February 2015



---

# **Non-Equilibrium Time Evolution of an Anderson Quantum Dot in the Kondo Regime**

---

**Referees: Prof. Dr. Thomas Gasenzer  
Prof. Dr. Selim Jochim**

Sebastian Bock  
Institut für Theoretische Physik  
Philosophenweg 16  
D-69120 Heidelberg  
Germany

*Supervisor*

---

Prof. Dr. Thomas Gasenzer  
Institut für Theoretische Physik  
Philosophenweg 16  
D-69120 Heidelberg  
Germany

# Abstract

In this thesis, we use a functional quantum field theoretical approach to investigate the non-equilibrium time evolution of an Anderson quantum dot with the main focus on the Kondo regime. We employ a real-time Keldysh path integral formulation to find an effective action. From the two-particle irreducible effective action, we derive, from the variational principle, the exact real-time Kadanoff–Baym equations of motion for the full propagator. We study these dynamic equations for the single impurity Anderson model, which describes a quantum dot coupled to two finite-temperature leads. We take the tunnelling to the leads into account exactly. In order to solve the Kadanoff–Baym equations numerically we have to approximate them. For this purpose, we make a non-perturbative approximation by summing an infinite number of Feynman diagrams in the direct (s)-, particle-particle (t)-, particle-hole (u)-, and stu-channels. The aim of our investigation is to analyse the non-equilibrium real-time evolution of the quantum dot after a hybridisation and interaction quench into its stationary state. The main focus is on the narrowing of the Kondo resonance and the formation of the Hubbard side bands. Following on from this, the main achievement is the transient, as well as the stationary electrical current, through the quantum dot and the investigation of the dependence on temperature and magnetic field. We compare our results with other methods, such as functional renormalisation group and iterative sum of path integrals, and find a very good agreement in most situations.

# Kurzzusammenfassung

In der vorliegenden Arbeit wird ein funktionaler quantenfeldtheoretischer Zugang verwendet, um die Nichtgleichgewichtszeitentwicklung eines Anderson-Quantenpunktes insbesondere im Kondo-Regime zu untersuchen. Es wird eine Pfadintegralformulierung unter Benutzung des Keldysh-Realzeitformalismus verwendet, um eine effektive Wirkung herzuleiten. Unter Verwendung des Variationsprinzips werden die exakten Kadanoff-Baym-Bewegungsgleichungen in Realzeit für den vollen Propagator aus der zweiteilchen-irreduziblen Wirkung abgeleitet. Die Bewegungsgleichungen werden für das single impurity Anderson-Modell, welches einen Quantenpunkt mit zwei angekoppelten Wärmebädern bei endlicher Temperatur beschreibt, untersucht. Die auftretenden Tunnelprozesse werden exakt berücksichtigt. Damit die Kadanoff-Baym-Gleichungen numerisch gelöst werden können, muss eine Näherung vorgenommen werden. Hierzu wird eine nichtstörungstheoretische Näherung gewählt, bei der eine unendliche Anzahl von Feynman-Diagrammen im Direkten (s)-, Teilchen-Teilchen (t)-, Teilchen-Loch (u)- und stu-Kanal aufsummiert wird. Das Ziel dieser Arbeit ist die Nichtgleichgewichts-Realzeitentwicklung eines Quantenpunktes nach einem Hybridisierungs- und Wechselwirkungsquench in seinen stationären Zustand zu untersuchen. Das Hauptaugenmerk liegt auf der Beobachtung der Verschmälerung der Kondo-Resonanz und der Bildung der Hubbard-Seitenpeaks. Darüber hinaus wird der transiente sowie der stationäre elektrische Strom durch den Quantenpunkt und dessen Abhängigkeit von Temperatur und Magnetfeld betrachtet. Die Ergebnisse werden mit anderen Methoden, wie der funktionalen Renormierungsgruppe und der iterativen Summierung von Pfadintegralen verglichen, wobei in den meisten Fällen eine sehr gute Überstimmung gefunden wird.

# Declaration by Author

This thesis is composed of my original work, and contains no material previously published or written by another person except where due reference has been made in the text. I have clearly stated the contribution by other authors to jointly-authored works that I have included in my thesis. The content of my thesis is the result of work I have carried out since the commencement of my graduate studies at the Heidelberg Graduate School of Fundamental Physics, Institut für Theoretische Physik, Universität Heidelberg and does not include material that has been submitted by myself to qualify for the award of any other degree or diploma in any university or other tertiary institution.





獻給  
慧



# Contents

<b>Abstract/Kurzzusammenfassung</b>	<b>v</b>
<b>Declaration by Author</b>	<b>vii</b>
<b>1 Introduction</b>	<b>1</b>
<b>2 Two-Particle Irreducible Effective Action Approach to Non-Equilibrium Quantum Field Theory</b>	<b>5</b>
2.1 Two-Point Green's Function . . . . .	6
2.1.1 Decomposing the Two-Point Green's Function into its Spectral and Statistical Components . . . . .	7
2.1.2 Schwinger–Keldysh Closed Time Path . . . . .	8
2.2 Non-Equilibrium Generating Functional . . . . .	10
2.3 Non-Equilibrium Two-Particle Irreducible Effective Action . . . . .	14
2.4 Exact Non-Equilibrium Dynamic Equation . . . . .	17
2.4.1 Exact Dynamic Equation for the Two-Point Green's Function . . . . .	18
2.4.2 Exact Dynamic Equations for the Statistical Propagator and the Spectral Function . . . . .	19
2.5 Thermal Equilibrium . . . . .	20
2.5.1 Fluctuation-Dissipation Relation . . . . .	22
2.6 Summary . . . . .	23
<b>3 Physical Background of Quantum Dots</b>	<b>25</b>
3.1 Quantum Dot . . . . .	25
3.2 Kondo Effect . . . . .	27
3.3 Single Impurity Anderson Model . . . . .	29
3.3.1 Hamiltonian and Action . . . . .	30
3.3.2 Phase Diagram . . . . .	31
3.4 Summary . . . . .	33
<b>4 Applying the Two-Particle Irreducible Effective Action to the Single Impurity Anderson Model</b>	<b>35</b>
4.1 Dynamic Equations for the Single Impurity Anderson Model . . . . .	36
4.2 Loop Expansion of the 2PI Effective Action . . . . .	36
4.2.1 Mean-Field or Hartree–Fock–Bogoliubov Approximation . . . . .	38
4.2.2 Second-Order Loop Expansion . . . . .	40
4.2.3 Third-Order Loop Expansion . . . . .	41

4.2.4	Higher-Order Loop Expansion . . . . .	43
4.3	Non-Perturbative Resummation of the 2PI Effective Action . . . . .	45
4.3.1	Hubbard–Stratonovich Transformation . . . . .	45
4.3.2	Direct (s)-Channel Resummation . . . . .	48
4.3.3	Particle-Particle (t)-Channel Resummation . . . . .	50
4.3.4	Particle-Hole (u)-Channel Resummation . . . . .	52
4.3.5	stu-Channel Resummation . . . . .	53
4.4	Implementing the Leads in the 2PI Formalism . . . . .	54
4.5	Electrical Current and Conductance . . . . .	59
4.6	Summary . . . . .	62
<b>5</b>	<b>Time Evolution of an Anderson Quantum Dot</b>	<b>65</b>
5.1	Numerical Implementation . . . . .	66
5.1.1	Initial Conditions . . . . .	66
5.1.2	Leads . . . . .	67
5.1.3	Kadanoff–Baym Equations of Motion . . . . .	67
5.1.4	Units . . . . .	69
5.2	Equilibrium Study of the Quantum Dot . . . . .	70
5.2.1	Occupation Number . . . . .	70
5.2.2	Spectral Function . . . . .	74
5.3	Non-Equilibrium Study of the Quantum Dot . . . . .	87
5.3.1	Transient Electrical Current . . . . .	87
5.3.2	Stationary Electrical Current and Conductance . . . . .	90
5.3.3	Temperature Dependence of the Stationary Electrical Current	94
5.3.4	Stationary Electrical Current and Conductance with a Mag- netic Field . . . . .	94
5.4	Summary . . . . .	96
<b>6</b>	<b>Conclusion</b>	<b>99</b>
<b>A</b>	<b>Numerical Methods</b>	<b>103</b>
A.1	Linear Multistep Methods for Solving Ordinary Differential Equations	103
A.1.1	Adams–Bashforth . . . . .	104
A.1.2	Adams–Moulton . . . . .	105
A.1.3	Predictor–Corrector . . . . .	105
A.2	Integration Methods . . . . .	106
A.2.1	Newton–Cotes . . . . .	106
A.2.2	Gaussian Quadrature . . . . .	107
<b>B</b>	<b>Effective Coupling</b>	<b>109</b>
B.1	Direct (s)-Channel . . . . .	110
B.2	Particle-Particle (t)-Channel . . . . .	111
B.3	Particle-Hole (u)-Channel . . . . .	112

<b>C Energy Conservation of an Isolated Quantum Dot</b>	<b>113</b>
C.1 Mean Field . . . . .	115
C.2 Second Order . . . . .	115
C.3 Direct (s)-Channel . . . . .	116
C.4 Particle-Particle (t)-Channel . . . . .	117
C.5 Particle-Hole (u)-Channel . . . . .	118
<b>Bibliography</b>	<b>119</b>
<b>Danksagung</b>	<b>135</b>



# Chapter 1

## Introduction

The substantial progress in nanotechnology over the last five decades has confirmed Richard Feynman's belief about this branch of physics, as expressed in the famous quotation:

“There's plenty of room at the bottom.”<sup>1</sup>

Since then it has been managed to shrink the dimensions of bulk materials to two-dimensional quantum wells by confining the material along one axis, such that the size of the material is smaller than the de Broglie wavelength of an electron in this direction. Furthermore, one-dimensional quantum wires and zero-dimensional quantum dots are feasible and have been of large scientific interest in the last twenty years. Due to the confinement in all directions, quantum dots, also referred to as artificial atoms, have a discrete and high density of states which gives rise to important electronic and optical properties. This can be exploited in a myriad of applications such as solar cells [1–3], lasers [4–6], displays [7], DNA nanosensors [8], biological tagging [9], and for medical diagnostics in general. Consequently, nanotechnology, and in particular quantum dots, have become an interdisciplinary research topic; as have quantum information and quantum computation. A quantum dot is manageable to prepare [10], control and manipulate [11–14], and its state can be read [15–17]. Hence, quantum dots meet most of DiVincenzo's criteria [18] and therefore are a promising candidate for building quantum computers as proposed in Ref. [19]. Due to the wide range of applications, nanotechnology will undoubtedly change our daily lives in the near future.

In 1961, the Anderson model [20] was introduced to explain the formation of magnetic moments in bulk metals with magnetic impurities. The limitation to a single impurity, the so-called single impurity Anderson model (SIAM), also perfectly describes the physics of quantum dots coupled to finite-temperature leads. The SIAM is the standard model<sup>2</sup> for quantum impurities and is of fundamental interest

---

<sup>1</sup>In 1959, Richard Feynman gave a talk entitled “Plenty of Room at the Bottom” at the California Institute of Technology.

<sup>2</sup>Besides the SIAM, there is also the resonant level model (RLM), which is a special case of the SIAM for vanishing on-site interaction,  $U = 0$ ; the interacting resonant level model (IRLM), which describes a single level on the quantum dot interacting with the nearest lead electrons; and the Anderson-Holstein model (AHM), which extends the SIAM by an additional interaction of phonons and electrons on the quantum dot.

in understanding the low temperature behaviour of quantum dots. At first sight, the SIAM looks rather simple, yet it exhibits a variety of interesting phenomena. The interplay of the on-site Coulomb repulsion and the coupling to a sea of fermions, represented by finite-temperature leads, gives rise to non-trivial many-body dynamics, such as the Kondo effect for large on-site interaction strength and low temperatures  $T < T_K$ ; where the Kondo temperature,  $T_K$ , is a characteristic energy scale of the system, see Ch. 3. The Kondo temperature depends exponentially on the interaction strength and therefore, the Kondo physics is hard to access. The first measurements of the Kondo effect in quantum dots [21–23] were realised in 1998. From the theoretical perspective, the SIAM has been studied for many years, however only the thermodynamic properties in equilibrium are known exactly from the Bethe ansatz [24–28]. Furthermore, dynamical properties of the spectral function in equilibrium are well understood, but the precise time evolution from a given initial state to the stationary state is not yet known. Moreover, when the quantum dot is driven by a finite bias voltage, due to different chemical potentials of the leads, the stationary electrical current for large bias voltages beyond the linear response regime is still being researched. Therefore, the SIAM is ideal for studying the non-equilibrium charge transport through quantum dots. Since the first realisation of quantum dots coupled to finite-temperature leads in experiments two decades ago, the SIAM has attracted a lot of attention. Due to available experimental data and the tunability of all relevant parameters in quantum dots, the SIAM has become a playground for testing new theoretical methods. Thus, there has been a tremendous effort to study the SIAM in and out of equilibrium.

The stationary properties of the SIAM were investigated by employing simple perturbative methods, such as the mean-field approximation of the one-particle non-equilibrium Green’s function (NEGF) [29] and an extension to the second-order expansion in the coupling constant [30]. Furthermore, Fermi liquid theory [31, 32], a self-consistent perturbation theory for NEGF [33], which makes use of a Ward identity, was applied and also the integrability of the SIAM [34] was exploited. In addition to this, calculations using a renormalised perturbation theory [35–38] were carried out. Moreover, various renormalisation group (RG) methods were employed to impurity models, such as the perturbative renormalisation group (PRG) [39–42], numerical renormalisation group (NRG) [43–52] based on the Wilson RG [53], functional renormalisation group (FRG) [54–58] and its extension to non-equilibrium [59–65]. The Bethe–Salpeter equation in the parquet approximation [66] was used to tackle the SIAM in the Kondo regime [67–69]. Besides this, the slave boson approach [70–74], full counting statistics (FCS) [75, 76], and Chebyshev expansion using matrix product states [77] were used to study quantum impurity models.

All the aforementioned methods either cannot access the time evolution of the SIAM or this was not performed in the cited references. In recent years, methods which are naturally not able to tackle the time evolution, were improved and can now yield time-dependent results such as the time-dependent density matrix renormalisation group (tDMRG) [78–84], the time dependent NRG [85–89], and the real-time renormalisation group [90–92]. There are also real-time Monte-Carlo [93–95] and



iterative sum of path integrals (ISPI) approaches [96–98], which make the calculation of time-dependent correlation functions possible. Recently, other not so popular methods, such as the Gutzwiller approach [99], excitation states [100, 101], and influence functional path integral (INFPI) [102] were employed to quantum impurity models.

In this thesis, we employ the two-particle irreducible (2PI) effective action, also known Luttinger–Ward functional and  $\phi$ -derivable [103–105], to investigate the non-equilibrium time evolution of the SIAM. The effective action allows us to derive, via the variational principle, an exact equations of motion for the NEGF, the so-called Kadanoff–Baym equations of motion, see Ch. 2. In order to find numerical solutions to these equations, one must approximate the self-energy of the NEGF, or equivalently the 2PI effective action. A non-perturbative resummation of a certain type of Feynman diagram to all orders, so-called channel resummation, is commonly used for an approximation. The 2PI effective action has successfully described the dynamics, as well as the thermalisation, of relativistic Bose systems [106–115], non-relativistic Bose gases in the context of Bose–Einstein condensates [116–121], relativistic fermionic quantum fields [122–124] and also non-relativistic Fermi gases [125–127]. However, in these fields, the 2PI effective action approach misses key benchmarks from exact results, other methods or even experimental data for strongly coupled systems. In the SIAM, the situation is different. Data obtained from other methods, numerical as well as exact analytic results and experimental data, are available for the stationary state of the quantum dot. Hence, the SIAM is an ideal system to benchmark the 2PI effective action for finding a range of validity. This is one key motivation for this thesis. In Ref. [128], a real time renormalisation group was proposed and extended in Ref. [129], which yields similar equation as in the 2PI effective action.

An equivalent approach is the so-called GW approximation [130, 131] of the NEGF, where additionally a certain type of Feynman diagram are resummed. Usually, it is carried out in Fourier space to calculate the stationary properties directly; as performed in Refs. [132–136] for the SIAM. For real-time calculation, the Kadanoff–Baym equation of motion must also be solved. Due to the complexity of this equation, in most cases the generalised Kadanoff–Baym ansatz (GKBA) [137] is applied, which simplifies the equation and reduces the computational time from cubic to quadratic. The GKBA was recently employed to carrier dynamics of semiconductors [138, 139], optical absorption spectra [140], quasiparticle spectra and excited Hubbard clusters [141–143], as well as the SIAM [144]. To our knowledge, the Kadanoff–Baym equation of motion for the NEGF, which is the starting point of this thesis, was used for the first time in Ref. [145] to calculate the time evolution of the SIAM and used also a few months later also in Ref. [146]. There are comparative studies for Fourier space calculations [48, 147, 148] and also real time [145, 146].

## Aims and Achievements of the Thesis

The first aim of this thesis is to investigate the time evolution of the equilibrium (equal chemical potentials of the leads) spectral function of the quantum dot into the stationary state. The quantum dot is set to a specific state at the initial time and will be coupled immediately to the leads, which is called hybridisation quench. The stationary equilibrium spectral function has been studied in detail in recent years with various methods [30, 43–45, 47, 51, 52, 56, 61, 62, 65, 67–69, 77, 87, 88, 149] and therefore, the stationary spectral function of the quantum dot is known. Thus, we can compare the stationary spectral function of the time evolution of the system obtained from the 2PI effective action to the known results. The main challenge with the spectral function is the width of the resonance, which narrows exponentially with increasing interaction strength. We find a range where we can render this feature correctly. Moreover, we present the whole time evolution of the spectral function to observe the build-up of the Kondo resonance and the Hubbard side bands, which goes beyond what is already discussed in the literature. For more detail, we refer to Sec. 5.2.2.

The second aim is to investigate the non-equilibrium charge transport through the quantum dot, especially beyond the linear response regime. In this range, even the stationary current is not yet well understood. The stationary current was investigated in Refs. [82, 98, 145, 148, 150, 151]. In addition to this, we are also interested in the transient current of the SIAM, which is so far not well researched, see Refs. [102, 145, 146, 150–152]. We study the transient electrical current through the quantum dot up to large bias voltages. Additionally, we compare the stationary results with the functional renormalisation group (FRG) and iterative sum of path integrals and find a very good agreement in the whole range for small to intermediate interaction strengths. For larger interaction strength, the deviation compared to the results of FRG becomes visible. However, we obtain the correct results in the limit of large bias voltages for the electrical current for all probed interaction strengths. More information can be found in Sec. 5.3.

The third aim of this thesis is to find out what can be achieved with this method. We will compare our results with other well-established methods and, when applicable, also with exact analytic results. We use different channel resummations for a non-perturbative approximation of the self-energy. Besides the established direct (s)-, particle-particle (t)-, and particle-hole (u)-channel resummations, we define the stu-channel resummation as a sum of these channel resummations and compare the results of each of them. This has not been carried out so far. From this analysis, we can estimate which diagrams are more important for the investigation of the SIAM in the Kondo regime. We obtain the best results for the stu-channel resummation approximation.

## Chapter 2

# Two-Particle Irreducible Effective Action Approach to Non-Equilibrium Quantum Field Theory

In this chapter, we put this thesis on a sound theoretical footing by introducing the theoretical concepts used to obtain the results we present in Ch. 5. In this thesis, we use the two-particle irreducible (2PI) effective action approach to non-equilibrium quantum field theory which is a well-established method, in particular in the fields of high energy physics and ultra-cold quantum gases, to derive an exact dynamic equation for the two-point correlation function. In describing the theoretical foundations, we make use of the formulation as layed out in Refs. [127, 153, 154].

We want to describe quantum dots at low temperatures, which means we can assume a non-relativistic system, which is well described without any space coordinates due to its smallness, see Ch. 3. These are the only assumptions we impose in this chapter. The extension to an arbitrary number of spatial dimensions is straightforward but not needed for the purposes of the present work. Apart from that, the entire derivation of the dynamic equations is universally valid for all interacting theories. Later in Ch. 3, we specify the model Hamiltonian for an Anderson quantum dot and in Ch. 4 we derive all relevant equations for the specific Hamiltonian for different approximations.

We are interested in the time evolution of experimentally accessible observables which can be extracted from the lowest order correlation functions as occupation number and electrical current. In the case of fermions, there is no macroscopic field because of the Pauli exclusion principle, which means the one-point function vanishes. Hence, at the beginning of this chapter, we introduce the two-point Green's function and its decomposition into the statistical propagator and spectral function.

The main goal of this chapter is the derivation of exact dynamic equations for the two-point Green's function, the so-called Kadanoff–Baym equations of motion [104, 155]. In the first instance, we use a real time path integral formulation along the Schwinger–Keldysh closed time path [156–160] to introduce a non-equilibrium generating functional for  $2n$ -point correlation functions. This generating functional includes the initial density matrix, which encodes the initial conditions of the system. In this thesis, we use Gaussian initial conditions, which means we specify the initial

correlation up to two-point correlation functions. This choice of initial conditions is not an approximation to the dynamics of the system and allows us to write the generating functional in a compact form. As an intermediate step, we introduce the Schwinger functional for generating connected  $2n$ -point correlation functions. With a Legendre transform with respect to the two-point source term we arrive at the 2PI effective action, which incorporates all statistical as well as quantum fluctuations. In analogy to the action in classical mechanics, we can derive with the variational principle an exact dynamic equation for the two-point Green's function, which includes an integration along the Schwinger–Keldysh contour. We use the decomposition into the statistical propagator and spectral function to convert the dynamic equation into a set of coupled integro-differential equations with ordinary time derivatives and integrals.

At the end of this chapter, we look at the special case of thermal equilibrium. In thermal equilibrium, the density matrix is given by a canonical or grand-canonical ensemble. In this case, the Schwinger–Keldysh closed time path is extended by a strip along the imaginary time axis determined by the temperature of the system. From the periodicity conditions, so-called Kubo–Martin–Schwinger conditions [161, 162], of this time path we can derive a relation between the statistical propagator and the spectral function.

## 2.1 Two-Point Green's Function

With our theoretical tools, we want to investigate real physical situations, and hence, we are interested in the time evolution of observables, *e.g.* the occupation number or the electrical current. Most of the experimentally accessible observables are encoded in the lowest correlation functions. Since there is no macroscopic fermionic field, the one-point function is vanishing and the lowest non-trivial correlation function is the two-point Green's function<sup>1</sup>.

The definition of the two-point Green's function or propagator is given by the time-ordered expectation value of two fermionic field operators at two points in time

$$D_{\alpha\beta}(t, t') = \langle \mathcal{T}_{\mathcal{C}} \Psi_{\alpha}(t) \Psi_{\beta}^{\dagger}(t') \rangle, \quad (2.1)$$

where  $\langle \cdot \rangle$  denotes the expectation value,  $\Psi$  an annihilation and  $\Psi^{\dagger}$  a creation field operator, and  $\mathcal{T}_{\mathcal{C}}$  is the time ordering operator along the Schwinger–Keldysh contour  $\mathcal{C}$ . We shift the discussion of the Schwinger–Keldysh contour to Subsec. 2.1.2 and in Sec. 2.2 we introduce a path integral representation for the expectation value. The index of a field operator describes, in general, its quantum numbers which depend on the system under consideration. We are interested in the non-equilibrium time evolution of an Anderson quantum dot, thus the index specifies the spin orientation of an electron,  $\alpha \in \{\uparrow, \downarrow\}$ . The Heisenberg field operators have the same properties

---

<sup>1</sup>“Correlation function” and “Green's function” are used interchangeably. In the special case of a two-point function, we also call it a propagator.

as Graßmann numbers<sup>2</sup>, therefore the time ordering of the two field operators reads

$$\mathcal{T}_C \Psi_\alpha(t) \Psi_\beta^\dagger(t') = \begin{cases} \Psi_\alpha(t) \Psi_\beta^\dagger(t') & \text{if } t > t' \\ -\Psi_\beta^\dagger(t') \Psi_\alpha(t) & \text{if } t < t' \end{cases}, \quad (2.2)$$

with an additional minus sign in the second case,  $t < t'$ . With this definition, we can rewrite the two-point Green's function in Eq. (2.1) with the help of the Heaviside step function as

$$D_{\alpha\beta}(t, t') = \langle \Psi_\alpha(t) \Psi_\beta^\dagger(t') \rangle \theta_C(t - t') - \langle \Psi_\beta^\dagger(t') \Psi_\alpha(t) \rangle \theta_C(t' - t). \quad (2.3)$$

In the case of fermions, the two-point correlation function is always connected because of the vanishing one-point function. The situation alters for higher  $n$ -point functions and there is a difference between full and connected  $n$ -point functions.

The definition of the propagator has a drawback because at equal times, in general, it has a jump discontinuity<sup>3</sup>, which is visible from Eq. (2.2). Both limits do exist but are not the same and the value at equal times is not defined. Such discontinuities can cause trouble and are not always easy to handle, especially in numerical calculations. Fortunately, there is a way to circumvent this problem by making this jump discontinuity explicit in what we are doing next.

### 2.1.1 Decomposing the Two-Point Green's Function into its Spectral and Statistical Components

We want to reformulate the propagator in terms of new functions which are continuous. We start from Eq. (2.3) and use the identity  $\text{sgn}_C(t) = 2\theta_C(t) - 1$ . We find

$$D_{\alpha\beta}(t, t') = \frac{1}{2} \langle [\Psi_\alpha(t), \Psi_\beta^\dagger(t')] \rangle - \frac{i}{2} \text{sgn}_C(t - t') i \langle \{ \Psi_\alpha(t), \Psi_\beta^\dagger(t') \} \rangle, \quad (2.4)$$

where  $[\cdot, \cdot]$  indicates the commutator and  $\{\cdot, \cdot\}$  the anti-commutator. We introduce the definition of the statistical propagator,  $F$ , and spectral function<sup>4</sup>,  $\rho$ ,

$$\begin{aligned} F_{\alpha\beta}(t, t') &= \frac{1}{2} \langle [\Psi_\alpha(t), \Psi_\beta^\dagger(t')] \rangle, \\ \rho_{\alpha\beta}(t, t') &= i \langle \{ \Psi_\alpha(t), \Psi_\beta^\dagger(t') \} \rangle. \end{aligned} \quad (2.5)$$

With these definitions, we can write the two-point Green's function in Eq. (2.1) in terms of the statistical propagator,  $F$ , and spectral function,  $\rho$ ,

$$D_{\alpha\beta}(t, t') = F_{\alpha\beta}(t, t') - \frac{i}{2} \text{sgn}_C(t - t') \rho_{\alpha\beta}(t, t'). \quad (2.6)$$

<sup>2</sup>Graßmann numbers make up the Graßmann algebra. Graßmann numbers are complex numbers that anti-commute with each other but commute with ordinary numbers. Let  $\theta_i$  and  $\theta_j$  denote two Graßmann variables. It follows that  $\{\theta_i, \theta_j\} = 0$  and  $(\theta_i)^2 = 0$ .

<sup>3</sup>In mathematics, singularities are divided into two types. Type I embraces the removable and jump discontinuity and type II contains the infinite discontinuity and essential singularity.

<sup>4</sup>The terms “statistical propagator” and “spectral function” are special for the propagator. We can also decompose, for example, the self-energy in the same way. For this and other functions, we use the terms statistical and spectral “part” or “component”.

Both the statistical propagator,  $F$ , and spectral function,  $\rho$ , are continuous at equal times  $t = t'$ , since the discontinuity is pulled out explicitly in the sign function.

With the decomposition of the two-point Green's functions in Eq. (2.6), the time-ordering operator does not appear in the statistical propagator,  $F$ , nor in the spectral function,  $\rho$ . In a path integral formulation, which we will introduce later, we cannot directly compute these expectation values because a path integral is inherently time ordered. However, with the Björken–Johnson–Low theorem [163, 164] it is possible to evaluate expectation values of equal-time anti-commutators of Grassmann field operators, which is consistent with the canonical quantisation. Therefore, we obtain for the spectral function,  $\rho$ , at equal times,

$$\rho_{\alpha\beta}(t, t) = i\delta_{\alpha\beta}. \quad (2.7)$$

The statistical propagator,  $F$ , is connected to the occupation number for equal field components by

$$F_{\alpha\alpha}(t, t) = \frac{1}{2} - n_{\alpha}(t), \quad (2.8)$$

with the definition for the occupation number  $n_{\alpha}(t) = \langle \psi_{\alpha}^{\dagger}(t)\psi_{\alpha}(t) \rangle$ . From these definitions, we also find symmetry relations for the statistical propagator,  $F$ , and spectral function,  $\rho$ :

$$F_{\alpha\beta}(t, t') = F_{\beta\alpha}^*(t', t), \quad \rho_{\alpha\beta}(t, t') = -\rho_{\beta\alpha}^*(t', t). \quad (2.9)$$

## 2.1.2 Schwinger–Keldysh Closed Time Path

In this section, we want to introduce the Schwinger–Keldysh closed time path invented by Schwinger [157], Bakshi [158, 159], Mahanthappa [160] and Keldysh [156]. So far, it has just been a label attached to operators but now we will give it a meaning. The basic idea comes from using the trace to calculate expectation values of operators. Hence, we write the expectation value of two field operators in the Schrödinger picture with the help of time evolution operators,  $\mathcal{U}(t, t') = \mathcal{T}_C \exp\left(-i \int_t^{t'} H(z) dz\right)$ . We obtain

$$\langle \mathcal{T}_C \psi_{\alpha}(t)\psi_{\beta}^{\dagger}(t') \rangle = \langle \mathcal{T}_C \mathcal{U}(t_0, t)\psi_{\alpha}\mathcal{U}(t, t')\psi_{\beta}^{\dagger}\mathcal{U}(t', t_0) \rangle. \quad (2.10)$$

From this, where we have the time dependence in the time evolution operators, it is clearly visible that it starts at time  $t_0$ , runs to time  $t$ , goes further to time  $t'$ , and then back to the initial time  $t_0$ . This describes a closed time path which we also show graphically in Fig. 2.1. We can split this time path into the forward,  $\mathcal{C}^+$ , and the backward branch,  $\mathcal{C}^-$ . Typically, the maximum time of the closed time path is given by the latest time of the operator appearing in the expectation value but we can also push this time to infinity. This is possible since the contribution from times later than the maximum time of the operators on both branches must cancel each other due to causality or, in terms of time evolution operators,  $\mathcal{U}(t', t'')\mathcal{U}(t'', t') = 1$ .

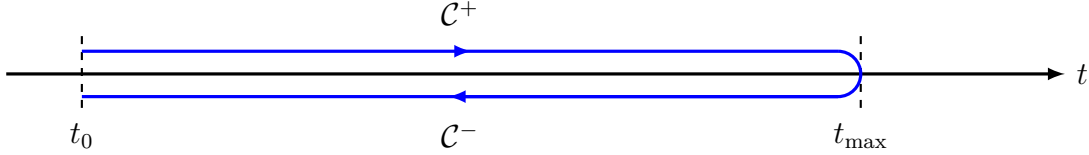


**Figure 2.1:** The closed time path or Schwinger–Keldysh contour consists of the forward,  $\mathcal{C}^+$ , and backward branch,  $\mathcal{C}^-$ . The Schwinger–Keldysh contour starts at an initial time  $t_0$  and goes to the maximum time  $t_{\max}$  occurring in the arguments of the operators. This time can also be pushed to infinity. Due to causality, all contributions later than  $t_{\max}$  must cancel each other on the forward and backward branch. The contour in the illustration is only shifted from the real time axis for clarity.

This closed time path translates to integrals along this time contour as

$$\int_{\mathcal{C}} dt = \int_{\mathcal{C}^+} dt + \int_{\mathcal{C}^-} dt, \quad (2.11)$$

where the integral along the forward,  $\mathcal{C}^+$ , and backward branch,  $\mathcal{C}^-$ , is given by

$$\int_{\mathcal{C}^+} dt = \int_{t_0}^{t_{\max}} dt, \quad \int_{\mathcal{C}^-} dt = \int_{t_{\max}}^{t_0} dt. \quad (2.12)$$

In the introductory example in Eq. (2.10), we tacitly assumed that both times of the operators lie on the forward branch. However, we can generalise it to both branches. Thus, in the case of a two-point correlation function, there are four possibilities depending on where the times are located on the Schwinger–Keldysh contour. The time ordering operator on this contour is defined as the standard time ordering if both times lie on the forward branch and anti time ordering on the backward branch. Times on the backward branch are always considered later than times on the forward branch. Therefore, the sign function on the Schwinger–Keldysh contour is the ordinary sign function if both times are on the forward branch and it gets an additional minus sign on the backward branch. The propagator in the decomposition of Eq. (2.6) reads

$$\begin{aligned} D_{\alpha\beta}^{++}(t, t') &= F_{\alpha\beta}(t, t') - \frac{i}{2}\rho_{\alpha\beta}(t, t') \operatorname{sgn}(t - t'), \\ D_{\alpha\beta}^{--}(t, t') &= F_{\alpha\beta}(t, t') + \frac{i}{2}\rho_{\alpha\beta}(t, t') \operatorname{sgn}(t - t'), \\ D_{\alpha\beta}^{+-}(t, t') &= F_{\alpha\beta}(t, t') + \frac{i}{2}\rho_{\alpha\beta}(t, t'), \\ D_{\alpha\beta}^{-+}(t, t') &= F_{\alpha\beta}(t, t') - \frac{i}{2}\rho_{\alpha\beta}(t, t'), \end{aligned} \quad (2.13)$$

where the  $\pm$  labels on the propagator  $D$  on the left hand side indicate whether the times in the argument are considered on the forward or backward branch of the Schwinger–Keldysh contour.

We point out that the introduction of the closed time path is artificial and is made only for technical reasons. This formalism provides us with a convenient way to get all correlation functions that are needed to describe non-equilibrium physical situations. From Eq. (2.13), we see that not all of these four propagators are linearly independent of one another because of

$$D_{\alpha\beta}^{++}(t, t') + D_{\alpha\beta}^{--}(t, t') = D_{\alpha\beta}^{+-}(t, t') + D_{\alpha\beta}^{-+}(t, t'). \quad (2.14)$$

Due to this fact, in literature, a Schwinger–Keldysh rotation is often used to get rid of one of the four propagators and the retarded  $D^R$ , advanced  $D^A$ , and Schwinger–Keldysh propagator  $D^K$  are introduced as a linear combination of the propagators in Eq. (2.13). Also the remaining three propagators are not completely independent of each other and there is a relation between the retarded and advanced ones. Hence, we only need two independent functions to describe the non-equilibrium physics, which in our case are the statistical propagator,  $F$ , and the spectral function,  $\rho$ . We can consider equilibrium as a special case of non-equilibrium. In this special case, we derive a universal relation between the statistical propagator,  $F$ , and the spectral function,  $\rho$ , see Subsec. 2.5.1. Thus, in equilibrium, only one propagator is needed and in non-equilibrium there are more degrees of freedom.

## 2.2 Non-Equilibrium Generating Functional

In non-equilibrium physics, we are interested in time-dependent correlation functions. For that, we use expectation values of Heisenberg field operators. The dynamics of the system is not only determined by the model Lagrangian but also by its initial conditions encoded in an initial density matrix at time  $t_0$ . The expectation values of time ordered Heisenberg field operators are given by the trace over them together with the initial density matrix as

$$\langle \cdot \rangle = \text{Tr} [\rho(t_0) \cdot]. \quad (2.15)$$

To evaluate this trace we need a complete set of states at the initial time  $t_0$ . A reasonable choice for this are eigenstates of the Heisenberg annihilation field operator  $\Psi_\alpha(t_0)$ ,

$$\Psi_\alpha(t_0) |\psi_0^{(\pm)}\rangle = \psi_{0,\alpha}^{(\pm)} |\psi_0^{(\pm)}\rangle, \quad (2.16)$$

where  $|\psi_0^{(\pm)}\rangle$  denotes the eigenstates, so-called coherent states, and  $\psi_{0,\alpha}^{(\pm)}$  are the corresponding eigenvalues. Here,  $\pm$  are only labels, so both sets are the same. We take these set of states to perform the trace for two Heisenberg field operators, after which it reads

$$\begin{aligned} \langle \mathcal{T}_C \Psi_\alpha(t) \Psi_\beta^\dagger(t') \rangle &= \text{Tr} \left[ \rho(t_0) \mathcal{T}_C \Psi_\alpha(t) \Psi_\beta^\dagger(t') \right] \\ &= \int \mathcal{D}\psi_0^+ \mathcal{D}\psi_0^- \left( \langle \psi_0^+ | \rho(t_0) | \psi_0^- \rangle \langle \psi_0^- | \mathcal{T}_C \Psi_\alpha(t) \Psi_\beta^\dagger(t') | \psi_0^+ \rangle \right). \end{aligned} \quad (2.17)$$



Between the density matrix and the time-ordered Heisenberg field operators, we also inserted an additional unity operator by taking advantage of the completeness of the eigenstates,  $\int \mathcal{D}\psi_0^- |\psi_0^- \rangle \langle \psi_0^-| = \mathbb{1}$ . The measure of the integral is  $\mathcal{D}\psi_0^{(\pm)} = \prod_\alpha d\psi_{0,\alpha}^\dagger d\psi_{0,\alpha}$ . The expectation value of the time-ordered Heisenberg field operators in the second line of Eq. (2.17) can be expressed as a path integral<sup>5</sup> [165], which is given in standard textbooks about quantum field theory [166, 167]. It reads

$$\langle \psi_0^- | \mathcal{T}_C \Psi_\alpha(t) \Psi_\beta^\dagger(t') | \psi_0^+ \rangle = \int_{\psi_0^+}^{\psi_0^-} \mathcal{D}'\psi \psi_\alpha(t) \psi_\beta^\dagger(t') \exp \left[ i \int_C dt \mathcal{L} \right], \quad (2.18)$$

where the integral measure of the path integral is defined on the time contour without the initial time  $\mathcal{D}'\psi = \prod_{\alpha, t \in C \setminus \{t_0\}} d\psi_\alpha^\dagger(t) d\psi_\alpha(t)$  and  $\mathcal{L}$  denotes the Lagrangian of the system. Accordingly, we can put this together and yield a path integral formulation for expectation values of time-ordered Heisenberg field operators,

$$\begin{aligned} \langle \mathcal{T}_C \Psi_\alpha(t) \Psi_\beta^\dagger(t') \rangle &= \int \mathcal{D}\psi_0^+ \mathcal{D}\psi_0^- \langle \psi_0^+ | \rho(t_0) | \psi_0^- \rangle \\ &\times \int_{\psi_0^+}^{\psi_0^-} \mathcal{D}'\psi \psi_\alpha(t) \psi_\beta^\dagger(t') \exp \left[ i S_C[\psi] \right], \end{aligned} \quad (2.19)$$

where the action is given by

$$S_C[\psi] = \int_C dt \mathcal{L}[\psi_\alpha, \psi_\alpha^\dagger]. \quad (2.20)$$

Since the expectation value of a fermionic field operator vanishes due to the Pauli principle, we introduce in the following, a method to calculate  $2n$ -point correlation functions by taking the  $n$ -th derivative of a generating functional. In addition to the action in the path integral, we also append an additional term that includes a non-local two-point source term,  $K_{\alpha\beta}(t, t')$ . The generating functional, also called partition functional, reads

$$\begin{aligned} Z[K; \rho(t_0)] &= \int \mathcal{D}\psi_0^+ \mathcal{D}\psi_0^- \langle \psi_0^+ | \rho(t_0) | \psi_0^- \rangle \\ &\times \int_{\psi_0^+}^{\psi_0^-} \mathcal{D}'\psi \exp \left[ i S_C[\psi] + i \int_C dt dt' \psi_\alpha^\dagger(t) K_{\alpha\beta}(t, t') \psi_\beta(t') \right]. \end{aligned} \quad (2.21)$$

This equation shows nicely the main components that make up non-equilibrium quantum field theory. The first line of the right-hand side embodies the initial conditions of the system, which describes the statistical fluctuations. The second line encloses information on the quantum fluctuations of the quantum dynamics via the action of the system,  $S_C$ . From the definition of the partition function in Eq. (2.21), it follows that

$$Z[K = 0, \rho(t_0)] = \text{Tr}[\rho(t_0)] = 1. \quad (2.22)$$

---

<sup>5</sup>In 1948, Richard Feynman introduced the path integral as a new formulation of quantum mechanics. It is nowadays a standard technique in quantum field theory.

The introduction of this non-local two-point source term is artificial and is made only for technical reasons, since it allows us to write higher-order correlation functions with the help of derivatives. After taking the derivative, we set the two-point source to zero. However, there are systems where such source terms have a physical meaning, such as an open system. In that case the source cannot be set to zero. The full  $2n$ -point correlation function is given by

$$\begin{aligned} & \langle \mathcal{T}_C \Psi_{\alpha_1}^\dagger(t_1) \Psi_{\beta_1}(t'_1) \cdots \Psi_{\alpha_n}^\dagger(t_n) \Psi_{\beta_n}(t'_n) \rangle \\ &= \frac{1}{Z} \frac{\delta^n Z[K; \rho(t_0)]}{i \delta K_{\alpha_1 \beta_1}(t_1, t'_1) \cdots i \delta K_{\alpha_n \beta_n}(t_n, t'_n)} \Bigg|_{K=0}. \end{aligned} \quad (2.23)$$

While the partition function provides the full correlation function, the Schwinger functional,  $W$ , which is defined by

$$W[K; \rho] = -i \ln Z[K; \rho], \quad (2.24)$$

gives only the connected part. This is due to the fact that the two-point correlation function or Green's function is connected in the case of fermions because there is no macroscopic fermionic field. Therefore, we get

$$\frac{\delta Z[K]}{\delta K_{\alpha\beta}(t, t')} = \frac{\delta W[K]}{\delta K_{\alpha\beta}(t, t')} = -G_{\beta\alpha}(t', t). \quad (2.25)$$

Higher derivatives of the generating functionals are different. It is obvious that higher derivatives of the Schwinger functional give more than one term because of the chain rule. The extra terms subtract the unconnected parts. In mathematical terms, the partition function generates moments and the Schwinger functional cumulants.

### Gaussian Initial States

In this section, so far, we have derived a path integral formulation for describing non-equilibrium dynamics for arbitrary initial conditions. In this subsection, we focus on the initial conditions, the first line in Eq. (2.21), to find an alternative formulation for the initial density matrix. It is sufficient to specify the first lowest correlation functions to describe experimental setups. For fermions, there are no expectation values of the fields, which means there is no macroscopic fermionic field and we have to set the initial conditions for the two-point correlation functions. We refer to this choice of initial conditions as Gaussian initial conditions. As a side effect of this choice of initial conditions, we can write the non-equilibrium partition function in a simpler or more compact way.

We write the initial density matrix in the most general form, which allows us to set arbitrary initial conditions and parametrise it as

$$\langle \psi_0^+ | \rho(t_0) | \psi_0^- \rangle = \mathcal{N} \exp [i f_C[\psi]], \quad (2.26)$$

where  $\mathcal{N}$  denotes a normalisation constant and  $f_{\mathcal{C}}$  is a functional of fields which can be expanded in powers of fields as

$$f_{\mathcal{C}}[\psi] = \alpha^{(0)} + \sum_{n=1}^{\infty} \frac{1}{n!} \int_{\mathcal{C}} \alpha_{\alpha_1 \dots \alpha_n}^{(n)}(t_1, \dots, t_n) \prod_{m=1}^n \psi_{\alpha_m}^{(\dagger)}(t_m). \quad (2.27)$$

The integral is along the Schwinger–Keldysh contour and it has to be evaluated on the forward branch,  $\mathcal{C}^+$ , and the backward branch,  $\mathcal{C}^-$ , of the closed time path with the boundary condition  $\psi^{(\dagger)}(t_0 \in \mathcal{C}^+) = \psi^{(\dagger)+}(t_0)$  and  $\psi^{(\dagger)}(t_0 \in \mathcal{C}^-) = \psi^{(\dagger)-}(t_0)$ . The Einstein notation for repeated indices is implied. The density matrix is only specified at the initial time, therefore the cumulants  $\alpha_{\alpha_1 \dots \alpha_n}^{(n)}(t_1, \dots, t_n)$  are only non-vanishing at the initial times on both branches of the Schwinger–Keldysh contour. The Hermiticity of the density matrix,  $\rho_0 = \rho_0^\dagger$ , imposes further conditions on the cumulants.

In the case of vanishing cumulants,  $\alpha_{\alpha_1 \dots \alpha_n}^{(n)}(t_1, \dots, t_n)$ , for all  $n > 2$  and at the initial times  $t_0$ , we obtain a Gaussian density matrix. As mentioned before, for fermions there are no field expectation values, thus the cumulant for  $n = 1$  can also be set to zero. For the Gaussian initial states, the non-equilibrium generating functional is given by

$$Z[K; \rho(t_0)] = \mathcal{N} \int \mathcal{D}\psi \exp \left[ i\alpha^{(0)} + \frac{i}{2} \int_{\mathcal{C}} dt dt' \alpha_{\alpha\beta}^{(2)}(t, t') \psi_{\alpha}^{\dagger}(t) \psi_{\beta}(t') \right. \\ \left. + iS_{\mathcal{C}}[\psi] + i \int_{\mathcal{C}} dt dt' \psi_{\alpha}^{\dagger}(t) K_{\alpha\beta}(t, t') \psi_{\beta}(t') \right]. \quad (2.28)$$

In contrast to Eq. (2.21), the integration measure  $\mathcal{D}\psi$  also includes the fields at the initial time,  $\psi_0^{(\pm)}$ , because they occur as the limits of the path integral and not as basis states of the matrix representation of the density matrix anymore. The zeroth cumulant  $\alpha^{(0)}$  can be shifted to the normalisation constant  $\mathcal{N}$ , which does not affect the non-equilibrium dynamics of a system. Therefore, we will drop it from now on. With a closer look at Eq. (2.28), we notice that the terms of the initial conditions for the two-point correlation function,  $\alpha_{\alpha\beta}^{(2)}$ , and the non-local two-point source,  $K_{\alpha\beta}$ , resemble each other. Therefore, we now define a new non-local two-point source,  $R_{\alpha\beta}$ , which combines both terms as

$$R_{\alpha\beta}(t, t') = K_{\alpha\beta}(t, t') + \frac{1}{2} \alpha_{\alpha\beta}^{(2)}(t, t'). \quad (2.29)$$

With this redefinition of the non-local two-point source,  $R$ , we can write the partition function in a compact form as

$$Z[R] = \int \mathcal{D}\psi \exp \left[ iS_{\mathcal{C}}[\psi] + i \int_{\mathcal{C}} dt dt' \psi_{\alpha}^{\dagger}(t) R_{\alpha\beta}(t, t') \psi_{\beta}(t') \right]. \quad (2.30)$$

In short, we are able to specify an arbitrary initial density matrix. In this thesis, we will stick with Gaussian initial conditions that allow us to write the non-equilibrium

generating functional in a compact way. We point out that, these initial conditions do not impose any restrictions on the non-equilibrium dynamics of the system. Higher correlation functions are not specified in the beginning but can build up during the non-equilibrium time evolution. In general, most physical setups are well approximated by Gaussian initial states, including experiments.

In the next section, we will introduce the 2PI effective action starting from the non-equilibrium generating functional in Eq. (2.30).

## 2.3 Non-Equilibrium Two-Particle Irreducible Effective Action

In the previous section in Eq. (2.36), we introduced the non-equilibrium generating functional which is a generalisation of the equilibrium partition function. We know in thermodynamics that the Legendre transform of the logarithm of the partition function also describes the same physics. In analogy to this, also in non-equilibrium quantum field theory, the Legendre transform of the Schwinger functional in Eq. (2.24) gives another equivalent representation. The Legendre transform with respect to the one-point source term leads to the one-particle irreducible (1PI) effective action, and the Legendre transform up to the two-point source term gives the two-particle irreducible effective action (2PI). This procedure can be generalised to an arbitrary order of source terms to get an  $n$ PI effective action [168].

All the generating functionals describe the physics equivalently. The main advantage of effective actions is that they are expressed in terms of correlation functions. The initial values of correlation functions are easier to access than those of source terms. In addition to this, the effective action obeys the variational principle, which makes it easier to derive dynamic equations for the correlation functions. We look for an effective action that fulfils

$$\frac{\delta\Gamma[D]}{\delta D} = 0. \quad (2.31)$$

We introduce the (2PI) effective action [103–105] via a Legendre transform of the Schwinger functional given in Eq. (2.24) with respect to the two-point source term,  $R$ . We get

$$\Gamma[D] = W[R] - \int_{\mathcal{C}} dt dt' \frac{\delta W[R]}{\delta R_{\alpha\beta}(t, t')} R_{\alpha\beta}(t, t') = W[R] + \text{Tr}[DR], \quad (2.32)$$

where we took advantage of

$$-D_{\beta\alpha}(t', t; R) = \frac{\delta W[R]}{\delta R_{\alpha\beta}(t, t')}. \quad (2.33)$$

Eq. (2.32) uses a trace which implies a sum over all field indices and an integration along the Schwinger–Keldysh closed time path. By taking the functional derivative

with respect to this 2PI effective action we get

$$\frac{\delta\Gamma[D]}{\delta D_{\beta\alpha}(t', t; R)} = R_{\alpha\beta}(t, t'), \quad (2.34)$$

which is the stationary condition in Eq. (2.31), in the case of a vanishing non-local source,  $R$ .

In the following, we want to calculate the 2PI effective action, which means we first need an expression for the generating functional of the  $2n$ -point correlation function given in Eq. (2.30). In general, the action contains a free and an interaction part

$$S_{\mathcal{C}}[\psi] = \int_{\mathcal{C}} dt dt' \psi_{\alpha}^{\dagger}(t) iD_{0,\alpha\beta}^{-1}(t, t') \psi_{\beta}(t') + S_{\mathcal{C},\text{int}}[\psi], \quad (2.35)$$

where the free inverse propagator<sup>6</sup>  $D_{0,\alpha\beta}^{-1}$  appears in the free part of the action. We Taylor expand the exponential containing the interaction action term. Then, the partition function reads

$$\begin{aligned} Z[R] &= \int \mathcal{D}\psi \exp\left(-\int_{\mathcal{C}} dt dt' \psi_{\alpha}^{\dagger}(t) (D_{0,\alpha\beta}^{-1}(t, t') - iR_{\alpha\beta}(t, t')) \psi_{\beta}(t')\right) \\ &+ \int \mathcal{D}\psi \exp\left(-\int_{\mathcal{C}} dt dt' \psi_{\alpha}^{\dagger}(t) (D_{0,\alpha\beta}^{-1}(t, t') - iR_{\alpha\beta}(t, t')) \psi_{\beta}(t')\right) \\ &\times \sum_{n=1}^{\infty} \frac{(iS_{\mathcal{C},\text{int}})^n}{n!}. \end{aligned} \quad (2.36)$$

In the first line, we pulled out the term corresponding to  $n = 0$  because it is a Gaussian path integral which is exactly solvable and gives a functional determinant expression. This term is referred to as the one-loop order. The second summand includes the interaction of the underlying model and is at least of the order of two loops. In the following steps, we focus on the one-loop part and derive the 2PI effective action at one-loop order. Performing the Gaussian path integral, we obtain for the partition functional at one-loop order,

$$\begin{aligned} Z^{(1 \text{ loop})}[R] &= \det\left(D_{0,\alpha\beta}^{-1}(t, t') - iR_{\alpha\beta}(t, t')\right) \\ &= \exp\left(\text{Tr} \ln\left(D_{0,\alpha\beta}^{-1}(t, t') - iR_{\alpha\beta}(t, t')\right)\right). \end{aligned} \quad (2.37)$$

From this follows the Schwinger generating functional for connected correlation functions at one-loop order,

$$W^{(1 \text{ loop})}[R] = -i \ln Z^{(1 \text{ loop})} = -i \text{Tr} \ln\left(D_{0,\alpha\beta}^{-1}(t, t') - iR_{\alpha\beta}(t, t')\right). \quad (2.38)$$

---

<sup>6</sup>The free inverse propagator is the inverse propagator of the free, non-interacting theory. For a non-relativistic system, it can usually be written as  $iD_{0,\alpha\beta}^{-1}(t, t') = \delta(t - t') (i\partial_t - H_{\alpha}^{1\text{B}}(t)) \delta_{\alpha\beta}$ , where  $H^{1\text{B}}$  denotes the one-body Hamiltonian. We also used  $\hbar = 1$  and we will use this throughout the thesis.

Finally, we arrive at the 2PI effective action at one-loop order,

$$\begin{aligned}\Gamma^{(1\text{ loop})}[D] &= W^{(1\text{ loop})}[R] + \text{Tr}(DR) \\ &= -i \text{Tr} \left( \ln D^{-1} + D(D_0^{-1} - D^{-1}) \right).\end{aligned}\quad (2.39)$$

In the last step, we set  $D^{-1} = D_0^{-1} - iR$  because the effective action, also at one-loop order, has to fulfil the stationary condition in Eq. (2.34):

$$i \left( D_{\alpha\beta}^{-1}(t, t') - D_{0,\alpha\beta}^{-1}(t, t') \right) = R_{\alpha\beta}(t, t') \quad \Rightarrow \quad D^{-1} = D_0^{-1} - iR. \quad (2.40)$$

At one-loop order, the full propagator is the same as the free propagator as long as no external sources are present.

Since we have now fully discussed the one-loop term, we draw the reader's attention to the second term in Eq. (2.36). We can write this contribution, which is at least of two-loop order, as an additional term to the one-loop 2PI effective action

$$\Gamma[D] = -i \text{Tr} \left( \ln D^{-1} + DD_0^{-1} \right) + \Gamma_2[D]. \quad (2.41)$$

In this expression, we dropped the constant term  $\text{Tr}(DD^{-1})$  because it is irrelevant for the dynamics of the system. All scattering effects are absorbed in the  $\Gamma_2[D]$  term.

We can depict the  $\Gamma_2[D]$  term with the help of Feynman diagrams<sup>7</sup> [169]. However first, in the following, we have to specify which conditions  $\Gamma_2[D]$  must satisfy. The effective action is a functional of the full propagator,  $D$ , which means that mathematically the effective action maps the full propagator to a scalar because it has no indices or time arguments. If we transfer this finding to the Feynman diagrams, the effective action contains only closed diagrams. It can be shown that the  $\Gamma_2[D]$  term is the sum of all possible 2PI Feynman diagrams assembled from bare vertices and full propagators,  $D$ . The 2PI term for Feynman diagrams means that we can cut two lines and the Feynman diagram is still connected. We also call this term the 2PI part of the effective action. The definition is

$$\Gamma_2[D] = -i \left\langle \sum_{n=1}^{\infty} \frac{(iS_{\text{int}})^n}{n!} \right\rangle_{2\text{PI} \& D}, \quad (2.42)$$

where  $\langle \cdot \rangle_{2\text{PI} \& D}$  denotes the expectation value of  $n$  interaction terms  $S_{\text{int}}$  with the condition that the corresponding Feynman diagrams have to be 2PI and the lines are the full propagators,  $D$ . The exact appearance of the 2PI Feynman diagrams is determined by the interaction term of the action. Thus, it is determined by the underlying model that is taken into consideration. In this thesis, we want to investigate a fermionic system at low temperatures and energies, therefore no relativistic effects

---

<sup>7</sup>Richard Feynman invented the pictorial representation of complicated mathematical expressions for subatomic scattering processes.

such as the annihilation and creation of particles will occur and we do not expect bound states. For this reason, we assume a two-to-two body scattering which means that at each interaction vertex four full propagator lines meet. For this interaction term, we show the Feynman diagram representation of the 2PI part of the effective action up to fourth order explicitly as

$$\begin{aligned}
 \Gamma_2[D] = & \text{Diagram 1} + \text{Diagram 2} + \text{Diagram 3} \\
 & + \text{Diagram 4} + \text{Diagram 5} + \dots,
 \end{aligned} \tag{2.43}$$

where the solid blue lines represent the full propagator,  $D$ , and the black dots are the bare vertices. In these Feynman diagrams, we do not distinguish between spin up and down because here we are focusing solely on the general structure of the diagrams. In Ch. 3, we introduce the specific model for this thesis and when we apply the 2PI effective action techniques to this model, in Ch. 4, we will show the Feynman diagrams in full detail.

So far, we have not given a reason why the Feynman diagrams that make up the 2PI part of the effective action,  $\Gamma_2$ , have to be 2PI. However, we have explained why they have to be closed. In the next section, where we derive an exact dynamic equation for the full propagator or two-point Green's function, the 2PI condition imposed on the Feynman diagrams will become clear.

## 2.4 Exact Non-Equilibrium Dynamic Equation

In the previous section, we introduced the 2PI effective action which incorporates statistical as well as quantum fluctuations. From this effective action, we want to derive a dynamic equation for the two-point Green's function in this section. Up to this point, we have not made any approximations in the derivation of the 2PI effective action and therefore, the derived dynamic equation, via the stationary condition, will be exact. Also, the Gaussian initial conditions we introduced in Subsec. 2.2 are not an approximation to the quantum dynamics of the system. Only the higher correlations are set to zero at the beginning. However, during the time evolution these higher correlations can build up. The higher correlation functions are very important for equilibration processes.

### 2.4.1 Exact Dynamic Equation for the Two-Point Green's Function

We put the full 2PI effective action given in Eq. (2.42) into the stationary condition in Eq. (2.34) and yield the well-known real time Schwinger–Dyson equation [170, 171]

$$D_{\alpha\beta}^{-1}(t, t'; R) = D_{0,\alpha\beta}^{-1}(t, t') - iR_{\alpha\beta}(t, t') - \Sigma_{\alpha\beta}(t, t'; D), \quad (2.44)$$

where we used

$$\Sigma_{\alpha\beta}(t, t'; D) = -i \frac{\delta\Gamma_2[D]}{\delta D_{\beta\alpha}(t', t; R)}, \quad (2.45)$$

which is the one-particle irreducible (1PI) self-energy. Here, it becomes clear why the  $\Gamma_2$  term has to be 2PI. Since by taking the derivative we, graphically speaking, cut one full propagator line,  $D$ , in the corresponding Feynman diagram and therefore reduce the order of the particle irreducibility by one. Thus, the self-energy imposes the 2PI condition on  $\Gamma_2$ .

The Schwinger–Dyson equation, Eq. (2.44), which we recover from the stationary condition of the 2PI effective action, is not easily numerically solvable for given initial conditions. Therefore, we convolve this equation with the full propagator,  $D$ , and obtain the equivalent Kadanoff–Baym equation of motion [104, 155],

$$\begin{aligned} \int_{\mathcal{C}} dz iD_{0,\alpha\gamma}^{-1}(t, z)D_{\gamma\beta}(z, t'; R) &= i\delta_{\mathcal{C}}(t - t')\delta_{\alpha\beta} \\ &+ i \int_{\mathcal{C}} dz \left( \Sigma_{\alpha\gamma}(t, z; D) + iR_{\alpha\gamma}(t, z) \right) D_{\gamma\beta}(z, t'; R). \end{aligned} \quad (2.46)$$

The two-point source,  $R$ , brings for the initial time,  $t_0$ , the information about the density matrix into the equation. In a closed system,  $R$  is only non-vanishing at the initial time,  $t_0$ , at both branches on the Schwinger–Keldysh contour. In this case, the term does not influence the dynamics of the system. This changes when a system is open and can interact with its environment. In general, the non-local two-point source term can be non-vanishing at all times and also has a deep impact on the dynamics.

Since we are considering a non-relativistic system, the free inverse propagator  $D_0^{-1}$  includes a first order time derivative and it is also diagonal in the time space. Thus, we can perform the integral and write the Kadanoff–Baym equations of motion as an integro-differential equation. In addition to this, we also pull out the local contribution of the self-energy

$$\Sigma_{\alpha\beta}(t, t'; D) \rightarrow -i\Sigma_{\alpha\beta}^{(0)}(t; D)\delta_{\mathcal{C}}(t - t') + \Sigma_{\alpha\beta}(t, t'; D) \quad (2.47)$$

and from now on  $\Sigma$  denotes only the non-local proper self-energy. The local contribution to the self-energy can be combined with the one-body Hamiltonian appearing in the free inverse propagator,  $D_0^{-1}$ , which yields

$$M_{\alpha\beta}(t, t'; D) = \delta_{\mathcal{C}}(t - t') \left( \delta_{\alpha\beta} H_{\alpha}^{1B}(t) + \Sigma_{\alpha\beta}^{(0)}(t; D) \right). \quad (2.48)$$



In the next step, we insert all of this into Eq. (2.46) and can perform the integration over the free inverse propagator and the local contribution of the self-energy because of the delta function. Now, the Kadanoff–Baym equation of motion reads

$$\left(i\partial_t - M_{\alpha\gamma}(t, t; D)\right)D_{\alpha\beta}(t, t') - i\delta_{\alpha\beta}\delta_{\mathcal{C}}(t - t') = \int_{\mathcal{C}} dz i\Sigma_{\alpha\gamma}(t, z; D)D_{\gamma\beta}(z, t'). \quad (2.49)$$

We dropped the term  $\int RD$  because  $R$  enters the dynamic equation in the same way as the self-energy and therefore the non-local source term,  $K$ , can also be shifted into the self-energy. The cumulant that specifies the initial condition of the two-point correlation function enters via the initial condition of the integro-differential equation. In the next subsection we will decompose the Kadanoff–Baym equation of motion into its statistical and spectral components.

### 2.4.2 Exact Dynamic Equations for the Statistical Propagator and the Spectral Function

In the previous section, we derived an integro-differential equation, the so-called Kadanoff–Baym equation of motion, for the two-point Green’s function. In this section, we split this equation into its statistical and spectral components. As in Eq. (2.6), we do the same decomposition for the non-local self-energy,

$$\Sigma_{\alpha\beta}(t, t') = \Sigma_{\alpha\beta}^{\text{F}}(t, t') - \frac{i}{2}\Sigma_{\alpha\beta}^{\rho}(t, t') \text{sgn}_{\mathcal{C}}(t - t'). \quad (2.50)$$

We insert both decompositions in Eq. (2.49) and use the identities for sign functions on the Schwinger–Keldysh contour:

$$\int_{\mathcal{C}} dt \text{sgn}_{\mathcal{C}}(t' - t) = 2 \int_{t_0}^{t'} dt \quad (2.51)$$

and

$$\int_{\mathcal{C}} dz \text{sgn}_{\mathcal{C}}(t - z) \text{sgn}_{\mathcal{C}}(z - t') = 2 \text{sgn}_{\mathcal{C}}(t - t') \int_{t'}^t dz. \quad (2.52)$$

We end up with the Kadanoff–Baym equations of motion for the statistical propagator,  $F$ , and spectral function,  $\rho$ ,

$$\begin{aligned} \left(i\delta_{\alpha\gamma}\partial_t - M_{\alpha\gamma}(t; D)\right)F_{\gamma\beta}(t, t') &= \int_{t_0}^t dz \Sigma_{\alpha\gamma}^{\rho}(t, z; D)F_{\gamma\beta}(z, t') \\ &\quad - \int_{t_0}^{t'} dz \Sigma_{\alpha\gamma}^{\text{F}}(t, z; D)\rho_{\gamma\beta}(z, t') \\ \left(i\delta_{\alpha\gamma}\partial_t - M_{\alpha\gamma}(t; D)\right)\rho_{\gamma\beta}(t, t') &= \int_{t'}^t dz \Sigma_{\alpha\gamma}^{\rho}(t, z; D)\rho_{\gamma\beta}(z, t'). \end{aligned} \quad (2.53)$$

The time derivative acting on the two-point Green’s function also acts on the sign function in front of the spectral function when we use the decomposition in Eq. (2.6).

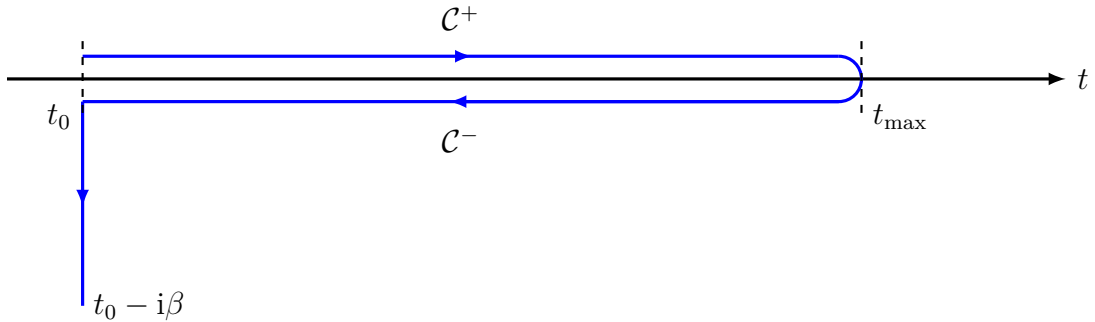


**Figure 2.2:** In thermal equilibrium, the Schwinger–Keldysh closed time path is extended by a strip along the imaginary time axis from the time  $t_0$  to  $t_0 - i\beta$  to the so-called Konstantinov–Perel’ contour. The entire path is denoted by  $\mathcal{C}_\beta$ . Times in the imaginary part of the time contour,  $\mathcal{C}_\beta$ , are considered to be later than any time on the Schwinger–Keldysh contour,  $\mathcal{C}$ . The extended time path,  $\mathcal{C}_\beta$ , is supposed to be closed such that it addresses boundary conditions to the operators at the initial times  $t_0$  and  $t_0 - i\beta$ .

Since  $\text{sgn}_{\mathcal{C}}(t - t') = 2\theta(t - t') - 1$  it follows that  $\partial_t \text{sgn}_{\mathcal{C}}(t - t') = 2\delta_{\mathcal{C}}(t - t')$ . This exactly cancels the delta term in Eq. (2.49) because  $\rho(t, t) = i$ .

The product of the self-energy and the two-point Green’s functions gives four terms but only three of them survive because ordinary functions integrated on a closed time path vanish. Two terms include one sign function which vanishes due to the identity in Eq. (2.51) and therefore contribute to the dynamic equation of the statistical component. The last term including two sign functions contribute to the spectral component because of Eq. (2.52). The memory integrals on the right hand side are normal time integrals which are no longer on a closed time path.

We now have a set of coupled integro-differential equations. The initial condition of the full propagator enters the Kadanoff–Baym equations of motions via the initial value of the statistical propagator,  $F$ , and spectral function,  $\rho$ , at initial time  $t_0$ . The scattering processes that were once in the 2PI part of the effective action are encoded into non-Markovian memory integrals on the right-hand side. They are called memory integrals because the dynamics of the present and the future is influenced by the entire past of the system. The form of the equations do not change with the approximation we have made in order to numerically calculate solutions to these equations. We discuss the commonly used approximations in Ch. 4 after we specify the Hamiltonian of the system in Ch. 3.

## 2.5 Thermal Equilibrium

So far, we have discussed a general theory describing non-equilibrium physics. In this section, we want to focus on a system in equilibrium at finite temperature. The thermal equilibrium can be regarded as a special case of non-equilibrium. The system

can initially be described by a (grand) canonical ensemble with the density matrix

$$\rho_\beta = \frac{1}{Z_\beta} e^{-\beta H}, \quad (2.54)$$

and the partition function  $Z_\beta = \text{Tr} \exp(-\beta H)$ , where  $\beta$  is the inverse temperature<sup>8</sup>,  $\beta = T^{-1}$ . For the path integral formulation, we follow exactly the same steps as in Sec. 2.2. Thus, we have to replace the general density matrix in the non-equilibrium case with the density matrix given in Eq. (2.54) and use the eigenstates of the Heisenberg field operators at the initial time,  $t_0$ , for the calculation of the trace. We get

$$Z_\beta = \int \mathcal{D}\psi_0 \langle \psi_0 | \rho_\beta | \psi_0 \rangle. \quad (2.55)$$

With a closer look at the numerator of Eq. (2.54), it becomes clear that  $e^{-\beta H}$  resembles a time evolution operator if we write  $e^{-\beta H} = e^{-i(-i\beta)H} = \mathcal{U}(t_0, t_0 - i\beta)$ , with the unusual property that this time evolution operator evolves the system to imaginary times which depend on the temperature. Thus, we get

$$\langle \psi_0 | \rho_\beta | \psi_0 \rangle = \langle \psi_{0-i\beta} | \psi_0 \rangle. \quad (2.56)$$

This consideration alone suggests that we extend the Schwinger–Keldysh contour discussed in Subsec. 2.1.2 by an imaginary strip along the imaginary time axis. We depict this new complex time path, also called the Konstantinov–Perel’ contour [172]  $\mathcal{C}_\beta$ , in Fig. 2.2. All times in the imaginary part are considered to be later than all times on the Schwinger–Keldysh closed time path. From the cyclic property of the trace, it follows that we have to identify the initial time,  $t_0$ , with the final time,  $t_0 - i\beta$ , which means this time path is also supposed to be closed. Therefore, we get certain periodicity conditions, also called Kubo–Martin–Schwinger (KMS) conditions [161, 162]. For a two-point Green’s function, it follows at the initial time,  $t_0$ , and final time,  $t_0 - i\beta$ , that

$$\begin{aligned} \langle \mathcal{T}_{\mathcal{C}_\beta} \psi(t) \psi^\dagger(t') \rangle \Big|_{t=t_0} &= - \langle \psi^\dagger(t') \psi(t) \rangle \Big|_{t=t_0}, \\ \langle \mathcal{T}_{\mathcal{C}_\beta} \psi(t) \psi^\dagger(t') \rangle \Big|_{t=t_0-i\beta} &= \langle \psi(t) \psi^\dagger(t') \rangle \Big|_{t=t_0-i\beta}, \end{aligned} \quad (2.57)$$

and with that

$$- \langle \psi^\dagger(t') \psi(t) \rangle \Big|_{t=t_0} = \langle \psi(t) \psi^\dagger(t') \rangle \Big|_{t=t_0-i\beta}. \quad (2.58)$$

The generating functional for the complex time contour ordered,  $2n$ -point correlation functions with Gaussian initial states is

$$Z_\beta[R] = \int \mathcal{D}\psi \exp \left[ iS_{\mathcal{C}_\beta} + i \int_{\mathcal{C}_\beta} dt dt' \psi_\alpha^\dagger(t) R_{\alpha\beta}(t, t') \psi_\beta(t') \right], \quad (2.59)$$

---

<sup>8</sup>The inverse temperature is  $\beta = (k_B T)^{-1}$  with the Boltzmann constant  $k_B$ . However, we set  $k_B = 1$ .

with the action on this time contour given by

$$S_{\mathcal{C}_\beta}[\psi] = \int_{\mathcal{C}_\beta} dt \mathcal{L}[\psi_\alpha, \psi_\alpha^\dagger]. \quad (2.60)$$

The two-point Green's function decomposed into the statistical propagator,  $F$ , and spectral function,  $\rho$ , reads

$$D_{\alpha\beta}(t-t') = F_{\alpha\beta}(t-t') - \frac{i}{2}\rho_{\alpha\beta}(t-t') \operatorname{sgn}_{\mathcal{C}_\beta}(t-t'), \quad (2.61)$$

where we used that in thermal equilibrium the system has time-translational invariance, which means that all functions depend only on the difference of the times.

### 2.5.1 Fluctuation-Dissipation Relation

A quantum system that is initially set far-from-equilibrium will evolve towards equilibrium, which means that the system is time- and space-translation invariant. However, this does not mean that the system is also thermalised in the sense that it is possible to describe the system with a (grand) canonical density matrix. It was shown for a one dimensional non-relativistic interacting Fermi gas in Ref. [126] that it can equilibrate without being thermalised. The fluctuation-dissipation relation provides the possibility to check whether the equilibrated state is also thermalised.

In the following we derive the fluctuation-dissipation relation by taking advantage of the KMS boundary conditions in Eqs. (2.57) and (2.58) and using the decomposition of the two-point Green's function in the statistical propagator,  $F$ , and the spectral function,  $\rho$ . We obtain

$$-\left(F(t, t') + \frac{i}{2}\rho(t, t')\right)\Big|_{t=t_0} = \left(F(t, t') - \frac{i}{2}\rho(t, t')\right)\Big|_{t=t_0-i\beta}. \quad (2.62)$$

We use the inverse Fourier transform for the statistical propagator,  $F$ , and also for the spectral function,  $\rho(t, t') = \int_{-\infty}^{\infty} \frac{d\omega}{2\pi} e^{-i\omega(t-t')} \rho(\omega)$ . Then, Eq. (2.62) reads

$$F(\omega) + \frac{i}{2}\rho(\omega) = e^{-\beta\omega} \left(-F(\omega) + \frac{i}{2}\rho(\omega)\right). \quad (2.63)$$

Due to the imaginary part on the final point of the time contour, we get the additional factor,  $\exp(-\beta\omega)$ . In the next step, we rearrange this equation such that the statistical propagator is isolated on the left hand side. We get the well-known Callen–Welton dissipation-fluctuation relation [173] which reads

$$F(\omega) = -i\left(\frac{1}{2} - n(\omega)\right)\rho(\omega), \quad (2.64)$$

where  $n(\omega) = (\exp(\beta\omega) + 1)^{-1}$  denotes the Fermi–Dirac distribution function. In thermal equilibrium, the statistical propagator,  $F$ , is connected with the spectral function,  $\rho$ , via a Fermi–Dirac distribution function. This is a result of the special

choice of density matrix. In non-equilibrium, where we have an arbitrary density matrix, it is also always possible to take the fraction of the two functions that make up the two-point Green's function. However, *a priori* it is not clear how this function looks. This is different to the special case of thermal equilibrium. Since in thermal equilibrium, the degrees of freedom for the Green's function are reduced because we only have to know one of the two functions.

## 2.6 Summary

In this section, the main goal was to derive exact dynamic equations for the two-point Green's function, the so-called Kadanoff–Baym equations of motion, in a general formulation for non-relativistic fermionic systems without any further specification of the model. With this tool, we are able to tackle non-equilibrium physical situations and can describe their quantum dynamics.

In the beginning, we introduced the two-point Green's function and found a decomposition in the statistical propagator,  $F$ , which describes the occupation of the available states in the system and the spectral function,  $\rho$ , which gives information about the spectrum of the system. In the next step, we introduced a path integral formulation of the non-equilibrium generating functional for  $2n$ -point correlation functions. This partition function contains the statistical fluctuations given by a general density matrix and the quantum fluctuations arising from a specific action. We use the convenient Schwinger–Keldysh closed time path formalism to access the full non-equilibrium information of the system encoded in the correlation functions. The initial density matrix sets the initial values of the correlation functions. It is sufficient for almost all purposes to use the correlation functions up to the second order. With these so-called Gaussian initial states, we introduced the two-particle irreducible effective action via a Legendre transform of the Schwinger functional. From this effective action, we could derive the exact dynamic equation for the two-point Green's function through the variational principle. We could then write this equation as a set of coupled integro-differential equations for the statistical propagator and the spectral function. In this formulation, only standard time integrals are present in the memory integrals.

At the end, we also discussed the special case of thermal equilibrium where the initial density matrix is given by a (grand) canonical ensemble. In thermal equilibrium the degrees of freedom are reduced because the statistical propagator and the spectral function are connected to each other via a Fermi–Dirac distribution function which is referred to as the fluctuation-dissipation relation.



# Chapter 3

## Physical Background of Quantum Dots

In the previous chapter, we used a path integral approach to introduce the two-particle (2PI) irreducible effective action. This effective action is a functional of the full propagator and incorporates the full quantum dynamics arising from the underlying Hamiltonian and statistical fluctuations encoded in the general density matrix. From the 2PI effective action, we derived an exact dynamic equation for the two-point Green's function, also known as the Kadanoff–Baym equation of motion, for a spatially zero-dimensional non-relativistic system without any further specification of the interaction. In order to solve this dynamic equation numerically, we have to make approximations to the self-energy of the full propagator due to the complexity of the mathematical structure of the equation. However, this demands the precise knowledge of an interaction term, which is why we need to specify the underlying Hamiltonian of our investigation.

In this chapter, we focus on the physical fundamentals of quantum dots. First, we introduce a quantum dot, which is an elementary component of electronic nanotechnology and has attracted a lot of attention over the past twenty years. In addition to this, we explain the main components of such nanodevices and the tunability of the most important parameters that have a strong influence on the physics. Second, we introduce the Kondo effect in a quantum dot. This effect has a tremendous non-trivial impact on the transport properties of quantum dots. Although it was first experimentally observed in the 1990s, the Kondo effect is still under investigation; especially the time-evolution in and out of equilibrium. Third, we introduce the single impurity Anderson model (SIAM), which is the role model to describe the forming of magnetic moments in metals and it also reflects the physics of quantum dots. At the end, we discuss the phase diagram of the SIAM to see where the Kondo regime is located in the parameter space.

### 3.1 Quantum Dot

In the last two decades, the rapid development of nanoelectronics, especially quantum dots, has led to various different fabrications such as two-dimensional electron gases, carbon nanotubes [174], metallic nanoparticles and also in recent years, the pop-

ularisation of indium arsenid nanowire quantum dots [175]. The general structure of quantum dots is independent of the special fabrication. Quantum dots are mesoscopic nanoelectronic devices with electronic properties between bulk materials and atoms. A certain number of electrons are confined in a small three-dimensional region with discrete energy levels, where the exact available energies strongly depend on the confining potential. Due to the smallness of such devices (of the order of 100 nm) and consequently the discreteness of the quantum dot's spectrum, it can be well-described as spatially zero-dimensional object. This electronic island is, in general, contacted capacitively with two leads forming a tunnelling barrier, which determines the probability of exchanging electrons. In experiments, this barrier can be controlled by voltages. In addition to this, a gate voltage is also capacitively coupled to the quantum dot for tuning the available energy levels. This can be seen in the equivalent electronic circuit of the quantum dot, depicted on the left-hand side of Fig. 3.1.

A frequently used model to describe the energy levels of a quantum dot is the constant interaction model (CIM) [176]. In this simplifying model, it is assumed that first, the single-electron energy levels of the quantum dot are not perturbed by the interaction and second, the interaction of the electrons on the quantum dot is determined by a constant capacitance,  $C = C_L + C_R + C_G$ , where  $C_L$ ,  $C_R$ , and  $C_G$  denote the capacitance of the contact of the leads and gate to the quantum dot. Without loss of generality, we assume the right lead to be grounded. Then according to the CIM, the total energy,  $E_{\text{tot}}$ , of a quantum dot with  $N$  electrons is given by

$$E_{\text{tot}}(N) = \frac{(q(N - N_0) + C_L V_B + C_G V_G)^2}{2C} + \sum_{i=1}^N E_i, \quad (3.1)$$

where  $N_0$  denotes the number of electrons at zero gate voltage,  $q$  the electron charge,  $V_B$  the bias voltage, and  $V_G$  the gate voltage. The last term describes the energy eigenvalues of the single-particle Schrödinger equation with a certain confining potential<sup>1</sup> of the quantum dot. The chemical potential of the quantum dot,  $\mu_{\text{dot}}$ , is defined by

$$\mu_{\text{dot}}(N) = E_{\text{tot}}(N) - E_{\text{tot}}(N - 1). \quad (3.2)$$

An electrical current through the quantum dot can flow if the quantum dot's chemical potential lies between the Fermi edges of the leads. The addition energy,  $E_{\text{add}}$ , to add one more electron to the quantum dot is then given by

$$\begin{aligned} E_{\text{add}} &= \mu_{\text{dot}}(N + 1) - \mu_{\text{dot}}(N) \\ &= \frac{q^2}{C} + E_{N+1} - E_N, \end{aligned} \quad (3.3)$$

with the charging energy,  $U$ , and orbital level spacing,  $\delta E$ , given by

---

<sup>1</sup>This depends strongly on the geometry of the quantum dot. In most cases, a box or harmonic potential is assumed. For a three-dimensional isotropic harmonic potential, the energy eigenvalues read  $E_{n,l} = (2n + l + 3/2)\hbar\omega$ .



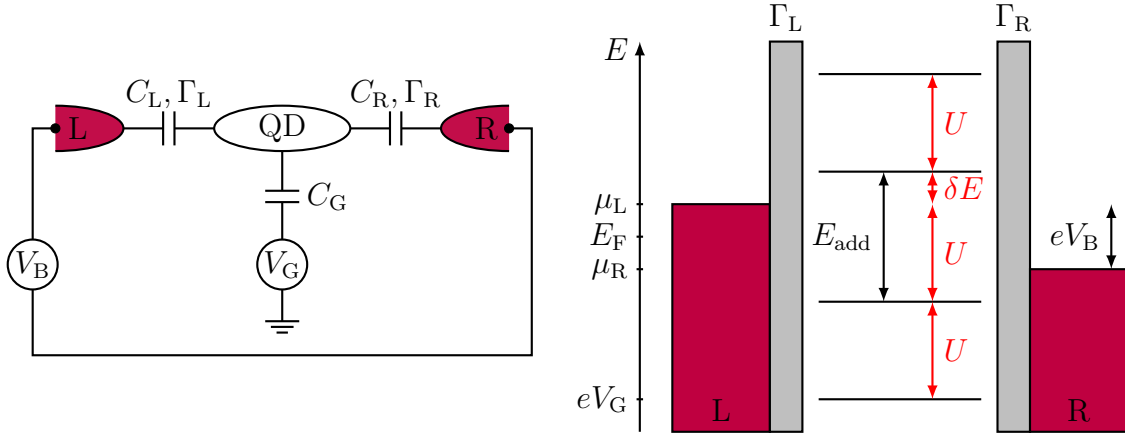


**Figure 3.1:** Left: The equivalent electronic circuit of a quantum dot coupled capacitively to three contacts: the left lead, right lead and gate contact. The energy levels on the dot can be adjusted by the gate voltage,  $V_G$ , and the bias voltage,  $V_B$ , controls the chemical potential of the leads. Right: Schematic energy diagram of a quantum dot coupled to two leads with chemical potential,  $\mu_{L,R}$ . The discrete energy levels belonging to the same orbital are separated by the charging energy,  $U$ , and to different orbitals by an extra amount for the orbital spacing,  $\delta E$ .

$$U = \frac{q^2}{C}, \quad \delta E = E_{N+1} - E_N. \quad (3.4)$$

Consequently, the on-site Coulomb repulsion can be controlled by the total capacitance,  $C$ . On the right-hand side of Fig. 3.1, a schematic energy diagram of a quantum dot coupled to two leads is shown. The leads are indicated by the red rectangles and the energy levels below the Fermi edges of the leads are occupied. Energy levels belonging to the same orbital are separated by the charging energy,  $U$ , and otherwise the additional orbital level spacing,  $\delta E$ , comes on top of it. The grey shaded areas represent the tunnel barriers which determine the tunnelling probability and can be adjusted by the left lead, right lead and quantum dot capacitance,  $C_{L,R}$ . Furthermore, the energy levels are adjusted by the applied gate voltage,  $V_G$ . All relevant parameters determining the physics of the quantum dot are tunable via the gate and bias voltage, which is a tremendous advantage of such systems.

## 3.2 Kondo Effect

Since the Kondo effect is the central topic of this thesis, we explain the Kondo effect in a quantum dot in full detail in this section. We assume that the quantum dot is coupled to two leads with the same chemical potentials,  $\mu_L = \mu_R$ . For the Kondo effect, the gate voltage of the quantum dot is tuned such that it is occupied by one electron which can be spin-up or spin-down with equal probability. This is achieved when first, the single electron energy,  $E_0$ , is smaller than the Fermi energy of the

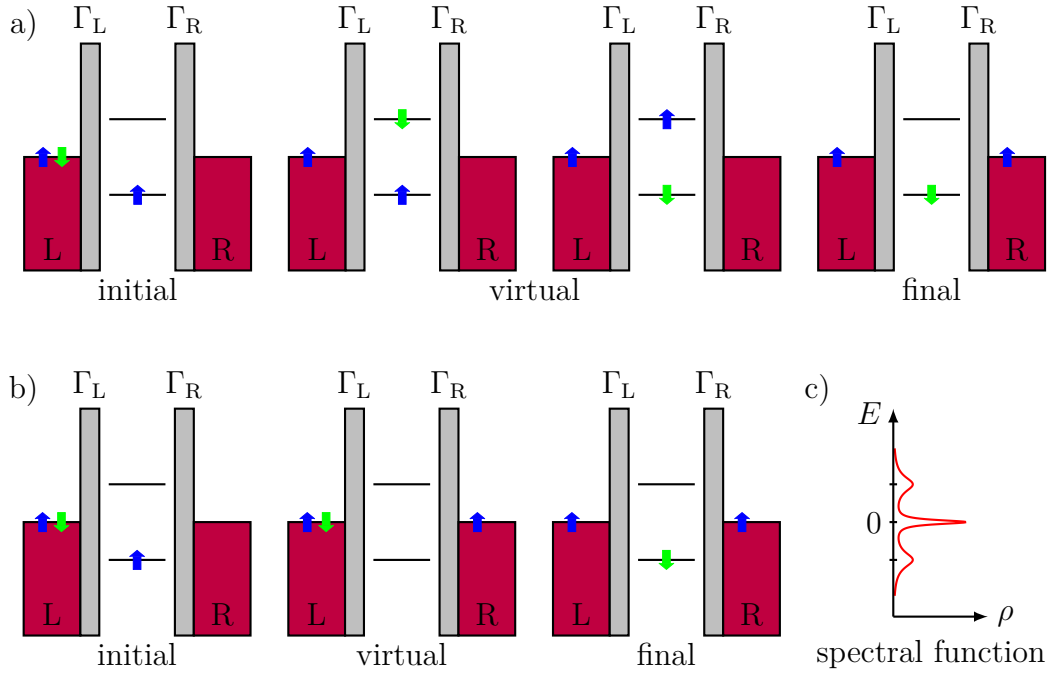


**Figure 3.2:** Illustration of two possible cotunnelling processes on a quantum dot in the particle-hole symmetric case with a double occupied (a) and an unoccupied virtual state (b) that give rise to the Kondo effect. Initially, the quantum dot is occupied by one electron mimicking the magnetic impurity. The virtual state is energetically forbidden (Coulomb blockade) because the Fermi energy lies between the two possible energy levels on the quantum dot and therefore both virtual states cost energy,  $E = U/2$ . Due to Heisenberg's uncertainty principle, it can occur in an intermediate state in a time scale of  $t \sim E^{-1}$ . In the final state, the spin is flipped on the quantum dot. c) The expected spectral function consists of two Hubbard side peaks located at  $E = \pm U/2$  and the sharp Kondo peak at the Fermi energy.

leads,  $E_0 < E_F$ , and second, due to the Coulomb repulsion when the double-occupied energy level lies above the single electron energy by the charging energy,  $U$ , and must be larger than the Fermi energy,  $E_0 + U > E_F$ . In the particle-hole symmetric case, both energy levels on the quantum dot are aligned symmetrically around the Fermi energy,  $E_0 = -U/2$ . In principle, in this situation, an additional electron cannot tunnel into the quantum dot, nor can the first electron tunnel out of the quantum dot, because both events cost energy. This situation is called a Coulomb blockade and is shown in Fig. 3.2 as the initial state.

However, this is only true for first-order tunnelling processes and changes if higher-order cotunnelling processes are also considered. Due to the Heisenberg uncertainty principle, intermediate states which are energetically forbidden also referred to as virtual states can occur only at very short time scales depending on the energy,  $t \sim E^{-1}$ . There are two possible intermediate states with a zero- or double-occupied

quantum dot, shown in Fig. 3.2.

Within the time scale  $t$ , a further tunnelling process must take place such that the final and initial states have the same total energy in order to make the virtual state possible. In the case of the Kondo effect, in the final state the electron must have the inverse spin of the initial state. This spin-flip process happens successively such that the quantum dot and lead electrons form a spin-singlet state and screen the spin on the quantum dot effectively. The formation of the spin-singlet is a macroscopically correlated state and leads to a sharp peak in the quantum dot's density of states at the Fermi energy, depicted in Fig. 3.2. The width of this peak is called the Kondo temperature,  $T_K$ , and only for smaller temperatures,  $T < T_K$ , do such processes become significant. The Kondo temperature can also be interpreted as the binding energy of the spin singlet. The side peaks corresponding to the two energy levels on the quantum dot are determined by the coupling to the leads,  $\Gamma$ .

The Kondo effect leads to an enhanced differential conductance at zero bias voltage and low temperatures. This was first proposed in Ref. [177] and observed in experiments by Goldhaber-Gordon *et al.* [21, 22] and Kouwenhoven *et al.* [23]. In the next section, we review the origin and the first steps in understanding the Kondo effect which led to the single impurity Anderson model.

### 3.3 Single Impurity Anderson Model

The origin of the motivation for the Anderson model goes back to 1936 when de Haas and van den Berg [178] measured the resistance of gold at low temperatures, up to  $T = 20$  K. They discovered at temperatures around  $T = 7.5$  K a minimum, which was not expected at that time for metals. With this, the resistance at low temperatures can be described by

$$R(T) = R_0 + AT^2 + BT^5 + C \ln\left(\frac{D}{T}\right), \quad (3.5)$$

where the first term,  $R_0$ , is the residual resistance coming from scattering events of conduction electrons with non-magnetic impurities, the second term is a Fermi gas contribution of the conduction electrons, the third term comes from the interaction of phonons with conduction electrons, and the, so far unknown, fourth term and was later linked with the scattering of conduction electrons with magnetic impurities which is the Kondo effect.

Almost two decades later in the 1950s, work by Zener [179], Yosida [180] and Friedel [181] led to the nowadays often called Kondo model<sup>2</sup>. The model describes an exchange spin interaction between an immobile local impurity spin and conduction electrons. The Hamiltonian reads

$$H = \sum_{k\sigma} \epsilon_k c_{k\sigma}^\dagger c_{k\sigma} + JS \cdot s \quad (3.6)$$

---

<sup>2</sup>This model is also called the  $s - d$  exchange model.

where  $c_{k\sigma}^\dagger$  and  $c_{k\sigma}$  creates and annihilates a conduction electron with energy  $\epsilon_k$  and spin  $\sigma$ ,  $J$  is the exchange coupling constant and  $S$  and  $s$  are the spin operators of the immobile impurity and conduction electrons. The formation of local moments<sup>3</sup> are not included in this model. In 1961, Anderson [20] suggested a more extensive model, which is named after him, and presented a Hartree–Fock calculation for the forming of local moments. Later Schrieffer and Wolff demonstrated that the single impurity Anderson model in the Kondo regime can be unitary transformed to the Kondo model [182]. Also in the early 1960s, the purity of the materials was drastically improved such that the resistance minimum could be connected to the magnetic impurities experimentally. In 1964, Kondo derived the logarithmic term in the resistance in Eq. (3.5) with a third-order perturbation expansion in the exchange coupling  $J$  from model then named after him [183]. It follows that, the resistance diverges for  $T \rightarrow 0$  which imposes that the perturbation theory must breakdown for very low temperatures. This was referred to as the Kondo problem. Only a year later, first non-perturbative calculations were carried out by Abrikosov [184], Suhl [185], Nagaoka [186], and Kondo [187], who suggested a resonant scattering at the Fermi edge that gives rise to a sharp resonance. For that reason, it should be called the Abrikosov–Suhl–Nagaoka–Kondo resonance. Nevertheless, all calculations diverge and could not be applied for temperatures far below the Kondo temperature. Furthermore, Anderson’s new poor man’s scaling idea [188] has the same fault. Nonetheless, this scaling idea led to Wilson’s numerical renormalisation group in 1975 [53]. With that, the first calculations far below the Kondo temperature could be performed.

Originally, the Anderson model was invented to explain the formation of local moments in bulk metals. The SIAM, which we introduce in the following subsection, perfectly models a quantum dot coupled to leads. A quantum dot provides the perfect possibility to study an isolated magnetic impurity in all detail because of the tunability of all parameters. This is in contrast to bulk metals and is a big advantage.

### 3.3.1 Hamiltonian and Action

The SIAM consists of three parts describing the quantum dot,  $H_D$ , the non-interacting metallic leads,  $H_L$ , and the tunnelling between leads and quantum dot,  $H_T$ ,

$$H = H_D + H_L + H_T \quad (3.7)$$

with

$$H_D = \sum_{\sigma} E_{0\sigma} n_{\sigma} + U n_{\uparrow} n_{\downarrow}, \quad (3.8)$$

$$H_L = \sum_{kp\sigma} (\epsilon_{kp} - \mu_p) c_{kp\sigma}^\dagger c_{kp\sigma}, \quad (3.9)$$

$$H_T = - \sum_{kp\sigma} (t_p c_{kp\sigma}^\dagger d_{\sigma} + t_p^* d_{\sigma}^\dagger c_{kp\sigma}), \quad (3.10)$$

---

<sup>3</sup>Local moments can be formed by magnetic impurities.

where  $\sigma = \pm 1/2 \simeq \uparrow, \downarrow$  denotes the spin index,  $p = \pm \simeq \text{L, R}$  labels the left and right leads, and  $k$  is the index of the spectrum of the lead electrons. The creation and annihilation operator of quantum dot electrons with spin  $\sigma$  are  $d_\sigma^\dagger$  and  $d_\sigma$ , hence, the occupation number operator of quantum dot electrons is given by  $n_\sigma = d_\sigma^\dagger d_\sigma$ . Analogously,  $c_{kp\sigma}^\dagger$  and  $c_{kp\sigma}$  creates and annihilates a lead electron. The single electron energy,  $E_0$ , is controlled by the gate voltage. In the presence of a magnetic field,  $B$ , the single electron energy is spin dependent due to the Zeeman splitting,  $E_{0\sigma} = E_0 + \sigma B$ .  $U$  is the interaction energy caused by the on-site Coulomb repulsion. Each lead has a chemical potential,  $\mu_p = peV_B$ , which forms a bias voltage<sup>4</sup>,  $V_B$ . The energies  $\epsilon_{kp\sigma}$  denote the single electron energies of the lead electrons. The tunnelling probability between leads and quantum dot is given by the parameter  $t_p$ , which we assume to be symmetric,  $t_L = t_R = \tau$ , throughout the thesis.

For the path integral approach to non-equilibrium physics, we need the corresponding action of the Hamiltonian given in Eq. (3.7). The action is determined by the Lagrangian which is a Legendre transform of the Hamiltonian. Therefore, the action reads

$$S = S_D + S_L + S_T \quad (3.11)$$

with

$$S_D = \int_{\mathcal{C}} dt \sum_{\sigma} d_{\sigma}^{\dagger} (i\partial_t - E_{0\sigma}) d_{\sigma} - U d_{\uparrow}^{\dagger} d_{\uparrow} d_{\downarrow}^{\dagger} d_{\downarrow}, \quad (3.12)$$

$$S_L = \int_{\mathcal{C}} dt \sum_{kp\sigma} c_{kp\sigma}^{\dagger} (i\partial_t - \epsilon_{kp} + \mu_p) c_{kp\sigma}, \quad (3.13)$$

$$S_T = \int_{\mathcal{C}} dt \sum_{kp\sigma} (t_p c_{kp\sigma}^{\dagger} d_{\sigma} + t_p^* d_{\sigma}^{\dagger} c_{kp\sigma}). \quad (3.14)$$

In the previous section, we discussed the Kondo effect and noticed that the temperature is very important for the system. Only below the Kondo temperature,  $T_K$ , do the necessary correlations between lead and quantum dot electrons prevail, which give rise to the Kondo peak in the quantum dot spectral function. The Kondo temperature was derived in Refs. [24–26] by applying the Bethe ansatz [189] to the SIAM and is given by

$$T_K = \sqrt{\frac{U\Gamma}{2}} \exp\left(-\frac{\pi U}{8\Gamma}\right) \quad (3.15)$$

in the particle-hole symmetric setup  $E_0 = -U/2$ , where  $\Gamma = 2\pi|\tau|^2\rho_L$  is the hybridisation between quantum dot and lead electrons. We assume a constant density of states,  $\rho_L$ , in the leads, see Sec. 4.4. Eq. (3.15) is valid for  $U \gg \Gamma$ .

### 3.3.2 Phase Diagram

The physics of the quantum dot is not determined by the total number of electrons but whether it has an even number, which is then a non-magnetic state, or an odd

---

<sup>4</sup>This is a different convention than that used in Sec. 3.1.

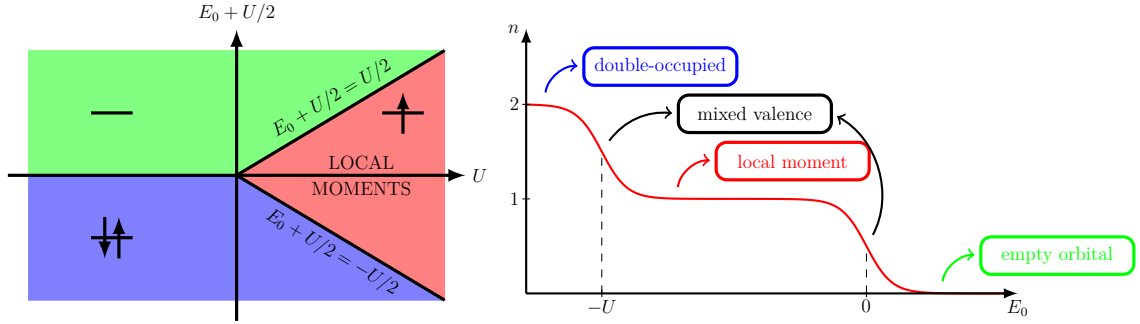


**Figure 3.3:** Illustrations of the phase diagram of the single impurity Anderson model. Depending on the interaction strength,  $U$ , and gate voltage,  $E_0$ , the quantum dot can be in four different regimes: the green marked area corresponds to the empty orbital, the blue area to the double occupied, the black lines between the green and red and blue and red areas to the mixed valence, and the red area to the local moments or Kondo regime. The mixed valence regime is not a sharp line as indicated on the left-hand side but rather a transition range of the order of  $\Gamma$  as depicted in the illustration on the right-hand side. The illustration on the left-hand side is inspired by Ref. [190]

number of electrons on the quantum dot, which is a magnetic state. This is why the SIAM is a very good approximation of a real quantum dot. In the SIAM, the non-magnetic states correspond to the unoccupied and double-occupied quantum dot, whereas the magnetic state corresponds to the single-occupied dot. The two non-magnetic states have a total energy<sup>5</sup> of

$$E_{\text{tot}}^0 = 0, \quad (3.16)$$

$$E_{\text{tot}}^2 = 2E_0 + U, \quad (3.17)$$

and for the magnetic state

$$E_{\text{tot}}^1 = E_0. \quad (3.18)$$

We assume that the quantum dot is single-occupied. If adding  $E_{\text{tot}}^2 - E_{\text{tot}}^1 = -E_0 > 0$ , and the removal of one electron costs energy,  $E_{\text{tot}}^0 - E_{\text{tot}}^1 = -E_0 > 0$ , then this state is stable. In this situation, the quantum dot is Coulomb blocked due to the on-site repulsion interaction. From this consideration, we find the condition for the local moment regime<sup>6</sup>, which is

$$\frac{U}{2} > E_0 + \frac{U}{2} > -\frac{U}{2}. \quad (3.19)$$

Strictly speaking, this consideration is only valid for zero temperature and in the limit of a vanishing coupling to the leads,  $\Gamma \rightarrow 0$ . This is shown on the left-hand

<sup>5</sup>This can be naively read off from the SIAM Hamiltonian. However, due to the on-site Coulomb repulsion, higher-order quantum corrections can change the exact values. We calculate the total energy of an isolated quantum dot in App. C.

<sup>6</sup>We use the term “local-moment regime” and “Kondo regime” interchangeably but the Kondo effect needs a finite coupling to the leads and lower temperatures.

side of Fig. 3.3 where the different regimes of the SIAM are only separated by a thin line. On the right-hand side, the total occupation number,  $n = n_{\uparrow} + n_{\downarrow}$ , is shown as a function of the gate voltage,  $E_0$ , for a fixed interaction strength,  $U$ , and a finite coupling to the leads,  $\Gamma$ , depicted as a continuous transition around the points  $E_0 = 0$  and  $E_0 = -U$ , the so-called mixed valence regime.

## 3.4 Summary

In this chapter, we introduced quantum dots and their physical foundations, in particular the tunability of important parameters determining the physics of the quantum dot. Moreover, we used a simple model to find an energy spectrum of the quantum dot.

Subsequently, we discussed the Kondo effect in a quantum dot in different physical situations. The Kondo effect requires higher-order cotunnelling processes because of the Coulomb blockade. The resulting intermediate state is energetically forbidden but due to the Heisenberg uncertainty principle, can happen within short time scales.

At the end, we introduced the standard model of quantum dots, which is the single impurity Anderson model (SIAM). Originally, Anderson proposed this model to describe the formation of local moments in bulk metals. However, it also describes quantum dots which were invented much later. We argued in which parameter space local moments are present in the SIAM. This is the most important aspect of the Kondo effect.





## Chapter 4

# Applying the Two-Particle Irreducible Effective Action to the Single Impurity Anderson Model

In the previous chapter, we stressed the importance of quantum dots in the field of condensed matter physics. This importance is due to the tunability of all quantities that affect the physics of such systems. We discussed the physical setup of real quantum dots. Moreover, we explained the Kondo effect in a quantum dot, which has a tremendous influence on the electrical charge transport property. Finally, we argued that the single impurity Anderson model (SIAM) is an appropriate model for describing quantum dots.

In this chapter, we apply the two-particle irreducible (2PI) effective action to the SIAM Hamiltonian and derive the specific dynamic equations that we can solve numerically. This model has two inconveniences: first, the interaction on the quantum dot, which is a two-body scattering process that gives rise to the four-fermion vertex, and second, the coupling to the leads. We start with the first point and hence, at first, we limit our consideration to an isolated quantum dot. Although the derived Kadanoff–Baym equations of motion for the full propagator are exact, they are not solvable without any truncation of the self-energy, which diagrammatically means not all Feynman diagrams can be taken into account. We begin with a loop expansion of the 2PI effective action and go on with a non-perturbative approximation to the 2PI part of the effective action,  $\Gamma_2$ , by summing up a certain class of Feynman diagrams to infinite order with the help of a Hubbard–Stratonovich transformation. For all considered approximations, we derive all the relevant equations to obtain the results we present in Ch. 5.

At the end of this chapter, we extend our considerations from a closed to an open system and discuss, in detail, how we treat the leads and implement them in our 2PI formalism. With this knowledge, we can introduce observables in which the leads play a tremendous role, like the linear and differential electrical conductance, as well as the electrical current through the quantum dot.

## 4.1 Dynamic Equations for the Single Impurity Anderson Model

In Ch. 2 we derived an exact equation for the two-point Green's function for a spatially zero-dimensional, non-relativistic fermionic system without any further specification to the model, especially concerning the interaction of the system. In the previous chapter, we introduced the SIAM, which describes a quantum dot coupled to finite temperature leads. We will, in this section, discuss the general shape of the Kadanoff–Baym equations of motion for the SIAM before we review approximations to the interaction of the system in order to make it possible to solve this equation numerically.

We consider a non-relativistic system at low temperatures and energies. Furthermore, the spin of each electron is assumed to be conserved. Thus, we assume that the two-point Green's function is diagonal in the spin space,  $D_{\sigma\lambda} \sim \delta_{\sigma\lambda}$ . Hence, we can write  $D_{\sigma\sigma} = D_\sigma$  without implying a sum over the same indices. Thereby, the two-point Green's function, which is a  $2 \times 2$  matrix in spin space, is reduced to its diagonal elements. With that, the Kadanoff–Baym equations of motion also simplify to

$$\begin{aligned} (i\partial_t - M_\sigma(t))\rho_\sigma(t, t') &= \int_{t'}^t du \Sigma_\sigma^\rho(t, u)\rho_\sigma(u, t') \\ (i\partial_t - M_\sigma(t))F_\sigma(t, t') &= \int_0^t du \Sigma_\sigma^\rho(t, u)F_\sigma(u, t') - \int_0^{t'} du \Sigma_\sigma^F(t, u)\rho_\sigma(u, t'), \end{aligned} \quad (4.1)$$

where the effective mass term

$$M_\sigma(t) = E_{0\sigma} + \Sigma_\sigma^{(0)}(t) \quad (4.2)$$

is given by the single electron energy,  $E_0$ , and the local self-energy contribution,  $\Sigma_\sigma^{(0)}$ , which will be determined in Subsec. 4.2.1. Also, the symmetries of the statistical propagator,  $F$ , and the spectral function,  $\rho$ , in Eq. (2.9) simplify to

$$F_\sigma(t, t') = F_\sigma^*(t', t), \quad \rho_\sigma(t, t') = -\rho_\sigma^*(t', t). \quad (4.3)$$

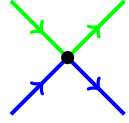
From these symmetries, it follows that the statistical propagator,  $F$ , has a symmetric real part and an anti-symmetric imaginary part, and that the spectral function,  $\rho$ , has an anti-symmetric real part and a symmetric imaginary part. For later times, when the system reaches equilibrium and both functions only depend on the difference of the times, the Fourier transform with respect to this gives a purely real statistical propagator and an imaginary spectral function in Fourier space.

In the following subsections, we show possible approximations to the 2PI part of the effective action.

## 4.2 Loop Expansion of the 2PI Effective Action

In the previous section, we derived the general exact dynamic equations for the isolated quantum dot. To solve these equations, we need an expression for the self-

energy entering the dynamic equations. In general, we have to take into account all two-particle irreducible (2PI) diagrams which can be constructed from the on-site quantum dot repulsive interaction term,

$$S_{\text{int}} = - \int_C dt U d_{\uparrow}^{\dagger} d_{\uparrow} d_{\downarrow}^{\dagger} d_{\downarrow} = \text{Diagram} . \quad (4.4)$$


This describes a two-to-two scattering process which couples up to down spins such that at each bare interaction vertex,  $U$  (black dot), one full propagator goes into the vertex and one out for spin up (blue line) and spin down (green line). This is problematic because it is impossible to write down a closed functional expression for all 2PI diagrams. Thus, we have to make some approximations or truncations to the 2PI part of the effective action and respectively to the self-energy. In this section, we perform a loop expansion of the 2PI effective action for which we rewrite the interaction part,

$$\Gamma_2[D] = \sum_{n=2}^{\infty} \Gamma_2^{(n)}[D], \quad (4.5)$$

as a sum of the number of bare interaction vertices appearing in all possible 2PI diagrams,

$$\Gamma_2^{(n)}[D] = -i \left\langle \frac{(iS_{\text{int}})^{n-1}}{(n-1)!} \right\rangle_{\text{2PI \& D}} . \quad (4.6)$$

The last equation means that we have to calculate the expectation value of a product of a certain number,  $n$ , of interaction terms but with the condition that the constructed diagram is 2PI and the propagator lines in the Feynman diagram are full propagators,  $D$ . This can be done by using Wick's theorem [191], for example.

Additionally, we introduce the  $n$ -loop approximation,

$$\Gamma_2^{(n \text{ loop})}[D] = \sum_{m=2}^n \Gamma_2^{(m)}[D] \quad \text{with } n \geq 2, \quad (4.7)$$

which is a sum of all 2PI diagrams constructed with up to  $n$  bare interaction vertices.

This procedure of loop expansion resembles the standard perturbation theory but it is important to note, at this stage, that they are not the same because in the Feynman diagrams, the solid lines represent full and not the free propagators. The full propagator is calculated self-consistently from Eq. (4.1) which means that each solid line consists of a multitude of diagrams up to an arbitrary power of bare vertices,  $U$ , depending on the chosen approximation. This is the reason why this type of approximation is called a loop expansion and not, as in perturbation theory, a coupling expansion.

In the following, we carry out this loop expansion for the first three orders explicitly and then give an outlook for higher orders.

### 4.2.1 Mean-Field or Hartree–Fock–Bogoliubov Approximation

We follow the instructions we introduced before and start with the simplest possible approximation, which is well-established as a mean-field or Hartree–Fock–Bogoliubov approximation [192–194]. To obtain this, we end the loop expansion in Eq. (4.7) after the first term and therefore the corresponding 2PI diagram is made of one bare vertex,  $U$ . Due to the structure of the bare vertex shown in Eq. (4.4), there is only one possibility for connecting the external legs to two full propagator lines,  $D$ . We need one for each spin to get a 2PI diagram,

$$\Gamma_2^{\text{MF}}[D] = -U \int_{\mathcal{C}} du D_{\uparrow}(u, u) D_{\downarrow}(u, u). \quad (4.8)$$

The corresponding Feynman diagram is<sup>1</sup>

$$\Gamma_2^{\text{MF}}[D] = \text{Diagram} \quad (4.9)$$

In the dynamic equations, the information of the chosen truncation enters via the self-energy. For this reason, we have to calculate the self-energy at mean-field order by taking the derivative of Eq. (4.9) with respect to the full fermion propagator,  $D$ , to obtain

$$\begin{aligned} \Sigma_{\sigma}^{\text{MF}}(t, t') &= iU \int_{\mathcal{C}} du \delta(u - t') \delta(u - t) D_{\bar{\sigma}}(u, u) \\ &= iU D_{\bar{\sigma}}(t, t) \delta(t - t') \\ &= -iU n_{\bar{\sigma}}(t) \delta(t - t') \end{aligned} \quad (4.10)$$

which corresponds to the Feynman diagrams

$$\Sigma_{\uparrow}(t, t') = \text{Diagram} , \quad \Sigma_{\downarrow}(t, t') = \text{Diagram} . \quad (4.11)$$

This shows the meaning of the functional derivative of the 2PI part of the effective action, which involves cutting and removing one full propagator line in the Feynman diagram, respectively.

In the last step of Eq. (4.10), we used a subtlety that needs further explanation. The propagator has a jump discontinuity at equal times and therefore, the value depends on the limit as we approach equal times and is ambiguous. To make this point clear, we look at the definition of the propagator in Eq. (2.1), which is the time-ordered expectation value of the annihilation and creation operators,

$$\begin{aligned} \lim_{\epsilon \rightarrow +0} D_{\sigma}(t, t - \epsilon) &= \langle d_{\sigma}(t) d_{\sigma}^{\dagger}(t) \rangle = 1 - n_{\sigma}(t) \\ \lim_{\epsilon \rightarrow +0} D_{\sigma}(t, t + \epsilon) &= -\langle d_{\sigma}^{\dagger}(t) d_{\sigma}(t) \rangle = -n_{\sigma}(t). \end{aligned} \quad (4.12)$$

<sup>1</sup>The lowest possible Feynman diagram for a four-point interaction is often called a double-bubble diagram.

The exact value for equal times is determined by the ordering of the operator in the Hamiltonian. The Hamiltonian in Eq. (3.7) corresponds to the latter value in Eq. (4.12). For more information, we refer to Ref. [145]. Since the lowest possible 2PI diagram consists of one bare vertex, the self-energy is only local in time and gives a contribution to the effective mass term,

$$M_\sigma(t) = E_{0\sigma} + Un_{\bar{\sigma}}(t). \quad (4.13)$$

The mean-field contribution shifts the bare one-particle energy level,  $E_0$ , by a value that is linear in occupation number and interaction strength. In the mean-field approximation, the occupation number is a constant in time because of the lack of non-local contributions to the self-energy that give rise to memory integrals. This changes when we go beyond the mean-field approximation in the repulsive interaction on the quantum dot or when we couple the quantum dot to external baths.

### Exact Solutions

Due to the simplicity of mean-field approximation, it is possible to find exact analytic solutions for the Kadanoff–Baym equations of motion. Since the self-energy contribution of the lowest possible 2PI diagram in  $\Gamma_2$  is local in time, the memory integrals on the right-hand side of Eq. (4.1) vanish. Therefore, the dynamic equations of motion become partial differential equations. We use Eq. (4.13) and yield the Kadanoff–Baym equations at mean-field order:

$$\begin{aligned} (i\partial_t - M_\sigma)\rho_\sigma(t, t') &= 0 \\ (i\partial_t - M_\sigma)F_\sigma(t, t') &= 0. \end{aligned} \quad (4.14)$$

Although the mean-field self-energy contribution, which is proportional to the occupation number, appears in the equation for the spectral function, both equations are not coupled because the occupation number is a constant at mean-field order for an isolated quantum dot. Thus, in the mean-field approximation, the Kadanoff–Baym equations of motion are simple, first-order differential equations with the conditions at equal times for the spectral function,  $\rho_\sigma(t, t) = i$ , and statistical propagator,  $F_\sigma(t, t) = 1/2 - n_\sigma$ . We find the analytic solutions

$$\begin{aligned} \rho_\sigma(t, t') &= ie^{-iM_\sigma(t-t')} \\ F_\sigma(t, t') &= \left(\frac{1}{2} - n_\sigma\right) e^{-iM_\sigma(t-t')}. \end{aligned} \quad (4.15)$$

The solutions are plane waves with angular frequency,  $M_\sigma$ , which is similar to the solution of a free theory but with shifted frequency. Since the solution only depends on the relative time coordinate, we apply a Wigner transform to the time variables  $t, t'$  and map them to the relative  $s = t - t'$  and absolute time  $T = (t + t')/2$  and

perform a Fourier transform of the spectral function with respect to the relative time coordinate. We obtain

$$\rho_\sigma(\omega) = 2\pi i \delta(\omega - M_\sigma), \quad (4.16)$$

which describes a sharp located peak and therefore, the state has an infinite lifetime  $t \sim \Gamma^{-1}$ , with the width  $\Gamma$ . This situation alters drastically when we couple the dot to external baths because then the dot electrons can tunnel off the quantum dot, which means that the state can decay in time and we expect a finite lifetime, *cf.* Sec. 4.4.

### 4.2.2 Second-Order Loop Expansion

In the next step, we go beyond mean-field approximations and take into account Feynman diagrams of up to two bare vertices  $U$ , which means up to three loops. Besides the two bare interaction vertices, the three loop Feynman diagram consists of four full propagator lines,  $D$  (two for each spin),

$$\begin{aligned} \Gamma_2^{(3 \text{ loop})}[D] = & -U \int_{\mathcal{C}} du D_\uparrow(u, u) D_\downarrow(u, u) \\ & + \frac{i}{2} U^2 \int_{\mathcal{C}} du du' D_\uparrow(u, u') D_\uparrow(u', u) D_\downarrow(u, u') D_\downarrow(u', u) \end{aligned} \quad (4.17)$$

and in diagrammatic language<sup>2</sup>

$$\Gamma_2^{(3 \text{ loop})}[D] = \text{Diagram 1} + \text{Diagram 2} \quad (4.18)$$

This expansion is also called the second-order Born approximation [195]. The way to connect the two bare vertices with full propagator lines stays unique even at second order. This behaviour will change in the next order of the loop expansion, which we will discuss in the following subsection. Since we already derived the self-energy of the first diagram in Eq. (4.18), we now compute the self-energy of the three loop diagram (basketball diagram) by taking the derivative with respect to the full propagator,  $D$ . We obtain

$$\begin{aligned} \Sigma_\sigma^{(3)}(t, t') = & \frac{U^2}{2} \int_{\mathcal{C}} du du' \delta(u - t') \delta(u' - t) D_\sigma(u', u) D_{\bar{\sigma}}(u, u') D_{\bar{\sigma}}(u', u) \\ & + \frac{U^2}{2} \int_{\mathcal{C}} du du' D_\sigma(u, u') \delta(u' - t') \delta(u - t) D_{\bar{\sigma}}(u, u') D_{\bar{\sigma}}(u', u) \\ = & U^2 D_\sigma(t, t') D_{\bar{\sigma}}(t, t') D_{\bar{\sigma}}(t', t) \end{aligned} \quad (4.19)$$

and in terms of Feynman diagrams<sup>3</sup>

$$\Sigma_\uparrow^{(3)}(t, t') = \text{Diagram 3}, \quad \Sigma_\downarrow^{(3)}(t, t') = \text{Diagram 4} \quad (4.20)$$

<sup>2</sup>The three loop diagram is often called a basketball diagram.

<sup>3</sup>The self-energy Feynman diagram corresponding to the three loop diagram of the 2PI effective action at second order is often called a sunset diagram.

Since the self-energy at second order is non-local in time, the contribution appears as memory integrals in the Kadanoff–Baym equations of motion. We split Eq. (4.19) into its spectral and statistical parts and obtain

$$\begin{aligned}\Sigma_{\sigma}^{\text{F}}(t, t') &= U^2 \left[ F_{\sigma}(t, t') \left( |F_{\bar{\sigma}}|^2(t, t') - \frac{1}{4} |\rho_{\bar{\sigma}}|^2(t, t') \right) \right. \\ &\quad \left. - \frac{1}{4} \rho_{\sigma}(t, t') \left( F_{\bar{\sigma}}(t, t') \rho_{\bar{\sigma}}^*(t, t') + F_{\bar{\sigma}}^*(t, t') \rho_{\bar{\sigma}}(t, t') \right) \right] \\ \Sigma_{\sigma}^{\rho}(t, t') &= U^2 \left[ \rho_{\sigma}(t, t') \left( |F_{\bar{\sigma}}|^2(t, t') - \frac{1}{4} |\rho_{\bar{\sigma}}|^2(t, t') \right) \right. \\ &\quad \left. - \frac{1}{4} F_{\sigma}(t, t') \left( F_{\bar{\sigma}}(t, t') \rho_{\bar{\sigma}}^*(t, t') + F_{\bar{\sigma}}^*(t, t') \rho_{\bar{\sigma}}(t, t') \right) \right],\end{aligned}\tag{4.21}$$

where we used the symmetry relations in Eq. (4.3) to bring the time arguments in the spectral function and statistical propagator to the same order.

With a look at Eq. (4.21), it becomes immediately clear that the Kadanoff–Baym equations of motion increase drastically in complexity in comparison to the mean-field order due to the non-local contribution to the self-energy. First of all, the dynamic equations are a closed set of coupled integro-differential equations and second, the equations are non-Markovian because of the memory integrals which describe many-body corrections. Even at second order the Kadanoff–Baym equations of motion are no longer analytically solvable and therefore, we need numerical techniques in order to obtain results from them.

### 4.2.3 Third-Order Loop Expansion

At third order or four loop expansion, the construction of 2PI diagrams is no longer unique and we get more terms that we have to take into consideration. The 2PI part of the effective action,  $\Gamma_2$ , reads

$$\begin{aligned}\Gamma_2^{(4)}[D] &= \frac{U^3}{6} \sum_{\sigma} \int_{\mathcal{C}} dx dy dz \\ &\quad \left( D_{\sigma}(x, y) D_{\bar{\sigma}}(y, x) D_{\sigma}(y, z) D_{\bar{\sigma}}(z, y) D_{\sigma}(z, x) D_{\bar{\sigma}}(x, z) \right. \\ &\quad \left. + D_{\sigma}(x, y) D_{\bar{\sigma}}(x, y) D_{\sigma}(y, z) D_{\bar{\sigma}}(y, z) D_{\sigma}(z, x) D_{\bar{\sigma}}(z, x) \right)\end{aligned}\tag{4.22}$$

and diagrammatically

$$\Gamma_2^{(4)}[D] = \text{Diagram 1} + \text{Diagram 2} + \text{Diagram 3} + \text{Diagram 4}.\tag{4.23}$$

These diagrams consist of three bubbles, where the first and the last are connected to each other. In every bubble, the propagators have opposite spin but either with propagators directed in the same or in opposite directions. A third possibility,

with alternating spin bubbles, can only occur with an even number of bare vertices because otherwise four propagators with the same spin would be connected to one vertex. We can compare this to the Feynman diagram with one less vertex. As we discussed before, there is only one way to write down a 2PI diagram but we can look at it in the aforementioned manner. While the first two mentioned topologies of Feynman diagrams exist at all orders starting with two bare vertices, the other exists only for an even number of bare interaction vertices. In the next section, we introduce a non-perturbative resummation scheme where we sum up a special class of Feynman diagrams to all orders. We will recover these three topologies of diagrams and distinguish three different channel resummations.

Taking the functional derivative of Eq. (4.22) with respect to the full propagator we obtain

$$\begin{aligned} \Sigma_{\sigma}^{(4)}(t, t') = & -iU^3 \left( D_{\bar{\sigma}}(t, t') \int_{\mathcal{C}} dz D_{\sigma}(t, z) D_{\bar{\sigma}}(z, t) D_{\sigma}(z, t') D_{\bar{\sigma}}(t', z) \right. \\ & \left. + D_{\bar{\sigma}}(t', t) \int_{\mathcal{C}} dz D_{\sigma}(t, z) D_{\bar{\sigma}}(t, z) D_{\sigma}(z, t') D_{\bar{\sigma}}(z, t') \right) \end{aligned} \quad (4.24)$$

and in Feynman diagrams

$$\begin{aligned} \Sigma_{\uparrow}^{(4)}(t, t') = & \text{Diagram 1} + \text{Diagram 2} + \text{Diagram 3} + \text{Diagram 4}, \\ \Sigma_{\downarrow}^{(4)}(t, t') = & \text{Diagram 5} + \text{Diagram 6} + \text{Diagram 7} + \text{Diagram 8}. \end{aligned} \quad (4.25)$$

We decompose the self-energy into its statistical,

$$\begin{aligned} \Sigma_{\sigma}^{\text{F}}(t, t') = & U^3 \left[ -F_{\bar{\sigma}}(t, t') \left( \int_0^t dz (\rho_{\sigma} F_{\bar{\sigma}}^* + F_{\sigma} \rho_{\bar{\sigma}}^*)(t, z) (F_{\sigma}^* F_{\bar{\sigma}} - \frac{1}{4} \rho_{\sigma}^* \rho_{\bar{\sigma}})(t', z) \right. \right. \\ & \left. \left. + \int_0^{t'} dz (F_{\sigma} F_{\bar{\sigma}}^* - \frac{1}{4} \rho_{\sigma} \rho_{\bar{\sigma}}^*)(t, z) (\rho_{\sigma}^* F_{\bar{\sigma}} + F_{\sigma}^* \rho_{\bar{\sigma}})(t', z) \right) \right. \\ & - \frac{1}{4} \rho_{\bar{\sigma}}(t, t') \int_{t'}^t dz (\rho_{\sigma} F_{\bar{\sigma}}^* + F_{\sigma} \rho_{\bar{\sigma}}^*)(t, z) (\rho_{\sigma}^* F_{\bar{\sigma}} + F_{\sigma}^* \rho_{\bar{\sigma}})(t', z) \\ & - F_{\bar{\sigma}}(t', t) \left( \int_0^t dz (\rho_{\sigma} F_{\bar{\sigma}} + F_{\sigma} \rho_{\bar{\sigma}})(t, z) (F_{\sigma} F_{\bar{\sigma}} - \frac{1}{4} \rho_{\sigma} \rho_{\bar{\sigma}})(t', z) \right. \\ & \left. \left. + \int_0^{t'} dz (F_{\sigma} F_{\bar{\sigma}} - \frac{1}{4} \rho_{\sigma} \rho_{\bar{\sigma}})(t, z) (\rho_{\sigma} F_{\bar{\sigma}} + F_{\sigma} \rho_{\bar{\sigma}})(t', z) \right) \right. \\ & \left. - \frac{1}{4} \rho_{\bar{\sigma}}(t', t) \int_{t'}^t dz (\rho_{\sigma} F_{\bar{\sigma}} + F_{\sigma} \rho_{\bar{\sigma}})(t, z) (\rho_{\sigma} F_{\bar{\sigma}} + F_{\sigma} \rho_{\bar{\sigma}})(t', z) \right], \end{aligned} \quad (4.26)$$



and spectral part,

$$\begin{aligned}
 \Sigma_\sigma^p(t, t') = U^3 & \left[ -\rho_{\bar{\sigma}}(t, t') \left( \int_0^t dz (\rho_\sigma F_{\bar{\sigma}}^* + F_\sigma \rho_{\bar{\sigma}}^*)(t, z) (F_\sigma^* F_{\bar{\sigma}} - \frac{1}{4} \rho_\sigma^* \rho_{\bar{\sigma}}) (t', z) \right. \right. \\
 & \left. \left. + \int_0^{t'} dz (F_\sigma F_{\bar{\sigma}}^* - \frac{1}{4} \rho_\sigma \rho_{\bar{\sigma}}^*)(t, z) (\rho_\sigma^* F_{\bar{\sigma}} + F_\sigma^* \rho_{\bar{\sigma}}) (t', z) \right) \right. \\
 & + F_{\bar{\sigma}}(t, t') \int_{t'}^t dz (\rho_\sigma F_{\bar{\sigma}}^* + F_\sigma \rho_{\bar{\sigma}}^*)(t, z) (\rho_\sigma^* F_{\bar{\sigma}} + F_\sigma^* \rho_{\bar{\sigma}}) (t', z) \\
 & - \rho_{\bar{\sigma}}(t', t) \left( \int_0^t dz (\rho_\sigma F_{\bar{\sigma}} + F_\sigma \rho_{\bar{\sigma}}) (t, z) (F_\sigma F_{\bar{\sigma}} - \frac{1}{4} \rho_\sigma \rho_{\bar{\sigma}}) (t', z) \right. \\
 & \left. \left. + \int_0^{t'} dz (F_\sigma F_{\bar{\sigma}} - \frac{1}{4} \rho_\sigma \rho_{\bar{\sigma}}) (t, z) (\rho_\sigma F_{\bar{\sigma}} + F_\sigma \rho_{\bar{\sigma}}) (t', z) \right) \right. \\
 & \left. \left. + F_{\bar{\sigma}}(t', t) \int_{t'}^t dz (\rho_\sigma F_{\bar{\sigma}} + F_\sigma \rho_{\bar{\sigma}}) (t, z) (\rho_\sigma F_{\bar{\sigma}} + F_\sigma \rho_{\bar{\sigma}}) (t', z) \right] , \tag{4.27}
 \end{aligned}$$

where we used the shorthand notation  $(\rho_\sigma F_{\bar{\sigma}}^* + F_\sigma \rho_{\bar{\sigma}}^*)(t, z) = \rho_\sigma(t, z) F_{\bar{\sigma}}^*(t, z) + F_\sigma(t, z) \rho_{\bar{\sigma}}^*(t, z)$ . These equations make clear that not only the number of possible diagrams increases with the order  $n$  but also the complexity of the resulting equations. This is obvious because the functional derivative with respect to the full propagator,  $D$ , cancels two time integrations in the effective action, therefore  $n - 2$  remain. If one of those integrations is left in the self-energy, we can manage to solve the Kadanoff–Baym equations of motion numerically. In general, it is also possible to solve them with more integrations but the computation time increases drastically and so either the time step size must be large or only short times can be considered in the time evolution. In both cases, we cannot expect to observe physics of interest in our research.

#### 4.2.4 Higher-Order Loop Expansion

We could go on with the procedure introduced in Sec. 4.2 to even higher orders but this becomes very tedious and, for practical purposes, not feasible. Thus, we limit our discussion of higher-order loop expansion of the effective action to the Feynman diagram representation. Possible Feynman diagrams with four bare interaction

vertices are given by

$$\begin{aligned}
 \Gamma_2^{\text{HO}}[D] = & \text{Diagram 1} + \text{Diagram 2} + \text{Diagram 3} + \text{Diagram 4} \\
 & + \text{Diagram 5} + \text{Diagram 6} + \text{Diagram 7} + \text{Diagram 8} \\
 & + \text{Diagram 9} + \text{Diagram 10} + \text{Diagram 11} + \dots
 \end{aligned} \tag{4.28}$$

Besides the first three diagrams that we have recognised in the previous subsection as three possible kinds of diagram that appear for every even number of bare vertices (the first diagram)<sup>4</sup> and for any number (the next two diagrams)<sup>5</sup>, Feynman diagrams appear with a novel structure that could not have been assembled with fewer bare interaction vertices. In comparison to the three aforementioned topologies, these new diagrams cannot be regarded as a sequence of bubbles where the first and the last are connected to each other. This is because the full propagators depicted inside the outer circle do not link two adjacent but the vis-à-vis bare interaction vertices. For this reason, these diagrams will not be considered in the leading-order non-perturbative channel resummation of the 2PI effective action in the next section.

<sup>4</sup>In the next section, these diagrams will appear in the direct (s)-channel resummation.

<sup>5</sup>The first two diagrams will later appear in the particle-hole (u)-channel resummation and the last two in the particle-particle (t)-channel resummation.

### 4.3 Non-Perturbative Resummation of the 2PI Effective Action

In the previous section, we performed a loop expansion of the 2PI effective action and showed the expansion starting from the leading-order expansion in  $U$ , which is mean-field with a ‘double-bubble’ diagram, continuing with a second-order ‘basketball’ diagram and ending with the third order. In this section, we summarise the resummation of certain classes of diagrams to infinite order. This procedure clearly goes beyond the previous discussed loop expansion. In particular, we will consider summations of s-, t- and u-channel bubbles, often also termed resummations in the direct, particle-particle, and particle-hole channels. In the direct (s)-channel, bubbles with alternating spins make up the chains where, in each bubble, the two propagators describe the same spin component. This is similar to the next-to-leading-order  $1/N$  approximation for  $N$ -component scalar fields [107, 113] and fermionic fields [126]. In the particle-particle (t)- and particle-hole (u)-channels, each bubble consists of two opposite spins propagating in the parallel or anti-parallel directions, *i.e.* ordering of  $d_\sigma$  and  $d_\sigma^\dagger$  in the propagator, distinguishing between the so-called particle-particle (t)- and particle-hole (u)-interactions. In this thesis, we extend the prior work in Ref. [145] by the particle-particle (t)-, particle-hole (u)-, and newly defined stu-channel calculations.

#### 4.3.1 Hubbard–Stratonovich Transformation

The Hubbard–Stratonovich transformation [196, 197] provides an elegant way to perform this resummation. This transformation uses a kind of bosonisation where two fermionic operators in the four-point interaction term are replaced by an auxiliary bosonic field. Due to four different fermionic operators, there are three ways of doing this which are related to the three types of resummations. The Hubbard–Stratonovich transformation converts the four-point interaction vertex to a Yukawa-like coupling<sup>6</sup> term, where two fermionic fields are coupled to one auxiliary bosonic field and the resulting new action is Gaussian in the new fields. Due to the integrability of these integrals, this transformation is exact.

We use the substitution for the on-dot interaction term

$$- J_\xi^T A^{-1} J_\xi \rightarrow \chi^T A \chi + 2 J_\xi^T \chi \quad (4.29)$$

with

$$\chi = \begin{pmatrix} \chi_1 \\ \chi_2 \end{pmatrix}, \quad A = \frac{1}{2U} \begin{pmatrix} 0 & 1 \\ 1 & 0 \end{pmatrix}, \quad A^{-1} = 2U \begin{pmatrix} 0 & 1 \\ 1 & 0 \end{pmatrix}, \quad (4.30)$$

where  $\chi$  is a vector with the new auxiliary bosonic fields  $\chi_1$  and  $\chi_2$ ,  $A$  is a matrix,

---

<sup>6</sup>In elementary particle physics, the Yukawa interaction describes the interaction of a Higgs boson with two fermions. This can be generalised to an interaction of an arbitrary scalar field to fermionic fields.

$A^{-1}$  is its inverse matrix, and the  $J$  operators are given by

$$J_s = \frac{1}{2} \begin{pmatrix} d_\uparrow^\dagger d_\uparrow \\ d_\downarrow^\dagger d_\downarrow \end{pmatrix}, \quad J_t = \frac{1}{2} \begin{pmatrix} d_\uparrow^\dagger d_\downarrow^\dagger \\ d_\downarrow d_\uparrow \end{pmatrix}, \quad J_u = \frac{1}{2} \begin{pmatrix} d_\uparrow^\dagger d_\downarrow \\ d_\uparrow d_\downarrow^\dagger \end{pmatrix}. \quad (4.31)$$

This corresponds to the three kinds of bosonisation we take into consideration. If we put all this into Eq. (4.29), we obtain, on the left-hand side, the on-dot interaction term shown in Eq. (3.8) and on the right-hand side, the free part for the quantum dot electrons, which gives the new transformed action

$$S_{\text{dot}} = \int_{\mathcal{C}} dt \left( \sum_{\sigma} d_{\sigma}^{\dagger} (i\partial_t - E_{0\sigma}) d_{\sigma} + \frac{1}{U} \chi_1 \chi_2 + \mathcal{L}_{\text{int},\xi} \right). \quad (4.32)$$

The new Yukawa interaction Lagrange densities, which are resummation scheme dependent interaction terms, ( $\xi = \text{s, t, u}$ ), are

$$\mathcal{L}_{\text{int},\text{s}} = d_{\uparrow}^{\dagger} d_{\uparrow} \chi_1 + d_{\downarrow}^{\dagger} d_{\downarrow} \chi_2, \quad (4.33)$$

$$\mathcal{L}_{\text{int},\text{t}} = d_{\uparrow}^{\dagger} d_{\downarrow}^{\dagger} \chi_1 + d_{\downarrow} d_{\uparrow} \chi_2, \quad (4.34)$$

$$\mathcal{L}_{\text{int},\text{u}} = d_{\uparrow}^{\dagger} d_{\downarrow} \chi_1 + d_{\uparrow} d_{\downarrow}^{\dagger} \chi_2. \quad (4.35)$$

The free inverse propagator for the fermions,  $D_0^{-1}$ , and the auxiliary bosonic fields,  $G_0^{-1}$ , is given by the quadratic part of the action or the second derivative of the action with respect to the fields, that is

$$\begin{aligned} iG_0^{-1}(t, t') &= 2A\delta(t - t'), \\ iD_{0,\sigma}^{-1}(t, t') &= (i\partial_t - E_{0\sigma})\delta(t - t') + \begin{cases} \bar{\chi}_{\sigma}\delta(t - t') & \text{for s-channel} \\ 0 & \text{otherwise} \end{cases}. \end{aligned} \quad (4.36)$$

The free inverse propagator,  $G_0^{-1}$ , is a  $2 \times 2$  matrix, where  $G$  denotes the resummed full bosonic propagator and  $\bar{\chi}_{\sigma}$  is the expectation value of the bosonic fields,  $\chi_{\sigma}$ . The corresponding 2PI effective action can be written as

$$\begin{aligned} \Gamma[G, D, \bar{\chi}] &= S_{\text{dot},\xi}[\bar{\chi}] - i \text{Tr}[\ln D^{-1} + D_0^{-1} D] \\ &\quad + \frac{i}{2} \text{Tr}[\ln G^{-1} + G_0^{-1} G] + \Gamma_2[D, G], \end{aligned} \quad (4.37)$$

where  $\Gamma_2$  includes all 2PI diagrams according to the new three-point Yukawa vertices in Eqs. (4.33), (4.34), and (4.35) with the full fermionic and bosonic propagators. In the following subsections, we present the lowest-order contribution for the three channels explicitly.

The self-energy of the quantum dot electrons and the auxiliary bosonic fields is given by the derivative of the 2PI part of the effective action with respect to the full propagators,

$$\begin{aligned} \Sigma_{\sigma}(t, t') &= -i \frac{\delta \Gamma_2[G, D]}{\delta D_{\sigma}(t', t)}, \\ \Pi_{\sigma\lambda}(t, t') &= 2i \frac{\delta \Gamma_2[G, D]}{\delta G_{\lambda\sigma}(t', t)}. \end{aligned} \quad (4.38)$$

From the stationary condition, we obtain the equations of motion for the propagators or two-point functions for the dot electrons and the auxiliary bosonic fields

$$\begin{aligned}\frac{\delta\Gamma}{\delta D} &= -i(-D^{-1} + D_0^{-1}) + i\Sigma = 0 &\Rightarrow & D_0^{-1} = D^{-1} + \Sigma \\ \frac{\delta\Gamma}{\delta G} &= \frac{i}{2}(-G^{-1} + G_0^{-1}) - \frac{i}{2}\Pi = 0 &\Rightarrow & G_0^{-1} = G^{-1} + \Pi.\end{aligned}\quad (4.39)$$

For both propagators, we get the Dyson equation but the self-energies are, in general, functionals of the fermionic, as well as the bosonic, full propagators.

We convolve the Dyson equation for the auxiliary bosonic fields with the free propagator,  $G_0$ , from the left and the full propagator,  $G$ , from the right,

$$G(t, t') = G_0(t, t') + (G_0 * \Pi * G)(t, t'), \quad (4.40)$$

where the asterisk denotes a convolution along the Keldysh contour,  $\mathcal{C}$ ,

$$\begin{aligned}(iA * B)(t, t') &= \int_{\mathcal{C}} du iA(t, u)B(u, t') \\ &= \int_0^t du A^\rho(t, u)B^F(u, t') - \int_0^{t'} du A^F(t, u)B^\rho(u, t') \\ &\quad - \frac{i}{2} \text{sgn}(t - t') \int_{t'}^t du A^\rho(t, u)B^\rho(u, t').\end{aligned}\quad (4.41)$$

The free propagator of the auxiliary bosonic fields,  $G_0$ , is the functional inverse of the first line in Eq. (4.36), that is  $\int du G_0^{-1}(t, u)G_0(u, t') = \mathbb{1}\delta(t - t')$  and we obtain

$$G_0(t, t') = \frac{i}{2}A^{-1}\delta(t - t') = iU\sigma_1\delta(t - t') = \tilde{G}_0\delta(t - t'). \quad (4.42)$$

We defined  $\tilde{G}_0 = iU\sigma_1$  with  $\sigma_1$ , the first Pauli matrix. We yield for the convolution of the free propagator with the self-energy of the auxiliary bosonic fields

$$(G_0 * \Pi)(t, t') = \int_{\mathcal{C}} du \tilde{G}_0\delta(t - u)\Pi(u, t') = iU \begin{pmatrix} \Pi_{21} & \Pi_{22} \\ \Pi_{11} & \Pi_{12} \end{pmatrix} (t, t'). \quad (4.43)$$

Solving the Dyson equation for the auxiliary bosonic fields iteratively, we obtain

$$\begin{aligned}G(t, t') &= iU \begin{pmatrix} 0 & 1 \\ 1 & 0 \end{pmatrix} \delta(t - t') - U^2 \begin{pmatrix} \Pi_{22} & \Pi_{21} \\ \Pi_{12} & \Pi_{11} \end{pmatrix} (t, t') \\ &\quad - iU^3 \begin{pmatrix} \Pi_{21} * \Pi_{22} + \Pi_{22} * \Pi_{12} & \Pi_{21} * \Pi_{21} + \Pi_{22} * \Pi_{11} \\ \Pi_{11} * \Pi_{22} + \Pi_{12} * \Pi_{12} & \Pi_{11} * \Pi_{21} + \Pi_{12} * \Pi_{11} \end{pmatrix} (t, t') + \mathcal{O}(U^4).\end{aligned}\quad (4.44)$$

The solution is a sum of bubbles represented by different  $\Pi$  at all orders. We explained the general approach for the resummation of an infinite number of Feynman diagrams of a certain class. In the following subsection, we derive the equations we need to solve the Kadanoff–Baym equations of motion in this approximation scheme for the three channels in the lowest order, which means including one resummed bosonic full propagator. At the end of this section, we give an outlook beyond the leading-order resummation.

### 4.3.2 Direct (s)-Channel Resummation

We start the discussion of the direct (s)-channel resummation with the equations of motion for the one-point functions of the auxiliary bosonic fields from the variation or functional derivative of the effective action with respect to the fields

$$\begin{aligned}\frac{\delta\Gamma(t)}{\delta\bar{\chi}_1(t)} &= \frac{1}{U}\bar{\chi}_2(t) - D_\uparrow(t, t) = 0 &\Rightarrow & \bar{\chi}_2 = UD_\uparrow(t, t) \\ \frac{\delta\Gamma(t)}{\delta\bar{\chi}_2(t)} &= \frac{1}{U}\bar{\chi}_1(t) - D_\downarrow(t, t) = 0 &\Rightarrow & \bar{\chi}_1 = UD_\downarrow(t, t).\end{aligned}\quad (4.45)$$

The expectation values of the auxiliary bosonic fields give the mean-field contribution, *cf.* Eq. (4.10), which enters the fermion's free inverse propagator, Eq. (4.36), and shifts the bare one particle energy  $E_0$ , *cf.* Eq. (4.13). From the new Yukawa couplings given in Eq. (4.33), we have to construct the lowest possible 2PI diagram to get the leading-order term in the s-channel resummation which reads

$$\Gamma_{2,s}[G, D] = \frac{i}{2} \sum_{\sigma} \int_{\mathcal{C}} du du' D_{\sigma}(u, u') D_{\sigma}(u', u) G_{\sigma\sigma}(u, u') \quad (4.46)$$

and in Feynman diagrams

$$\Gamma_{2,s}[G, D] = \text{Diagram 1} + \text{Diagram 2}. \quad (4.47)$$

The blue and green solid lines correspond to the spin up and down full fermion propagator and the wiggly line denotes the resummed bosonic propagator. From the  $\Gamma_2$  part of the effective action given in Eq. (4.46), we can compute the self-energy of the auxiliary fields as

$$\begin{aligned}\Pi_{\sigma\sigma}(t, t') &= -D_{\sigma}(t, t') D_{\sigma}(t', t) = \Pi_{\sigma\sigma}(t', t), \\ \Pi_{\sigma\bar{\sigma}}(t, t') &= 0\end{aligned}\quad (4.48)$$

and diagrammatically

$$\Pi_{\uparrow\uparrow}(t, t') = \text{Diagram 1}, \quad \Pi_{\downarrow\downarrow}(t, t') = \text{Diagram 2}, \quad (4.49)$$

which represents a bubble with the same spins but opposite directions. We then split Eq. (4.48) into its statistical and spectral parts,

$$\begin{aligned}-\Pi_{\sigma\sigma}^{\text{F}}(t, t') &= |F_{\sigma}|^2(t, t') - \frac{1}{4} |\rho_{\sigma}|^2(t, t'), \\ -\Pi_{\sigma\sigma}^{\rho}(t, t') &= 2\Re\left(\rho_{\sigma}(t, t') F_{\sigma}^*(t, t')\right).\end{aligned}\quad (4.50)$$

### 4.3 Non-Perturbative Resummation of the 2PI Effective Action

Similar to the self-energy of the auxiliary bosonic fields, we obtain for the fermions' self-energy

$$\begin{aligned}\Sigma_\sigma(t, t') &= -i \frac{\delta \Gamma_2[G, D]}{\delta D_\sigma(t', t)} = \frac{1}{2} D_\sigma(t, t') \left( G_{\sigma\sigma}(t, t') + G_{\sigma\sigma}(t', t) \right) \\ &= D_\sigma(t, t') G_{\sigma\sigma}(t, t'),\end{aligned}\quad (4.51)$$

where we have used the symmetry relation  $G_{\sigma\sigma}(t, t') = G_{\sigma\sigma}(t', t)$  which is a direct result of the symmetries of the bosonic self-energy bubbles in Eq. (4.48). Diagrammatically, it reads

$$\Sigma_\uparrow(t, t') = \text{diagram with blue arc and red wavy line}, \quad \Sigma_\downarrow(t, t') = \text{diagram with green arc and red wavy line}.\quad (4.52)$$

We split the fermion self-energy into its statistical and spectral parts,

$$\begin{aligned}\Sigma_\sigma^{\text{F}}(t, t') &= F_\sigma(t, t') G_{\sigma\sigma}^{\text{F}}(t, t') - \frac{1}{4} \rho_\sigma(t, t') G_{\sigma\sigma}^\rho(t, t'), \\ \Sigma_\sigma^\rho(t, t') &= \rho_\sigma(t, t') G_{\sigma\sigma}^{\text{F}}(t, t') + F_\sigma(t, t') G_{\sigma\sigma}^\rho(t, t').\end{aligned}\quad (4.53)$$

From Eq. (4.48), it follows that the self-energy of the auxiliary bosonic fields has vanishing off-diagonal elements and the diagonal remains because the propagators occurring in Eq. (4.46) have the same spin indices. The solution for the full resummed bosonic propagator in the direct (s)-channel can be read off from Eq. (4.44) with Eq. (4.48) as

$$\begin{aligned}G &= iU \begin{pmatrix} 0 & 1 \\ 1 & 0 \end{pmatrix} \delta - U^2 \begin{pmatrix} \Pi_{22} & 0 \\ 0 & \Pi_{11} \end{pmatrix} - iU^3 \begin{pmatrix} 0 & \Pi_{22} * \Pi_{11} \\ \Pi_{11} * \Pi_{22} & 0 \end{pmatrix} \\ &+ U^4 \begin{pmatrix} \Pi_{22} * \Pi_{11} * \Pi_{22} & 0 \\ 0 & \Pi_{11} * \Pi_{22} * \Pi_{11} \end{pmatrix} + \dots,\end{aligned}\quad (4.54)$$

where we have suppressed the time arguments. Since only the diagonal elements appearing in the self-energy of the fermions in Eq. (4.51) are those entering the Kadanoff–Baym equations of motion, we write down the Feynman diagrammatic representation of the diagonal elements of the full bosonic propagator,  $G$ ,

$$\text{red wavy line} = \left\{ \begin{array}{l} \text{diagram 1} + \text{diagram 2} + \mathcal{O}(U^6) \\ \text{diagram 3} + \text{diagram 4} + \mathcal{O}(U^6), \end{array} \right.\quad (4.55)$$

where the two cases belong to the two possible leading-order 2PI diagrams shown in Eq. (4.47). The elements of the full bosonic propagator,  $G$ , can be written as coupled

recursive equations,

$$\begin{aligned} G_{\sigma\sigma}(t, t') &= iU(\Pi_{\bar{\sigma}\bar{\sigma}} * G_{\bar{\sigma}\sigma})(t, t') - U^2\Pi_{\bar{\sigma}\bar{\sigma}}(t, t'), & G_{\bar{\sigma}\sigma}(t, t') &= iU(\Pi_{\sigma\sigma} * G_{\sigma\sigma})(t, t'), \\ G_{\bar{\sigma}\bar{\sigma}}(t, t') &= iU(\Pi_{\sigma\sigma} * G_{\sigma\bar{\sigma}})(t, t') - U^2\Pi_{\sigma\sigma}(t, t'), & G_{\sigma\bar{\sigma}}(t, t') &= iU(\Pi_{\bar{\sigma}\bar{\sigma}} * G_{\bar{\sigma}\bar{\sigma}})(t, t'). \end{aligned} \quad (4.56)$$

These equations can be split into statistical and spectral components with Eq. (4.41) and we have used this to calculate the effective coupling in App. B.1.

### 4.3.3 Particle-Particle (t)-Channel Resummation

We follow exactly the same steps as in the previous subsection for the direct (s)-channel resummation to derive all the relevant equations we need in order to solve the Kadanoff–Baym equations of motion. Unlike in the direct (s)-channel, the expectation value of the auxiliary bosonic fields vanishes,

$$\frac{\delta\Gamma}{\delta\bar{\chi}_1} = \frac{\delta\Gamma}{\delta\bar{\chi}_2} = 0. \quad (4.57)$$

Hence, the mean-field contribution must come along with the resummed bosonic propagator. We construct the lowest possible 2PI diagram from the Yukawa coupling in Eq. (4.34), which reads

$$\Gamma_{2,t}[G, D] = \frac{i}{2} \sum_{\sigma} \int_{\mathcal{C}} du du' D_{\sigma}(u, u') D_{\bar{\sigma}}(u, u') G_{\sigma\bar{\sigma}}(u', u) \quad (4.58)$$

and in the Feynman diagram representation

$$\Gamma_{2,t}[G, D] = \text{Diagram 1} + \text{Diagram 2}. \quad (4.59)$$

Due to the mixed spin indices appearing in the  $\Gamma_2$  part of the effective action in Eq. (4.58), the self-energy of the auxiliary bosonic fields has only off-diagonal entries,

$$\begin{aligned} \Pi_{\sigma\bar{\sigma}}(t, t') &= -D_{\sigma}(t, t') D_{\bar{\sigma}}(t, t') = \Pi_{\bar{\sigma}\sigma}(t, t'), \\ \Pi_{\sigma\sigma}(t, t') &= 0 \end{aligned} \quad (4.60)$$

with the corresponding Feynman diagram

$$\Pi_{\uparrow\downarrow}(t, t') = \text{Diagram} = \Pi_{\downarrow\uparrow}(t, t'), \quad (4.61)$$

which is a bubble with opposite spins but with the same direction. We split the self-energy into its statistical and spectral parts,

$$\begin{aligned} -\Pi_{\sigma\bar{\sigma}}^{\text{F}}(t, t') &= F_{\sigma}(t, t') F_{\bar{\sigma}}(t, t') - \frac{1}{4} \rho_{\sigma}(t, t') \rho_{\bar{\sigma}}(t, t'), \\ -\Pi_{\sigma\bar{\sigma}}^{\text{S}}(t, t') &= \rho_{\sigma}(t, t') F_{\bar{\sigma}}(t, t') + F_{\sigma}(t, t') \rho_{\bar{\sigma}}(t, t'). \end{aligned} \quad (4.62)$$



### 4.3 Non-Perturbative Resummation of the 2PI Effective Action

The fermion self-energy follows from taking the derivative of Eq. (4.60) with respect to the full fermionic propagator,  $D$ ,

$$\Sigma_\sigma(t, t') = \frac{1}{2} D_{\bar{\sigma}}(t', t) \left( G_{\sigma\bar{\sigma}}(t, t') + G_{\bar{\sigma}\sigma}(t, t') \right) = D_{\bar{\sigma}}(t', t) G_{\sigma\bar{\sigma}}(t, t'), \quad (4.63)$$

where we took advantage of the symmetry relation  $G_{\sigma\bar{\sigma}}(t, t') = G_{\bar{\sigma}\sigma}(t, t')$  coming from the symmetry of the bosonic self-energy in Eq. (4.60). Diagrammatically, it reads

$$\Sigma_\uparrow(t, t') = \text{diagram with green and red arcs}, \quad \Sigma_\downarrow(t, t') = \text{diagram with blue and red arcs}. \quad (4.64)$$

The statistical and spectral parts of the fermion self-energy read

$$\begin{aligned} \Sigma_\sigma^{\text{F}}(t, t') &= F_{\bar{\sigma}}^*(t, t') G_{\sigma\bar{\sigma}}^{\text{F}}(t, t') - \frac{1}{4} \rho_{\bar{\sigma}}^*(t, t') G_{\sigma\bar{\sigma}}^{\rho}(t, t'), \\ \Sigma_\sigma^{\rho}(t, t') &= \rho_{\bar{\sigma}}^*(t, t') G_{\sigma\bar{\sigma}}^{\text{F}}(t, t') + F_{\bar{\sigma}}^*(t, t') G_{\sigma\bar{\sigma}}^{\rho}(t, t'), \end{aligned} \quad (4.65)$$

where we used the symmetries for the statistical and spectral function to bring the time arguments in all terms to the same order. With Eq. (4.60), we can read off the solution of the resummed bosonic propagator,  $G$ , in the particle-particle (t)-channel from Eq. (4.44)

$$\begin{aligned} G &= iU \begin{pmatrix} 0 & 1 \\ 1 & 0 \end{pmatrix} \delta - U^2 \begin{pmatrix} 0 & \Pi_{21} \\ \Pi_{12} & 0 \end{pmatrix} - iU^3 \begin{pmatrix} 0 & \Pi_{21} * \Pi_{21} \\ \Pi_{12} * \Pi_{12} & 0 \end{pmatrix} \\ &+ U^4 \begin{pmatrix} 0 & \Pi_{21} * \Pi_{21} * \Pi_{21} \\ \Pi_{12} * \Pi_{12} * \Pi_{12} & 0 \end{pmatrix} + \dots \end{aligned} \quad (4.66)$$

If we put the first term in Eq. (4.63), we get exactly the mean-field contribution. Thus, we define the resummed bosonic propagator without the mean-field contribution as  $\bar{G} = G - iU\sigma_1\delta$ . This reads, in Feynman diagrams,

$$\text{wavy red line} = \left\{ \begin{array}{l} \text{diagram 1} + \text{diagram 2} + \mathcal{O}(U^4) \\ \text{diagram 3} + \text{diagram 4} + \mathcal{O}(U^4) \end{array} \right. \quad (4.67)$$

which is an infinite sum of bubbles with opposite spins pointing in the same direction. The two cases correspond to the two off-diagonal elements of the full bosonic propagator,  $G$ , which can be determined by the recursive equation

$$G_{\sigma\bar{\sigma}}(t, t') = iU(\Pi_{\bar{\sigma}\sigma} * G_{\sigma\bar{\sigma}})(t, t') - U^2 \Pi_{\bar{\sigma}\sigma}(t, t'). \quad (4.68)$$

We split it, with the help of Eq. (4.41), into its statistical and spectral parts in App. B.2 to calculate the effective coupling.

### 4.3.4 Particle-Hole (u)-Channel Resummation

We continue with the last channel resummation and derive the equations of motion for the one-point function of the auxiliary bosonic fields,

$$\frac{\delta\Gamma}{\delta\bar{\chi}_1} = \frac{\delta\Gamma}{\delta\bar{\chi}_2} = 0. \quad (4.69)$$

As in the particle-particle (t)-channel, the expectation value vanishes and therefore the mean-field contributions come from the resummed propagator. The 2PI part of the effective action,  $\Gamma_2$ , reads for the lowest possible 2PI diagram from the interaction term in Eq. (4.35),

$$\Gamma_{2,u}[G, D] = \frac{i}{2} \sum_{\sigma} \int_{\mathcal{C}} du du' D_{\sigma}(u, u') D_{\bar{\sigma}}(u', u) G_{\sigma\bar{\sigma}}(u, u') \quad (4.70)$$

and in terms of Feynman diagrams,

$$\Gamma_{2,u}[G, D] = \text{Diagram 1} + \text{Diagram 2}. \quad (4.71)$$

The structure looks very similar to the particle-particle (t)-channel but with opposite directions of the fermions. Hence, the self-energy of the auxiliary bosonic field has also only off-diagonal entries and reads

$$\begin{aligned} \Pi_{\sigma\bar{\sigma}}(t, t') &= -D_{\sigma}(t, t') D_{\bar{\sigma}}(t', t) = \Pi_{\bar{\sigma}\sigma}(t', t), \\ \Pi_{\sigma\sigma}(t, t') &= 0, \end{aligned} \quad (4.72)$$

diagrammatically,

$$\begin{aligned} \Pi_{\uparrow\downarrow}(t, t') &= \text{Diagram 3} = \Pi_{\downarrow\uparrow}(t', t), \\ \Pi_{\downarrow\uparrow}(t, t') &= \text{Diagram 4} = \Pi_{\uparrow\downarrow}(t', t) \end{aligned} \quad (4.73)$$

and split into its statistical and spectral components,

$$\begin{aligned} -\Pi_{\sigma\bar{\sigma}}^F(t, t') &= F_{\sigma}(t, t') F_{\bar{\sigma}}^*(t, t') - \frac{1}{4} \rho_{\sigma}(t, t') \rho_{\bar{\sigma}}^*(t, t'), \\ -\Pi_{\sigma\bar{\sigma}}^{\rho}(t, t') &= \rho_{\sigma}(t, t') F_{\bar{\sigma}}^*(t, t') + F_{\sigma}(t, t') \rho_{\bar{\sigma}}^*(t, t'). \end{aligned} \quad (4.74)$$

We take the derivative of Eq. (4.70) with respect to the full fermion propagator,  $D$ , to calculate the fermionic self-energy and obtain

$$\Sigma_{\sigma}(t, t') = \frac{1}{2} D_{\bar{\sigma}}(t, t') \left( G_{\sigma\bar{\sigma}}(t', t) + G_{\bar{\sigma}\sigma}(t, t') \right) = D_{\bar{\sigma}}(t, t') G_{\sigma\bar{\sigma}}(t', t), \quad (4.75)$$

where we used the symmetry relation  $G_{\sigma\bar{\sigma}}(t', t) = G_{\bar{\sigma}\sigma}(t, t')$ , which is a direct result of the symmetry of the self-energy in Eq. (4.72). The diagrammatic representation is

$$\Sigma_{\uparrow}(t, t') = \text{diagram with red wavy line and green arc}, \quad \Sigma_{\downarrow}(t, t') = \text{diagram with red wavy line and blue arc} \quad (4.76)$$

and split into its statistical and spectral components,

$$\begin{aligned} \Sigma_{\sigma}^{\text{F}}(t, t') &= F_{\bar{\sigma}}(t, t')G_{\bar{\sigma}\sigma}^{\text{F}}(t, t') - \frac{1}{4}\rho_{\bar{\sigma}}(t, t')G_{\bar{\sigma}\sigma}^{\rho}(t, t'), \\ \Sigma_{\sigma}^{\rho}(t, t') &= \rho_{\bar{\sigma}}(t, t')G_{\bar{\sigma}\sigma}^{\text{F}}(t, t') + F_{\bar{\sigma}}(t, t')G_{\bar{\sigma}\sigma}^{\rho}(t, t'). \end{aligned} \quad (4.77)$$

From Eq. (4.44), it follows that the solution for the resummed bosonic propagator in the particle-hole (u)-channel, with the help of Eq. (4.72), is

$$\begin{aligned} G &= iU \begin{pmatrix} 0 & 1 \\ 1 & 0 \end{pmatrix} \delta - U^2 \begin{pmatrix} 0 & \Pi_{21} \\ \Pi_{12} & 0 \end{pmatrix} - iU^3 \begin{pmatrix} 0 & \Pi_{21} * \Pi_{21} \\ \Pi_{12} * \Pi_{12} & 0 \end{pmatrix} \\ &+ U^4 \begin{pmatrix} 0 & \Pi_{21} * \Pi_{21} * \Pi_{21} \\ \Pi_{12} * \Pi_{12} * \Pi_{12} & 0 \end{pmatrix} + \dots \end{aligned} \quad (4.78)$$

and the diagrammatic representation for the off-diagonal elements is

$$\text{red wavy line} = \left\{ \begin{array}{l} \text{diagram 1} + \text{diagram 2} + \mathcal{O}(U^4) \\ \text{diagram 3} + \text{diagram 4} + \mathcal{O}(U^4) \end{array} \right. \quad (4.79)$$

The off-diagonal elements obey the recursive equation

$$G_{\sigma\bar{\sigma}}(t, t') = iU(\Pi_{\bar{\sigma}\sigma} * G_{\sigma\bar{\sigma}})(t, t') - U^2\Pi_{\bar{\sigma}\sigma}(t, t'), \quad (4.80)$$

which we split, with Eq. (4.41), into its statistical and spectral components in App. B.3 to calculate the effective coupling.

### 4.3.5 stu-Channel Resummation

Above, we discussed three different resummation channels according to the spins and direction of the fermionic propagators in the loops of the Feynman diagrams. All of these are directly derived from the underlying theory and therefore contribute to the physics. However, some diagrams can be more important depending on the physical situation. From this point of view, it is natural to define a new channel where all the three different channels are taken into consideration at the same time. However,

we have to be careful when doing this because diagrams in one channel can also be in one of the others. Thus, we define

$$\begin{aligned} \Gamma_{2,\text{stu}}[D, G] = & \Gamma_{2,\text{s}}[D, G] + \Gamma_{2,\text{t}}[D, G] \\ & + \Gamma_{2,\text{u}}[D, G] - \Gamma_{2,\cap}[D, G] , \end{aligned} \quad (4.81)$$

where  $\Gamma_{2,\cap}$  denotes

$$\begin{aligned} \Gamma_{2,\cap} = & \Gamma_{2,\text{s}} \cap \Gamma_{2,\text{t}} + \Gamma_{2,\text{s}} \cap \Gamma_{2,\text{u}} \\ & + \Gamma_{2,\text{t}} \cap \Gamma_{2,\text{u}} - \Gamma_{2,\text{s}} \cap \Gamma_{2,\text{t}} \cap \Gamma_{2,\text{u}} \end{aligned} \quad (4.82)$$

which prevents over-counting of the diagrams. Inserting the leading diagram of Eqs. (4.55), (4.67), and (4.79) into Eqs. (4.47), (4.59), and (4.71), we can see that the second order diagram

$$\Gamma_2^{\text{2nd}}[D] = \text{Diagram} \quad (4.83)$$


is already included in all channels and hence it must be subtracted twice from the sum of all channels. Therefore the corresponding non-local self-energy, which enters the dynamic equations for this channel, is given by

$$\begin{aligned} \Sigma_\sigma^{\text{stu}}(t, t') = & \Sigma_\sigma^{\text{s}}(t, t') + \Sigma_\sigma^{\text{t}}(t, t') \\ & + \Sigma_\sigma^{\text{u}}(t, t') - 2\Sigma_\sigma^{\text{2nd}}(t, t') . \end{aligned} \quad (4.84)$$

The local self-energy contribution arising from the double-bubble diagram is treated separately.

## 4.4 Implementing the Leads in the 2PI Formalism

At the beginning of this chapter, we focused on different non-perturbative truncations of the 2PI effective action for the isolated quantum dot with a repulsive on-site interaction. In this section, we explain how we implement the coupling of the leads to the quantum dot into the 2PI formalism. Initially, we assume that there are no correlations between the leads and the quantum dot and therefore, the density matrix of the entire system is given by the tensor product

$$\rho(t_0) = \rho_{\text{D}} \otimes \rho_{\text{L}} . \quad (4.85)$$

Furthermore, we assume that the leads are in thermal equilibrium, hence the density matrix of the leads is described by a grand canonical ensemble,  $\rho_{\text{L}} = \exp(-\beta(H - \mu N))$ , with the inverse temperature<sup>7</sup>  $\beta = T^{-1}$ , chemical potential  $\mu$ , and occupation number  $N$ . Since the leads are an infinite system in comparison to the quantum

<sup>7</sup>The inverse temperature is  $\beta = (k_{\text{B}}T)^{-1}$  with the Boltzmann constant  $k_{\text{B}}$ . However, we set  $k_{\text{B}} = 1$ .

dot, tunnelling processes to and off the quantum dot do not drive the leads out of equilibrium. In Sec. 2.5, we explained, with the inclusion of a thermal density matrix, that we need to extend the close time path by a finite strip along the imaginary time axis and therefore, in this section  $\mathcal{C}$  denotes the Konstantiov-Perel' time path [172].

In the SIAM, electrons form non-interacting metallic leads such that the model is quadratic in the lead electron operators and we can integrate them out exactly, which is why we do not have to make any further approximations in this procedure. In the following, we neglect the quantum dot part of the SIAM Hamiltonian in Eq. (3.7) and focus on the lead in Eq. (3.9) and tunnelling part of the action in Eq. (3.10) to write down the path integral representation of the partition function,

$$Z[d, d^\dagger] = \int \mathcal{D}[c, c^\dagger] \exp \left[ i \int_{\mathcal{C}} dt \sum_{k p \sigma} \left( c_{k p \sigma}^\dagger (i\partial_t - \epsilon_{kp}) c_{k p \sigma} + \tau c_{k p \sigma}^\dagger d_\sigma + \tau^* d_\sigma^\dagger c_{k p \sigma} \right) \right]. \quad (4.86)$$

We shift the lead electron fields that we integrate over,

$$c'_{k p \sigma} = c_{k p \sigma} + \tau (i\partial_t - \epsilon_{kp})^{-1} d_\sigma, \quad c'^{\dagger}_{k p \sigma} = c^\dagger_{k p \sigma} + \tau^* (i\partial_t - \epsilon_{kp})^{-1} d_\sigma^\dagger \quad (4.87)$$

to complete the square and arrive at a Gaussian integral in the new primed fields,

$$Z[d, d^\dagger] = \int \mathcal{D}[c', c'^\dagger] \exp \left[ i \int_{\mathcal{C}} dt \sum_{k p \sigma} \left( c'^{\dagger}_{k p \sigma} (i\partial_t - \epsilon_{kp}) c'_{k p \sigma} - |\tau|^2 d_\sigma^\dagger (i\partial_t - \epsilon_{kp})^{-1} d_\sigma \right) \right]. \quad (4.88)$$

We perform the Gaussian integral over the shifted lead electron fields

$$Z[d, d^\dagger] \sim \exp \left[ -i |\tau|^2 \int_{\mathcal{C}} dt \sum_{k p \sigma} d_\sigma^\dagger (i\partial_t - \epsilon_{kp})^{-1} d_\sigma \right], \quad (4.89)$$

where the expression between the dot electron fields is the free propagator of a lead electron. This is the inverse of the differential operator of the free theory

$$(i\partial_t - \epsilon_{kp}(t)) A_{k p \sigma}(t, t') = \delta_{\mathcal{C}}(t, t'), \quad (4.90)$$

where  $\epsilon_{kp}(t) = \epsilon_{kp}$  is on the Keldysh contour and  $\epsilon_{kp}(t) = \epsilon_{kp} - \mu$  on the additional imaginary strip.  $A_{k p \sigma}$  denotes the free propagator of the lead electrons that is also defined by the time ordered product of an annihilation and creation operator, *c.f.* Eq. (2.1),

$$iA_{k p \sigma}(t, t') = \langle \mathcal{T}_{\mathcal{C}} c_{k p \sigma}(t) c_{k p \sigma}^\dagger(t') \rangle. \quad (4.91)$$

The time evolution of the creation and annihilation operator is given by a phase factor with the energy eigenvalue

$$c_{k p \sigma}(t) = c_{k p \sigma} e^{-i\epsilon_{kp} t}, \quad c_{k p \sigma}^\dagger(t) = c_{k p \sigma}^\dagger e^{i\epsilon_{kp} t}. \quad (4.92)$$

We insert this into Eq. (4.91) and yield

$$\mathcal{T} c_{k p \sigma}(t) c_{k p \sigma}^\dagger(t') = (1 - c_{k p \sigma}^\dagger c_{k p \sigma}) e^{-i\epsilon_{kp}(t-t')} \theta(t-t') - c_{k p \sigma}^\dagger c_{k p \sigma} e^{-i\epsilon_{kp}(t-t')} \theta(t'-t). \quad (4.93)$$

The occupation number operator can be expressed with the Fermi–Dirac distribution function, known from quantum statistics, as

$$\langle N_{kp\sigma} \rangle = \langle c_{kp\sigma}^\dagger c_{kp\sigma} \rangle = \frac{1}{e^{\beta(\epsilon_{kp} - \mu_p)} + 1} = f(\epsilon_{kp} - \mu_p). \quad (4.94)$$

With this and the relation  $2\theta(t) = 1 + \text{sgn}(t)$ , we get the statistical and spectral components of the free lead electron propagators

$$\begin{aligned} A_{kp\sigma}^F(t, t') &= -i \left( \frac{1}{2} - f(\epsilon_{kp} - \mu_p) \right) e^{-i\epsilon_{kp}(t-t')}, \\ A_{kp\sigma}^\rho(t, t') &= e^{-i\epsilon_{kp}(t-t')}. \end{aligned} \quad (4.95)$$

Only the statistical component of the free lead electron propagator contains information about the thermodynamic properties, like the temperature and chemical potential, of the leads. In addition to this, due to the Fermi–Dirac distribution function, it has knowledge about the occupation probability of a state. Both components depend only on the difference of the times, which indicates thermal equilibrium.

If we add the quantum dot part of the SIAM Hamiltonian to the partition function in Eq. (4.89) and follow the same steps as in Ch. 2, we obtain the equation of motion for the quantum dot electron propagator,

$$\left[ D_0^{-1} + i|\tau|^2 A \right] * D = \Sigma * D + \delta. \quad (4.96)$$

We can interpret the leads term as a contribution to the free inverse propagator of the dot electrons or, alternatively, we can bring the term to the right-hand side and interpret this as a contribution to the self-energy. We continue with the latter point of view and get a contribution to each electron’s self-energy,

$$\begin{aligned} \Sigma_L^{F(1)}(t, t') &= -|\tau|^2 \left( \frac{1}{2} - f(\epsilon - \mu) \right) e^{-i\epsilon(t-t')}, \\ \Sigma_L^\rho(t, t') &= -i|\tau|^2 e^{-i\epsilon(t-t')}. \end{aligned} \quad (4.97)$$

We get the entire contribution from all electrons in the lead by integrating over the density of states of the lead,  $\rho_L$ . Thus, we replace the sum over  $k$ , which indicates the energy of one electron, with an energy integral in the limits of the bandwidth,  $D$ . We obtain, for either the statistical or spectral components of the self-energy,

$$\Sigma_L(t, t') = \int_{-D}^D d\epsilon \rho_L(\epsilon) \Sigma_L^{(1)}. \quad (4.98)$$

Throughout this thesis, we use the wide flat band limit, where we assume a constant density of states. The one lead contribution to the spectral component of the self-energy is given by

$$\Sigma_p^\rho(t, t') = -i \lim_{D \rightarrow \infty} \int_{-D}^D d\epsilon \rho_L |\tau|^2 e^{-i\epsilon(t-t')} = -i\Gamma \delta(t - t'), \quad (4.99)$$

where we have used the definition of the hybridisation  $\Gamma = 2\pi|\tau|^2\rho_L$ . For the statistical part of the self-energy, we obtain

$$\Sigma_p^F(t, t') = - \lim_{D \rightarrow \infty} \int_{-D}^D d\epsilon, \rho_L |\tau|^2 \left( \frac{1}{2} - f(\epsilon - \mu) \right) e^{-i\epsilon(t-t')}. \quad (4.100)$$

In general, it is not possible to perform this integral analytically. However, in the case of zero temperature and  $D > |\mu|$ , it follows that

$$\begin{aligned} \Sigma_p^F(t, t') &= - \lim_{D \rightarrow \infty} \frac{\Gamma}{4\pi} \int_{-D}^D d\epsilon \operatorname{sgn}(\epsilon - \mu_p) e^{-i\epsilon(t-t')} \\ &= \lim_{D \rightarrow \infty} \frac{i\Gamma}{2\pi} \frac{e^{-i\mu_p(t-t')} - \cos D(t-t')}{t-t'} \\ &= \frac{i\Gamma}{2\pi} \mathcal{P} \frac{e^{-i\mu_p(t-t')}}{t-t'}, \end{aligned} \quad (4.101)$$

where  $\mathcal{P}$  denotes the principal value.

### Exact Mean-Field Solutions

The dynamic equations for the statistical propagator and spectral function are only coupled through the effective mass term that includes the occupation number in both equations. At late times, the occupation number is supposed to be stationary and then it is a constant and both equations decouple. Therefore, we can solve the dynamic equation for the spectral function independent of the statistical propagator. Only the statistical component of the self-energy arising from the leads causes problems and such a term does not exist in the dynamic equation for the spectral function.

We apply a Wigner transform to the time coordinates which changes the times  $t, t'$  to the relative  $s = t - t'$  and absolute time  $T = (t + t')/2$  because at later times when the system reaches equilibrium, the statistical propagator,  $F$ , and the spectral function,  $\rho$ , only depend on the difference of the times. Hence, we have

$$\partial_s \rho_\sigma(s) = \left( -iM_\sigma - \Gamma \operatorname{sgn}(s) \right) \rho_\sigma(s). \quad (4.102)$$

For this equation, we need an initial value to obtain a solution. From the fermionic anti-commutator, we get an initial value  $\rho_\sigma(0) = i$ . With this, we get

$$\rho_\sigma(s) = i \exp \left( -iM_\sigma s - \Gamma |s| \right) \quad (4.103)$$

and the spectral function in Fourier space reads

$$\rho_\sigma(\omega) = i \int_{-\infty}^{\infty} ds \exp \left( i(\omega - M_\sigma)s - \Gamma |s| \right) = \frac{2i\Gamma}{(\omega - M_\sigma)^2 + \Gamma^2}, \quad (4.104)$$

with the expected normalisation

$$\int_{-\infty}^{\infty} \frac{d\omega}{2\pi} \frac{2i\Gamma}{(\omega - M_\sigma)^2 + \Gamma^2} = i. \quad (4.105)$$

In comparison to the mean-field solution of the isolated quantum dot in Eq. (4.16), the state in the spectral function has a finite width of  $2\Gamma$  due to the coupling of the leads. This leads to a finite lifetime of this state because electrons can tunnel off the quantum dot. The effective mass term,  $M_\sigma$ , appears as a free parameter in the spectral function. In the next step, we want to derive a constraint equation for the occupation number, which also sets the effective mass. For that, we transform the dynamic equation for the spectral propagator,  $F$ , to the new variable,  $T$ , which is directed along the diagonal in the real time plane. However, we encounter a problem because of the memory integrals arising from the leads that contain the statistical part of the self-energy, due to the cumbersome term in Eq. (4.101). Since we are only interested in the stationary value, we can push the times in the limits of the integral to infinity. Then this integral is a convolution in the real time domain, which translates to a normal product in Fourier space. Therefore, we have to apply the inverse Fourier transform to the product of  $\Sigma_{\text{lead}}^{\text{F}}(\omega) = -\Gamma/2 \text{sgn}(\omega)$  and the spectral function given in Eq. (4.104). We do this only for equal times because we are interested in the occupation number. This simplification makes the inverse Fourier transform analytically solvable and we get

$$\int_{-\infty}^{\infty} du \Sigma_{\text{lead}}^{\text{F}}(t, u) \rho_\sigma(u, t) = -\frac{i\Gamma}{\pi} \arctan\left(\frac{E_0 + Un_{\bar{\sigma}}}{\Gamma}\right). \quad (4.106)$$

The dynamical equation for the statistical propagator along the time diagonal reads

$$i\partial_T F_\sigma(T) = -i\Gamma F_\sigma(T) + \frac{i\Gamma}{\pi} \arctan\left(\frac{E_0 + Un_{\bar{\sigma}}}{\Gamma}\right), \quad (4.107)$$

where the first term on the right-hand side comes from the spectral part of the lead contribution to the self-energy. In any case, this equation is only valid for large times  $T \rightarrow \infty$  because of the second term on the right-hand side. Therefore, we can only extract the stationary occupation number from that and not the whole time evolution. At large times, when the system reaches equilibrium, the statistical propagator,  $F$ , and consequently the occupation number, is a constant. Thus, the left-hand side of Eq. (4.107) is zero. With these considerations and  $F_\sigma(T) = 1/2 - n_\sigma(T)$ , we can recover the known occupation number at mean-field, *c.f.* Ref. [20], from the Kadanoff–Baym equations of motion derived from the 2PI effective action

$$n_\sigma = \frac{1}{2} - \frac{1}{\pi} \arctan\left(\frac{E_0 + Un_{\bar{\sigma}}}{\Gamma}\right). \quad (4.108)$$

We do not consider a magnetic field, which means that the occupation number for up and down spins are the same,  $n_\sigma = n_{\bar{\sigma}}$ . This equation is not solvable analytically but it can be solved numerically or graphically. In the particle-hole symmetric quantum dot,  $E_0 = -U/2$ , the solution of the equation is  $n = 0.5$ . This is easy to verify because, in this case, the argument of the inverse tangent function is zero and therefore this term vanishes.



## 4.5 Electrical Current and Conductance

Now that we have discussed how to implement the leads in the 2PI formalism, we can introduce the electrical current through a quantum dot. Electrical current is transport of charges and therefore the product of the elementary charge and the change of the occupation number. The contribution of one lead to the current through the quantum dot is

$$I_p(t) = -e\dot{N}_p(t), \quad N_p(t) = \sum_{k\sigma} \langle c_{pk\sigma}^\dagger(t) c_{pk\sigma}(t) \rangle \quad (4.109)$$

and the total net current is given by the difference of both contributions,

$$I = \frac{I_L - I_R}{2}. \quad (4.110)$$

We can compute the derivative with respect to the time of one operator with the help of the Heisenberg equation<sup>8</sup>. Thus, we have to calculate the commutator of the occupation number operator in Eq. (4.109) with the full Hamiltonian. The quantum dot and the lead part of the Hamiltonian commutes with the occupation number operator,

$$[H_D, N_p] = [H_L, N_p] = 0, \quad (4.111)$$

because the first term does not contain a creation or annihilation operator of a lead electron and the second term contains only the occupation number operator of lead electrons. Therefore, we need to calculate the commutator of the part of the Hamiltonian that describes the tunnelling between quantum dot and leads and the occupation number operator

$$\begin{aligned} I_p &= -\frac{e}{\hbar} i [H_{T,p}, N_p] = -\frac{e}{\hbar} i \sum_{k\sigma} \left[ - (t_p c_{pk\sigma}^\dagger d_\sigma + t_p^* d_\sigma^\dagger c_{pk\sigma}), c_{pk\sigma}^\dagger c_{pk\sigma} \right] \\ &= -i \frac{e}{\hbar} \sum_{k\sigma} (t_p c_{pk\sigma}^\dagger d_\sigma - t_p^* d_\sigma^\dagger c_{pk\sigma}). \end{aligned} \quad (4.112)$$

The index  $p$  attached to the Hamilton operator indicates that only one lead is taken into account because the commutator of the two operators is non-vanishing if the creation and annihilation operators of the lead electrons operate on the same lead. The total electrical current through the quantum dot is given by the expression,

$$I(t) = -\frac{i\pi e}{h} \sum_{pk\sigma} p \left( t_p \langle c_{pk\sigma}^\dagger d_\sigma \rangle - t_p^* \langle d_\sigma^\dagger c_{pk\sigma} \rangle \right) (t). \quad (4.113)$$

We want to include this term in our path integral formalism. It is convenient to calculate the electrical current just by taking the derivative of a source, in analogy to the correlation functions,

$$I(t_m) = -i \frac{\partial}{\partial \eta} \ln Z[\eta] \Big|_{\eta=0} = -i \frac{1}{Z} \frac{\partial Z[\eta]}{\partial \eta} \Big|_{\eta=0} = \left\langle \frac{\partial S_\eta}{\partial \eta} \Big|_{\eta=0} \right\rangle. \quad (4.114)$$

<sup>8</sup>In the Heisenberg picture, an operator  $\mathcal{O}$  obeys the Heisenberg equation  $d\mathcal{O}/dt = i/\hbar[H, \mathcal{O}] + \partial\mathcal{O}/\partial t$ .

Therefore, we need to introduce an additional term to the action in the path integral, which reads

$$S_\eta(t_m) = -\frac{i\pi e\eta}{h} \sum_{pk\sigma} p \left( t_p c_{pk\sigma}^\dagger d_\sigma - t_p^* d_\sigma^\dagger c_{pk\sigma} \right) (t_m). \quad (4.115)$$

At this point, we can also integrate out the leads degree of freedom with this additional term in the action, as we did in the previous section. We can just change the tunnelling parameter slightly,

$$\tilde{\tau} = \tau \left( 1 + \frac{i\pi e\eta}{h} p \delta(t_m - t) \right), \quad (4.116)$$

to get exactly the same form as before in Eq. (4.88), and arrive at

$$\begin{aligned} iS_{\text{lead}} = -i|\tau|^2 \sum_{pk\sigma} \int_{\mathcal{C}} dt \int_{\mathcal{C}} dt' d_\sigma^\dagger(t) & \left( A_{pk\sigma}(t, t') + \frac{i\pi e\eta}{h} p A_{pk\sigma}(t, t') \right. \\ & \left. \times \left[ \delta(t' - t_m) - \delta(t - t_m) \right] \right) d_\sigma(t'), \end{aligned} \quad (4.117)$$

where we have dropped the term that is proportional to  $\eta^2$  because it yields a term with  $\eta$  after we take the derivative with respect to this source. We have to set this source to zero and therefore it vanishes.

The goal is to derive a formula for the electrical current through the quantum dot from this effective action. To achieve this, we have to take the derivative with respect to the source,  $\eta$ , and obtain

$$\begin{aligned} I_p(t_m) = -\frac{i\pi e}{h} |\tau|^2 \sum_{pk\sigma} p \left( \int_{\mathcal{C}} dt' D_\sigma(t', t_m) A_{pk\sigma}(t_m, t') \right. \\ \left. + \int_{\mathcal{C}} dt D_\sigma(t_m, t) A_{pk\sigma}(t, t_m) \right). \end{aligned} \quad (4.118)$$

The full quantum dot propagator comes from taking the expectation value. For the next step, we split the product of the full quantum dot and the free lead electron propagators into the spectral and statistical components. The latter will vanish due to the integration along the Schwinger–Keldysh contour because one of the terms has no sign function and the other has two but with the same time arguments. For this reason, we only calculate the spectral part of it,

$$\left( D_\sigma(t', t_m) A_{pk\sigma}(t_m, t') \right)^\rho = \rho_\sigma(t', t_m) A_{pk\sigma}^{\text{F}}(t_m, t') - F_\sigma(t', t_m) A_{pk\sigma}^\rho(t_m, t'). \quad (4.119)$$

We put this into Eq. (4.118), bring the arguments of the propagators for all terms to the same order and obtain the expression for the current as a function of time:

$$\begin{aligned} I(t_m) = -\frac{\pi e}{h} |\tau|^2 \sum_{pk\sigma} \int_0^{t_m} dt p \left( A_{pk\sigma}^{\text{F}}(t_m, t) \rho_\sigma(t, t_m) - A_{pk\sigma}^\rho(t_m, t) F_\sigma(t, t_m) \right. \\ \left. + A_{pk\sigma}^{\text{F}*}(t_m, t) \rho_\sigma^*(t, t_m) - A_{pk\sigma}^{\rho*}(t_m, t) F_\sigma^*(t, t_m) \right). \end{aligned} \quad (4.120)$$

The terms including the statistical propagator,  $F$ , drop out because the spectral part of  $A$  does not contain any information about the thermodynamic properties of the leads and thereby  $A_L^{\rho} = A_R^{\rho}$ . We use  $|\tau|^2 = \Gamma/(2\pi)$  and insert the expression for  $A$  into Eq.(4.120). Finally, we obtain

$$\begin{aligned} I(t_m) &= -\frac{e\Gamma}{h} \Re \sum_{\sigma} \int_0^{t_m} dt \left( A_L^F(t_m, t) - A_R^F(t_m, t) \right) \rho_{\sigma}(t, t_m) \\ &= \frac{e\Gamma}{h} \Im \sum_{\sigma} \int_{-D}^D d\epsilon \int_0^{t_m} dt \left( f(\epsilon - \mu_L) - f(\epsilon - \mu_R) \right) e^{-i\epsilon(t_m-t)} \rho_{\sigma}(t, t_m). \end{aligned} \quad (4.121)$$

Since the real part of the exponential is symmetric, the imaginary part is anti-symmetric and vice versa for the symmetries of real and imaginary parts of the spectral function. Consequently, the imaginary part of the product of both functions is symmetric. For this reason, we can also extend the time integral to negative times and get an additional factor of 1/2. Furthermore, we push the time to infinity and get, for the stationary current,

$$\begin{aligned} I &= \frac{e\Gamma}{2h} \Im \sum_{\sigma} \int_{-D}^D d\epsilon \int_{-\infty}^{\infty} ds \left( f(\epsilon - \mu_L) - f(\epsilon - \mu_R) \right) e^{-i\epsilon s} \rho_{\sigma}(s, T) \\ &= \frac{e\Gamma}{2h} \Im \sum_{\sigma} \int_{-D}^D d\epsilon \left( f(\epsilon - \mu_L) - f(\epsilon - \mu_R) \right) \rho_{\sigma}(\epsilon, T). \end{aligned} \quad (4.122)$$

This equation is also called the Meir-Wingreen formula [198], which is a Landauer formula<sup>9</sup> [199] for the current through an interacting electron region. In the first line, we applied a Wigner transform and in the step to the second line, we performed the integral along the relative time coordinate, which leads to a Fourier transform of the spectral function.

Once we have the electrical current, we can introduce the linear and differential electrical conductance:

$$G_{\text{lin}}(t) = \frac{I(t)}{V}, \quad G_{\text{dif}}(t) = \frac{dI(t)}{dV}. \quad (4.123)$$

### Exact Mean-Field Solution

At mean-field order, it is possible to calculate exact results for the stationary current voltage characteristics at zero temperature. We can just take the solution we found in the previous subsection for the spectral function in Eq. (4.104). In that solution, we find the effective mass term that is an unknown parameter to be determined before we can insert the solution into Eq. (4.122) to calculate the stationary current.

We need a new constraint equation for the occupation number because Eq. (4.108) is only valid for zero chemical potential of the leads. In the derivation of this equation, we replace the statistical self-energy component of the leads with  $\Sigma_{p,\text{lead}}^F(\omega) =$

<sup>9</sup>The Landauer formula combines the transmission amplitude,  $T$ , of a one-level non-interacting scatterer in a conductor with the conductance,  $G$ , for low bias voltages,  $G = 2e^2/h|T|^2$ .

$-\Gamma/2 \operatorname{sgn}(\omega - \mu_p)$  and obtain [29]

$$n_\sigma = \frac{1}{2} - \frac{1}{2\pi} \arctan\left(\frac{E_0 + Un_{\bar{\sigma}} - V/2}{\Gamma}\right) - \frac{1}{2\pi} \arctan\left(\frac{E_0 + Un_{\bar{\sigma}} + V/2}{\Gamma}\right). \quad (4.124)$$

However, we always assume that the quantum dot is in the particle-hole symmetric case,  $E_0 = -U/2$ , the chemical potentials are adjusted symmetrically,  $\mu_L = -\mu_R = -\mu/2$ , around zero energy, and we do not apply a magnetic field to the leads. In this case, Eq. (4.124) is also easy to solve with an educated guess of  $n_\sigma = n_{\bar{\sigma}} = 0.5$ . Then the single electron energy,  $E_0$ , and the mean-field contribution,  $Un$ , cancel each other. From the anti-symmetric property of the inverse tangent function, it follows that the two inverse tangent functions cancel each other and we are left with one half on the left- and right-hand sides. In this special case, the effective mass term is always zero and the occupation number for up and down spins is a half.

With that, it follows for the stationary electrical current,

$$\lim_{t_m \rightarrow \infty} I(t_m) = \frac{e\Gamma}{2h} \sum_\sigma \int_{-D}^D d\epsilon \left( f(\epsilon - \mu_L) - f(\epsilon - \mu_R) \right) \frac{2\Gamma}{(\epsilon - M_\sigma)^2 + \Gamma^2}, \quad (4.125)$$

and at zero temperature and finite bias voltage we get

$$I = 2 \frac{e\Gamma}{h} \int_{-\mu/2}^{\mu/2} d\epsilon \frac{2\Gamma}{\epsilon^2 + \Gamma^2} = \frac{4e\Gamma}{h} \left[ \arctan\left(\frac{\mu}{2\Gamma}\right) \right]. \quad (4.126)$$

For the maximum current, we take the limit of an infinite chemical potential gradient:

$$I = 2\pi \frac{e\Gamma}{h}. \quad (4.127)$$

From Eq. (4.126), we immediately obtain the differential conductance

$$\frac{dI}{dV} = G_0 \frac{4\Gamma^2}{\mu^2 + (2\Gamma)^2}, \quad (4.128)$$

where we introduced the conductance quantum<sup>10</sup>  $G_0 = 2e^2/h$  [200].

## 4.6 Summary

In this chapter, we discussed the Kadanoff–Baym equations of motion and different approximations of the two-particle irreducible (2PI) effective action for the single impurity Anderson model (SIAM) introduced in the previous chapter. Due to the low temperatures and energies, we do not have to consider any relativistic effects and so the SIAM has a two-to-two scattering interaction vertex that couples up to down spins. Although the Kadanoff–Baym equations of motion are exact, we have

<sup>10</sup>The conductance quantum in SI units is  $G_0 = 7.7480917346(25) \cdot 10^{-5}$  S.

to make an approximation for the self-energy because of the tremendous complexity in order to obtain self-contained expressions for the dynamic equations in terms of the statistical propagator,  $F$ , and the spectral function,  $\rho$ , so that we can solve them numerically. We reviewed two non-equilibrium approximation schemes of the 2PI part of the effective action.

First, we made a loop expansion of the 2PI part of the effective action up to the third order explicitly. In the lowest order mean-field approximation, we found that the dynamic equations for the statistical propagator and the spectral function do not have any non-Markovian memory integrals. This changes when we go to a higher expansion of the 2PI effective action.

Second, we carried out a resummation of spin bubbles to all orders, which is possible as long as we sum up a certain class of Feynman diagram. According to the spin structure of each bubble, we categorised the resummation in three channels: the direct (s)-channel, which consists of alternating spin bubbles; the particle-particle (t)-channel and particle-hole (u)-channel, where all bubbles with opposite spins are propagating in the opposite or same direction. In addition, we also took all channels into account simultaneously in a so-called stu-channel. Here, we had to pay attention to avoid multiple counting of Feynman diagrams. The Hubbard-Stratonovich transformation provides an elegant way of achieving this. We wrote down the leading-order resummation in terms of resummed auxiliary propagators.

Afterwards, we showed how we implemented the non-interacting metallic leads into the 2PI formalism. The path integral for the SIAM is Gaussian in the lead electron fields, which provides the opportunity to integrate them out exactly. This results in an additional contribution to the self-energy.

At the end, we introduced the electrical conductance and current through the quantum dot and derived an expression for the transient, as well as stationary, properties. Both quantities are important for characterising the electrical charge transport properties of the quantum dot in a non-equilibrium situation, in the case of a finite bias voltage, where both chemical potentials of the leads are different.



## Chapter 5

# Time Evolution of an Anderson Quantum Dot

In the previous chapter, we introduced different non-perturbative approximations from simple loop expansions to the resummation of an infinite number of Feynman diagrams for the two-particle irreducible (2PI) effective action of the single impurity Anderson model (SIAM). The Kadanoff–Baym equations of motion are exact equations for the two-point functions but are not solvable without any truncations to the 2PI part of the effective action or to the self-energy of the quantum dot electrons. Therefore, finding significant approximations that on the one hand side, include as much physics as possible and on the other hand, limit the Kadanoff–Baym equations of motion to a solvable set of equations is a major step towards reliable results. In addition to this, we discussed how we implemented the leads into the 2PI formalism and derived the necessary equations for the physical quantities describing transport through the quantum dot, such as equations for the electrical current and conductance.

The SIAM consists of two elements, the leads and the quantum dot. First, we prepare the system such that there is no coupling between the leads and the quantum dot,  $\tau = 0$ , and the two elements are separate systems. The leads are in thermal equilibrium and thus the leads' density matrix is described by a grand canonical ensemble. The density matrix of the quantum dot is determined by the initial occupation. We will assume an empty quantum dot and the equal time anti-commutation relation specifies the two-point function. At the beginning of the time evolution, we perform a quench in the coupling,  $\tau$ , and the interaction strength,  $U$ , and with that we drive the quantum dot out of equilibrium. However, throughout the whole time evolution, we assume the leads stay in thermal equilibrium because the leads are a much larger system than the quantum dot and the occurring tunnelling processes cannot alter this.

We begin this chapter with the discussion of the initial conditions and the numerical implementation. The first part of our numerical results is dedicated to the quantum dot without a chemical gradient. We start with the transient and stationary occupation of the quantum dot. However, the main focus is on the spectral function in the particle-hole symmetric scenario, where the Kondo effect plays a major role. For the second part of our numerical results, we switch on a bias voltage which also

provides a non-equilibrium condition for the quantum dot. This applied voltage leads to a charge transport through the quantum dot. We study the transient, as well as the stationary, electrical current and conductance with respect to their dependence on the applied voltage, temperature and magnetic field. The main goal of this thesis is to have a better understanding of the transient dynamics of this quantum system in and out of equilibrium.

This work is based on Ref. [145] where similar investigations were undertaken with the 2PI effective action in the direct (s)-channel resummation. In this thesis, we extend the investigation to all other non-perturbative resummations discussed in Ch. 4 and with our research for the SIAM, go into much more detail.

## 5.1 Numerical Implementation

In this section, we discuss how we numerically solve the equations we derived in the previous chapter to obtain the results we present in the ongoing sections. We start the discussion with the initial conditions, the leads, go on to the algorithm we use for solving the Kadanoff–Baym equations of motion and end with comments on the units we use in this chapter. For more details on the used numerical methods we refer to Appendix A.

### 5.1.1 Initial Conditions

In Ch. 2, we stated that non-equilibrium physics can be formulated as a collection of initial value problems, which can also be seen from the integro-differential Kadanoff–Baym equations of motion. These type of equations need defined initial values in order to calculate the time evolution just like every other ordinary differential equation. From the definition of the statistical function,  $F$ , in Eq. (2.5), it follows that it is linearly proportional to the occupation number of the system at equal times, see Eq. (2.8), and therefore it is determined by the initial occupation. The initial value for the spectral function,  $\rho$ , is given by the equal-time anti-commutator relation for fermions. Hence, the initial values read

$$\rho_\sigma(t_0, t_0) = i, \quad (5.1)$$

$$F_\sigma(t_0, t_0) = \frac{1}{2} - n_\sigma(t_0) \quad (5.2)$$

and thereby, according to Eq. (2.6), the propagator or two-point function for the quantum dot electrons,

$$D_\sigma(t_0, t_0) = \langle d_\sigma(t_0) d_\sigma^\dagger(t_0) \rangle, \quad (5.3)$$



is completely defined. All other two-point correlation functions are:

$$\langle d_\sigma(t_0)d_\lambda^\dagger(t_0) \rangle = 0 \quad \text{for } \sigma \neq \lambda \quad (5.4)$$

$$\langle d_\sigma^\dagger(t_0)d_\lambda^\dagger(t_0) \rangle = 0 \quad (5.5)$$

$$\langle d_\sigma(t_0)d_\lambda(t_0) \rangle = 0 \quad (5.6)$$

and higher order correlation functions are set to zero. This is how the Gaussian initial conditions introduced in Subsec. 2.2 enter the Kadanoff–Baym equations of motion. We want to stress that during the time evolution higher correlation functions can and will, for non-linearly coupled systems, build up.

### 5.1.2 Leads

The main advantage of the leads' contribution to the self-energies is that it only depends on the time difference, which means only  $\mathcal{N}$  values must be calculated for the spectral and statistical part of the self-energy and not  $\mathcal{N}^2$ . Hence, this saves memory and calculation power. Since the number of points,  $\mathcal{N}$ , for each time axis and the step size of the time discretisation,  $\Delta t$ , must be set in advance, the statistical component of the leads' self-energy contribution given in Eq. (4.100) can be calculated completely at the beginning, stored in an array and added to the dot self-energies when it is needed. For the spectral part of the self-energy, we use the limit of an infinite bandwidth and can treat this term similarly, as with the mean-field contribution.

In the case of zero temperature, another benefit comes into play because the integral can be performed analytically, as shown in Eq. (4.100), and thus saves further calculation effort. For non-vanishing temperatures, we use fifth order Gauß–Legendre quadrature in lieu of a Newton–Cotes rule to perform the integrals because it is usually more accurate and furthermore, the functions occurring in the integral are given analytically. The latter point is the reason why this integration method is not very applicable to the memory integrals on the right-hand side of the dynamic equations. Since the nodes are the roots of the Legendre polynomial, and therefore not equally distributed, this means that intermediate points are needed. In general, it is possible to interpolate these points but this procedure has an additional numerical error and extends the runtime dramatically.

### 5.1.3 Kadanoff–Baym Equations of Motion

In the past, the Kadanoff–Baym equations of motion were solved by splitting the differential part from the non-Markovian memory integrals, see Refs. [116, 126]. While the differential part was solved with the fourth-order Runge–Kutta algorithm, the memory integrals were calculated with a Newton–Cotes formula of second order. However, both results were added together linearly, which is why this procedure has an error of the same order as the standard Euler method. In Ref. [145], a modified

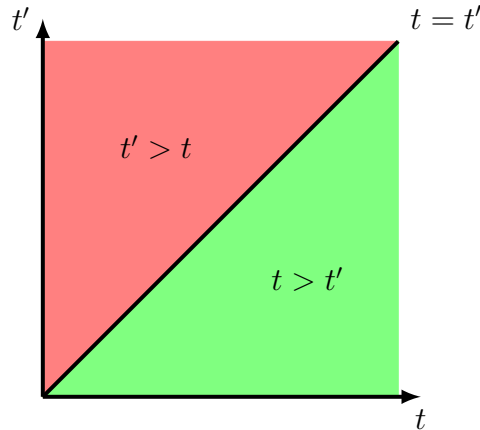


**Figure 5.1:** Illustration of the real-time plane, where we solve the Kadanoff–Baym equations of motion for the statistical propagator,  $F$ , and spectral function,  $\rho$ . In the green area, we solve the dynamic equations of motion, Eq. (4.1), numerically, and for the red area, we take advantage of the symmetry relations given in Eq. (4.3) to save computation time. The spectral function is fixed for equal times due to the anti-commutator relation for fermions. Since the quantum dot is coupled to external baths, the occupation number is not conserved and consequently the statistical propagator must also be solved numerically for equal times.

Euler method was used to solve the Kadanoff–Baym equations of motion. In this thesis we apply an algorithm to these equations where we treat both parts in the same way consistently.

One way to treat both parts equally is to use a single step algorithm, such as the Runge–Kutta method, which needs only the current time point to calculate the next one. This makes the algorithm very stable but at the same time it is also a drawback because midpoints are needed. This is the reason why it is complicated to implement the memory integrals using this algorithm. Another way is to apply a linear multistep algorithm. At first glance, it seems to be an elaborate solution because points from the past must be taken into consideration. However, due to the memory integrals, we have to save the entire past anyway.

For the linear multistep algorithms we have to distinguish between the explicit Adams–Bashforth methods where the current and past time points are needed and the implicit Adams–Moulton methods, where the next time point also appears on the right hand side. This makes the implicit method more stable but at every time step, we have to solve a linear set of equations. Due to this fact, we decided to combine both methods and use a predictor-corrector method. First, we apply an  $n$ -th order Adams–Bashforth to calculate the value at the new time step,  $t_{n+1}$ , and put this value into an  $(n + 1)$ -th<sup>1</sup> order Adams–Moulton method to increase the accuracy of this

<sup>1</sup>For the Adams–Bashforth and Adams–Moulton algorithms, we use the order counting convention given in App. A.

value (correction step). Our analysis showed that we could decrease the numerical errors if we execute the correction step twice. We could not find any better results if we increased the number of iterations for the correction step. This predictor-corrector algorithm and higher order Newton–Cotes integration clearly improves the results for the exponential decay of the spectral function, in the tail of the relative time, at the end of the time evolution.

At the beginning of the time evolution, when we only have our initial values, we start with the lowest possible order in the predictor step, which is the implicit, and in the corrector, the explicit Euler method. After every time step, we increase the order of the multistep algorithms until we reach the aforementioned orders after  $n$  time steps, and then calculate all the following values in the time evolution at this order in the methods.

We save computation time by using the symmetry relations for the statistical and spectral function shown in Eq. (4.3). With these symmetries, we only have to calculate the lower triangle in the real time plane. Starting from the initial values at  $(t_0, t_0)$  we perform the time step to get the values at  $(t_1, t_0)$  and with the symmetries also the values at  $(t_0, t_1)$ . For the spectral function, the values along the time diagonal, which are the equal times, are determined by the equal-time anti-commutator relations and no further calculations are needed. This changes for the statistical function because the occupation number that is related to the diagonal values can change; as long as the quantum dot is coupled to leads. So we apply our algorithm to the values at the point  $(t_1, t_0)$  to find the solution at  $(t_1, t_1)$ . We do this successively until we arrive at the end of our time evolution.

For the non-Markovian memory integrals, we do not make any truncations to the time we take into account. In every time step, we integrate over the full past and therefore we have to save all values for the statistical and spectral function, as well as the statistical and spectral part of the self-energy. We evaluate the memory integrals with the well-known closed Newton–Cotes algorithm up to seventh order.

### 5.1.4 Units

Throughout the whole thesis, we use  $\Gamma$ -units for all quantities, which means we write them in terms of the hybridisation,  $\Gamma = 2\pi\rho_L|\tau|^2$ , and set it to one,  $\Gamma = 1$ . There are quantities which are in  $\Gamma$ -units, such as: interaction strength  $U$ , gate voltage  $E_0$ , chemical potential  $\mu$ , bias voltage  $eV$ , magnetic field  $B$ , temperature  $T$ , electrical current  $I$ , and the Fourier space variable  $\omega$ . There are also quantities that are in inverse  $\Gamma$ -units, such as time  $t$ , and spectral function  $\rho$  in Fourier space. For example, if we write  $U = 4$  we mean  $U = 4\Gamma$ . In our numerics we set the physical constants of elementary charge, Planck constant and Boltzmann constant to one,  $e = h = k_B = 1$ .

We want to point out that in the literature different definitions of the hybridisation,  $\Gamma$ , are used. In the case of two leads,  $\Gamma$  is half the width of the Hubbard side peaks. The definition  $\Gamma = \Gamma_L + \Gamma_R$  is also common. Hence, the results in the literature are not always directly comparable.

## 5.2 Equilibrium Study of the Quantum Dot

In this section, we begin our investigation of the non-equilibrium time evolution of an Anderson quantum dot coupled to leads with equal chemical potentials,  $\mu_L = \mu_R$ . This is, in principle, the equilibrium case for the quantum dot. However, as we stated in Sec. 4.4, we consider the leads and the quantum dot as two separate systems, which we couple immediately at the beginning of the time evolution by a quench in the tunnelling parameter<sup>2</sup>,  $\tau$ , and interaction strengths,  $U$ . Initially, this quench drives the quantum dot out of equilibrium but during the time evolution the system evolves into a stationary state. While the stationary state was studied extensively in theory and experiment, the time evolution of the quantum dot was only tackled theoretically in the years. In this section, we focus on the time evolution of the occupation number, as well as the stationary occupation and the spectral function. In this section, the main focus is on the spectral function.

### 5.2.1 Occupation Number

We consider first the transient evolution of the electron population on the quantum dot after a sudden coupling to the leads, given a particular self-coupling,  $U$ , on the dot. Our first aim is to study the effect of the different resummation schemes introduced in Ch. 4. We choose an initially empty dot,  $n_\uparrow(0) = n_\downarrow(0) = 0$ .

In both investigations of the transient as well as the stationary occupation of the quantum dot we let the system evolve numerically with a time-step size of  $\Delta t = 300^{-1}$  up to the total time  $t_{\max} = 6.67$  which correlates to 2000 time steps. We set the physical parameters of the quantum dot to a vanishing magnetic field,  $B$ , and couple it to zero temperature,  $T = 0$ , leads. For our investigation of the transient properties of the quantum dot we adjust the single electron energy level to the particle-hole symmetric point,  $E_0 = -U/2$ .

#### Transient Occupation

In Fig. 5.2, we compare the time dependence of the population of the dot as obtained with the full 2PI equations of motion for different resummation schemes applied for the 2PI part,  $\Gamma_2$ , of the effective action. The different panels show the results obtained with the dot self-energy in direct (s)-, particle-particle (t)-, particle-hole (u)-, and stu-channel resummations (from upper left to lower right panels). Since we set the initial occupation for both spins equally and do not apply a magnetic field to the quantum dot, the Kadanoff–Baym equations of motion are the same for spin up and down. Therefore, the occupation number for each spin evolves in the same way,  $n(t) = n_\uparrow(t) = n_\downarrow(t)$ , and we plot on the axis of ordinates the single electron occupation number. In each panel we compare the time evolution of the quantum dot population for different interaction strengths,  $U$ , from vanishing Coulomb interactions at  $U = 0$ , where an exact solution exists

---

<sup>2</sup>This is also called a hybridisation quench.

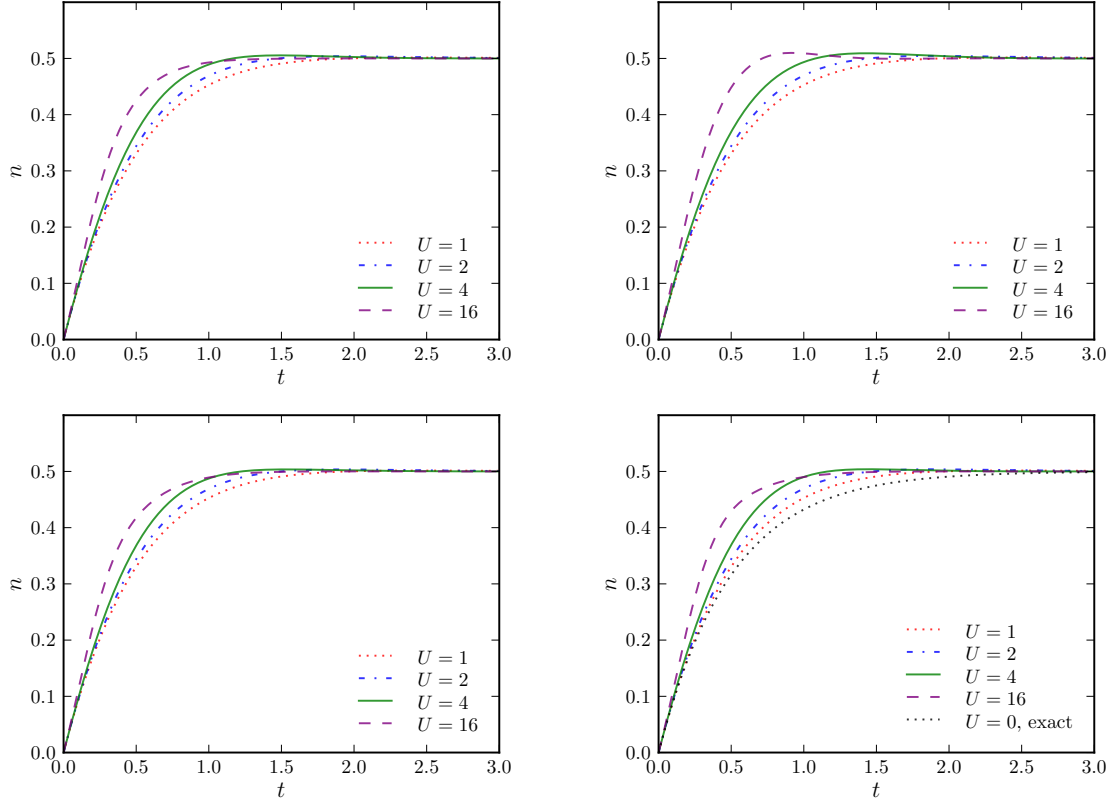


**Figure 5.2:** Comparison of the transient populations  $n(t) = n_{\uparrow}(t) = n_{\downarrow}(t)$  of the quantum dot at the particle-hole symmetric point starting from zero occupation, after a sudden coupling to the zero-temperature bath represented by the leads, for different interaction strengths between up- and down-spin electrons on the dot. The results are obtained in the direct (s)- (upper left), particle-particle (t)- (upper right), particle-hole (u)- (lower left), and stu-channel (lower right) resummation. The exact solution for  $U = 0$  is shown in Eq. (5.7), taken from Ref. [152].

$$n(t) = \frac{1}{2} \left( 1 - e^{-2\Gamma t} \right) \quad (5.7)$$

taken from Ref. [152], via small  $U = 1$ , all the way to large on-site couplings,  $U = 16$ .

We benchmarked our numerics with the exact solution in the non-interacting case and found a numerical error after the first time step of  $10^{-9}$ , which exponentially decreases during the time evolution to an error of  $10^{-15}$ , when the occupancy becomes stationary. For vanishing Coulomb interactions, we can read from Eq. (5.7) that the occupation number increases for  $t \ll 2\Gamma$  linearly in time and has a charge relaxation time of the order  $t_{\text{ch}} \sim 1/\Gamma$ .

In the presence of interactions on the quantum dot, we observe qualitatively similar results. At the beginning of the time evolution, the system is independent of

the interaction strengths because the interaction term, *cf.* Eq. (3.8), is proportional to the product of the occupancies of up and down spins. Therefore it takes about  $t \approx 0.1$  for large couplings and  $t \approx 0.4$  for small couplings for the effects of the interactions to set in. After this time, for all resummation schemes, we observe with increasing interaction strength a steeper initial slope in the occupation number and hence, the stationary state is reached earlier but at the same timescale as in the non-interacting case. The deviation of the interacting and non-interacting time evolution of the occupation number,  $\Delta n = n_U - n_0$ , with  $n_0$  given in Eq. (5.7), increases with increasing interaction strength. For  $U = 16$ , the maximum occurs around  $t = 0.45$  and is about  $\Delta n = 0.11$  and both values are slightly larger only in the particle-particle (t)-channel. However, if we compare the results for the interaction with the case without interaction but with a fixed gate voltage,  $E_0$ , the results change drastically because then both states are below the chemical potentials and the stationary occupation grows with increasing interaction strength.

In Ref. [152], a similar analysis was done with perturbation theory and Monte Carlo (MC) methods. The presented results are in good concordance with our results, especially with respect to the MC data. The main difference of the results is in the time range up to  $t \approx 0.15$ . Initially, it seems that the MC data for the occupation number starts with a higher exponent before it continues to increase linearly. In contrast to the wide flat band, in Ref. [152], a more realistic model with a soft cut-off for the leads is taken into consideration. In addition, the deviation of the interacting to the non-interacting case with a fixed bias voltage is close to our results.

While in the direct (s)-, particle-hole (u)-, and stu-channels, the stationary occupation is approached from below, we find that the particle-particle (t)-channel for large interaction strength,  $U = 16$ , oscillations lead firstly to an overshoot over the stationary occupation of  $n = 0.5$ , and later approaches that value from below.

For the study of the transient occupation of the quantum dot, we use the particle-hole symmetric setup, which means that the single and double occupation levels in the quantum dot are symmetrically assigned around the Fermi edges of the leads. Therefore we expect a stationary occupation of  $n = 0.5$ , which is obtained in all resummation schemes. For later times than are shown in Fig. 5.2, we find no change in the occupation up to the end of the time evolution at  $t_{\max} = 6.67$ . However, in the particle-particle (t)-channel resummation we observe numerical instabilities which come into play for even later times and lead to a divergence in the occupation number. For smaller time steps, we find the instability to appear at later times and for larger interaction strengths, at earlier times.

### Stationary Occupation

We discussed the transient and asymptotic occupation number for the direct (s)-, particle-particle (t)-, particle-hole (u)-, and stu-channels. We go on with the final occupation number at the end of the finite time evolution for these channels, not only in the particle-hole symmetric scenario, which is shown in Fig. 5.3. In each panel on the axis of ordinates we address the final single electron occupation number

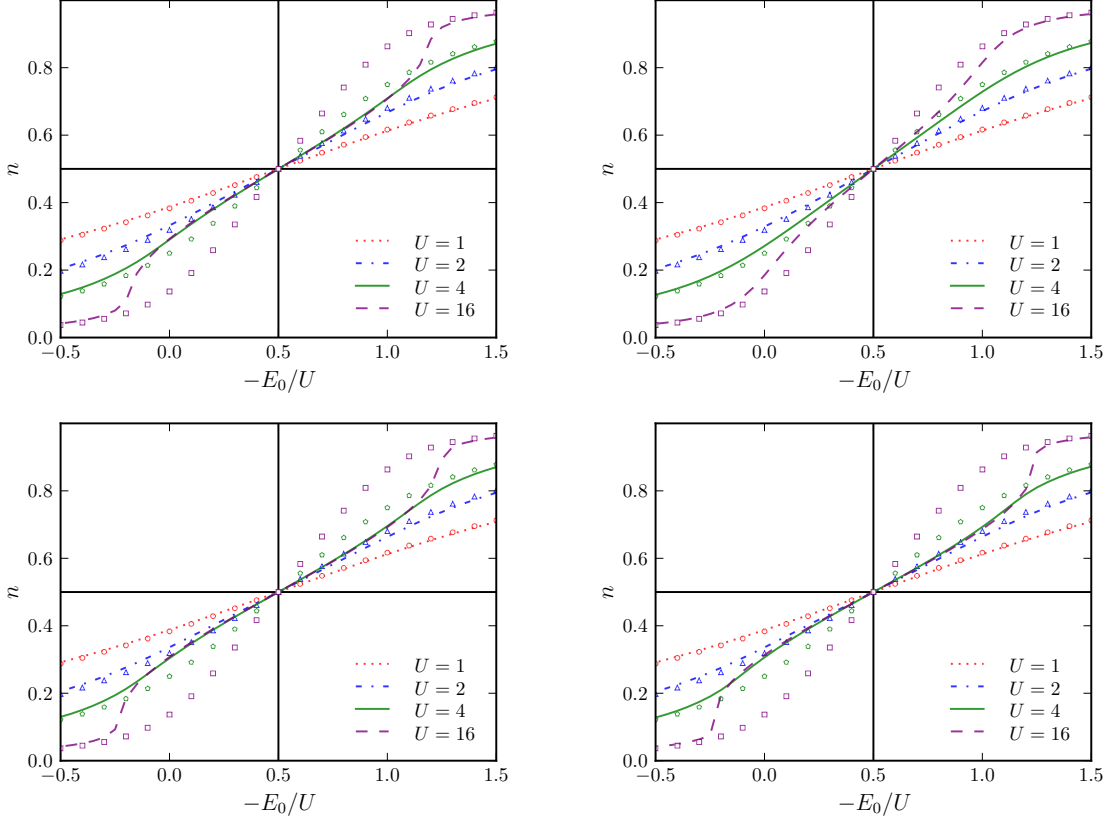


**Figure 5.3:** The final occupation number,  $n$ , after the time evolution, starting from zero occupation, as a function of the gate voltage,  $E_0$ , for several interaction strengths,  $U$ , obtained in the direct (s)- (upper left), particle-particle (t)- (upper right), particle-hole (u)- (lower left), and stu-channels (lower right). The two solid black lines in each panel mark the particle-hole symmetric setup and at this point, the results directly correspond to the asymptotic occupation number in Fig. 5.2. The different line styles indicate the numerical results obtained with the full 2PI equations of motion for different resummation schemes applied for the 2PI part,  $\Gamma_2$ , of the effective action and the points mark the mean-field solution given by Eq. (5.8).

$n$  and on the axis of abscissas the single electron energy level (gate voltage),  $E_0$ , normalised by the negative interaction strength,  $-U$ . This is a useful and convenient notation because the stationary population of the quantum dot is correlated with the axis of abscissa. We have to distinguish three regions: First, in the case of a gate voltage much smaller than the negative interaction strength  $E_0 \ll -U$ , or in our notation  $-E_0/U \gg 1$ , both energy levels lie below the Fermi edges and the quantum dot is fully occupied with two electrons, which means  $n = 1$  for the single electron. Second, the empty dot,  $n = 0$ , for gate voltages much larger than zero,  $E_0 \gg 0$ , and  $-E_0/U \ll 0$ , because both energy levels lie above the chemical potentials of

the leads. Third, in the region around the particle-hole symmetric point that is  $-U \gg E_0 \gg 0$  or  $0 \gg -E_0/U \gg 1$ , the quantum dot is singly-occupied,  $n = 1/2$ . The transition between the three regions is determined by the width of the energy levels, which means by the value of the transition matrix element,  $\tau$ .

In Fig. 5.3, the vertical solid line in each panel marks the particle-hole symmetric setup and the horizontal line the expected stationary occupation,  $n = 0.5$ . The values at this point result from the time evolution of the occupation number shown in Fig. 5.2. Besides the numerical results represented by the different line styles in each panel, we compare it to the mean-field solution for the stationary occupation number given by

$$n_\sigma = \frac{1}{2} - \frac{1}{\pi} \arctan\left(\frac{E_0 + Un_{\bar{\sigma}}}{\Gamma}\right), \quad (5.8)$$

which is represented by the symbols in the same colour for the same interaction strength. In the case of a vanishing magnetic field, Eq. (5.8) simplifies because both occurring occupation numbers are equal. Even in this simpler case, the equation is not solvable analytically and we need numerical techniques to find the intersection of the left- and right-hand side which was accomplished using MATHEMATICA.

For small interaction strengths, all results obtained from the non-perturbative resummation of the 2PI effective action agree very well with mean-field results. An explicit deviation, as expected, is visible for larger interaction strengths in the direct (s)-, particle-hole (u)-, and stu-channels. The particle-particle (t)-channel results still match pretty well. All non-perturbative resummations show the correct values for large negative values of the gate voltage, where the quantum dot is doubly occupied and on the other side for large gate voltages, where the quantum dot is empty. However, for large interaction strengths it is expected that around the particle-hole symmetric point a plateau should form. Our data shows that for interaction strengths starting from  $U = 4$ , the slope around the particle-hole symmetric point does not get steeper, but rather is even slightly more gradual for large interaction strengths.

## 5.2.2 Spectral Function

The width of the Kondo peak depends exponentially on the interaction strengths and therefore it is challenging to obtain the right results. Perturbative methods cannot yield this feature of the spectral function correctly. Surprisingly, a second order perturbation expansion in the interaction strength provides compared good results to Monte-Carlo methods, except for the Kondo temperature [30]. It is not yet known which Feynman diagrams are important and which cancel each other. The NRG yields the best results found in current literature [43, 44, 51, 52, 87, 88]. In Ref. [87], the stationary spectral function obtained from the time dependent NRG is compared to the results from the direct equilibrium calculation with NRG and a very good agreement is found. However, the time evolution into the stationary state is not shown. In Refs. [30, 45, 51, 52, 56, 67, 87, 88], the stationary equilibrium spectral functions are presented, which can render the main characteristics. In comparison to



this, other methods do not yield the main features correctly [61, 62, 65, 68, 69, 77, 147, 149].

In the non-equilibrium case, with different chemical potentials of the leads, the stationary spectral function is not yet completely known. The first investigation of this setup [201] proposed a splitting of the Kondo resonance in the spectral function, such that one peak is pinned to each chemical potential. With increasing bias voltage, the peaks should be damped and vanish for bias voltages much larger than the Kondo temperature. In contrast to that, there are other methods which do not yield these results. Instead, the bias voltage acts as an effective temperature that damps the Kondo peak until it vanishes [30]. The non-equilibrium spectral function for finite bias voltages is beyond the scope of this thesis.

### Interaction Strength Dependence for Long Time Evolution

We want to begin our discussion of the stationary spectral function with the dependence on the interaction strength of the on-site Coulomb repulsion,  $U$ . We let the quantum dot, which is adjusted to the particle-hole symmetric point, evolve in time, as stated in the beginning of this section, until the total time of  $t_{\max} = 20$  is reached with a time-step size of  $\Delta t = 800^{-1}$ . In Fig. 5.4, we present our results obtained from the numerics with the non-perturbative resummation approximation of the 2PI effective action in the direct (s)-, particle-particle (t)-, particle-hole (u)-, and stu-channel from upper-left to lower-right panel for small,  $U = 2$ , to intermediate interaction strengths,  $U = 10$ . During the time evolution we calculate the real and imaginary part of the spectral function in the whole real-time plane. In the figure, we show only the imaginary part of the spectral function at the end of the time evolution for positive relative times because the real part is zero and the imaginary part is symmetric according to the symmetry relation in Eq. (4.3).

In Ch. 3, we mentioned that the spectral functions for the symmetric SIAM without a bias voltage, at very low temperatures, show three peaks corresponding to the Hubbard side peaks because of the single and double occupation levels with a width of the order of  $\Gamma$  and a very narrow peak located at the Fermi edges with the width of the Kondo temperature,  $T_K$ . Thus, the spectral function in the time domain should be approximated by

$$\rho(t) = Ae^{-\Gamma|t|} \cos(U/2t) + Be^{-T_K/2|t|}. \quad (5.9)$$

The first term describes the side peaks with width<sup>3</sup>  $2\Gamma$ , located at the points  $\omega = \pm U/2$  and the second term, the Kondo peak. The real solution does not have to be exactly like Eq. (5.9) but it should be similar to it to render the expected characteristics. From Eq. (5.9), we can deduce that the first term approaches zero much faster than the second one because the width of the side peaks is much larger than the Kondo resonance,  $2\Gamma \gg T_K$ . While the short time behaviour is dominated

---

<sup>3</sup>We define the width as the full width at half maximum (FWHM) and use this definition throughout the whole thesis.

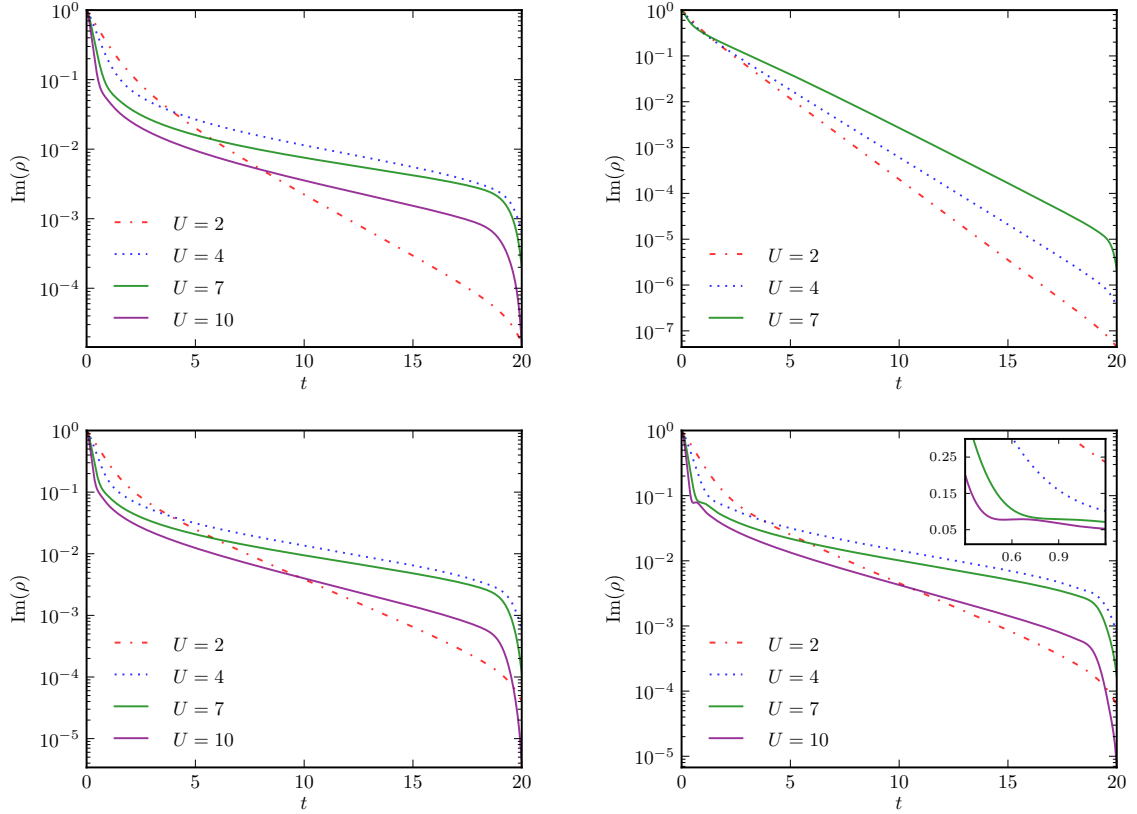


**Figure 5.4:** The imaginary part of the spectral function,  $\rho(t)$ , at the end of the time evolution obtained in the direct (s)- (upper left), particle-particle (t)- (upper right), particle-hole (u)- (lower left), and stu-channel (lower right) for different interaction strengths,  $U$ , with a time-step size of  $\Delta t = 800^{-1}$  in the particle-hole symmetric setup. The inset in the lower-right panel shows the transition region from large to small exponential decay. For larger interaction strengths, the oscillatory behaviour becomes more pronounced. This feature is important for the Hubbard side bands in Fourier space.

by the first term describing the coupling to leads, the late time characteristics come from the second term describing the Kondo correlations.

We compare these considerations to the results shown in Fig. 5.4, where we set the axis of ordinates to a log scale because then the exponential function becomes linear. For the smallest interaction strength,  $U = 2$ , two ranges with a larger negative slope for small relative times and a smaller one for later times are already visible in the direct (s)- but less pronounced, particle-hole (u)-, and stu-channel. This effect is only present in the particle-particle (t)-channel for larger interaction strengths but less distinct. The negative slope in this channel is larger than in the others and therefore, the spectral function at the final time is much smaller. In the other channels, the two ranges with different exponential decays become much steeper with increasing

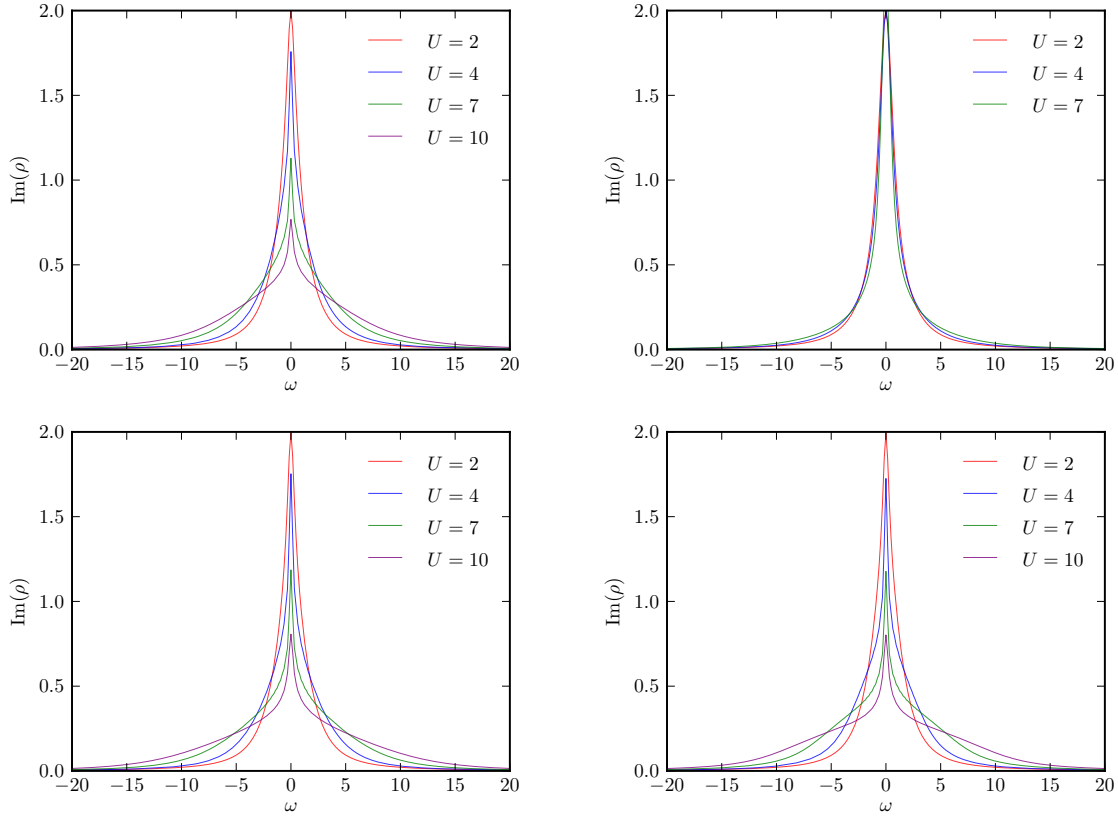


**Figure 5.5:** The discrete Fourier transform of the spectral function,  $\rho$ , shown in Fig. 5.4 obtained in the direct (s)- (upper left), particle-particle (t)- (upper right), particle-hole (u)- (lower left), and stu-channel (lower right) for different interaction strengths,  $U$ , in the particle-hole symmetric setup,  $E_0 = -U/2$ . The system was evolved to the time  $t_{\max} = 20$  with a time-step size of  $\Delta t = 800^{-1}$ .

interaction strengths. The initial drop-off depends on the interaction strength, which is also included in Eq. (5.9), in the argument of the cosine function. However, an oscillatory behaviour is clearly visible in the stu-channel and in the direct (s)- and particle-hole (u)-channel only a tiny ansatz. The strong bend that starts just before the final time is a finite-time effect we discuss later in more detail.

In Fig. 5.5, we show the corresponding spectral functions, to the same order as shown in Fig. 5.4, in Fourier space by using a discrete Fourier transform. It is clear that the spectral functions do not show the expected features, like the Hubbard side bands in the particle-particle (t)-channel, for example. Also, the peaks do not change much with increasing interaction strength. This is totally different in the other three channels. The first point to note is that the height of the peak is decreasing with increasing interaction strength, which means that the area under the spectral function in time is not conserved. This is not in accordance with the Friedel sum rule, *cf.* Fig. 5.7 and Fig. 5.8, which we discuss later. Second, besides the Kondo peak at

the origin, there are side peaks located at  $U = \pm U/2$ , which is best visible in the stu-channel. This effect sets in at interaction strengths of around  $U = 4$ . In the following discussion, we focus on the features of the Kondo peak, like width and height.

### Kondo Temperature

In this section, we focus on the main characteristic of the spectral function, the width of the Kondo resonance, which is determined by the Kondo temperature,  $T_K$ . The Kondo temperature is the energy scale at which the correlations between dot and lead electrons becomes important.

We do not read off the value for the width of the peak located at the origin for two reasons. First, the discretisation in the Fourier space is determined through the discrete Fourier transform as

$$\Delta\omega = \frac{\pi}{\Delta t \mathcal{N}}, \quad t_{\max} = \Delta t \mathcal{N} = 20. \quad (5.10)$$

This means decreasing the time-step size,  $\Delta t$ , makes the resolution in Fourier space worse if we do not simultaneously increase the number of time steps,  $\mathcal{N}$ . The resolution is given by the maximum time in the time evolution, which we chose to be  $t_{\max} = 20$ , thus in Fourier space the resolution is  $\Delta\omega \approx 0.157$ , which is much less accurate than in the time domain. Second, the amplitude of the peak is not the same for all time discretisations and interaction strengths. We discuss this fact in the following section.

Instead, we take advantage of our knowledge of the spectral function. We extract the Kondo temperature from an exponential fit,

$$\rho^{\text{fit}}(t) = k_1 e^{-k_2 |t|}, \quad (5.11)$$

to the data of our spectral functions at late times in the range  $t \in [12, 14]$ . We saw in Fig. 5.4 that we have to be careful for choosing the right range for this fit because at times which are too late the spectral function shows a sharp bend, which we will discuss later. For our consideration, the fit parameter,  $k_1$ , is of minor importance. The Kondo scale is related to the other fit parameter,  $T_K = 2k_2$ .

In Fig. 5.6, we address at the axis of ordinate, the Kondo temperature  $T_K$  and, at the abscissa, the interaction strength,  $U$ . We compare our results obtained in the direct (s)-, particle-particle (t)-, particle-hole (u)- and stu-channel from upper-left to lower-right panels for different time-step sizes,  $\Delta t$ , with the exact analytic solution [24–26] drawn as a black solid line given by Eq. (3.15). This solution is valid for  $U \gg \Gamma$  and therefore, we do not expect any accordance for small interaction strengths. Each curve from our numerical results is made of 19 data points; 13 data points from  $U = 0$  to  $U = 12$  in steps of  $\Delta U = 1$ , and an additional 6 data points at  $U \in \{2.5, 3.5, 4.5, 5.5, 14, 16\}$ .

Due to our method, how we extract the width cannot be distinguished for small interaction strengths between the decay, as a consequence of the coupling to the

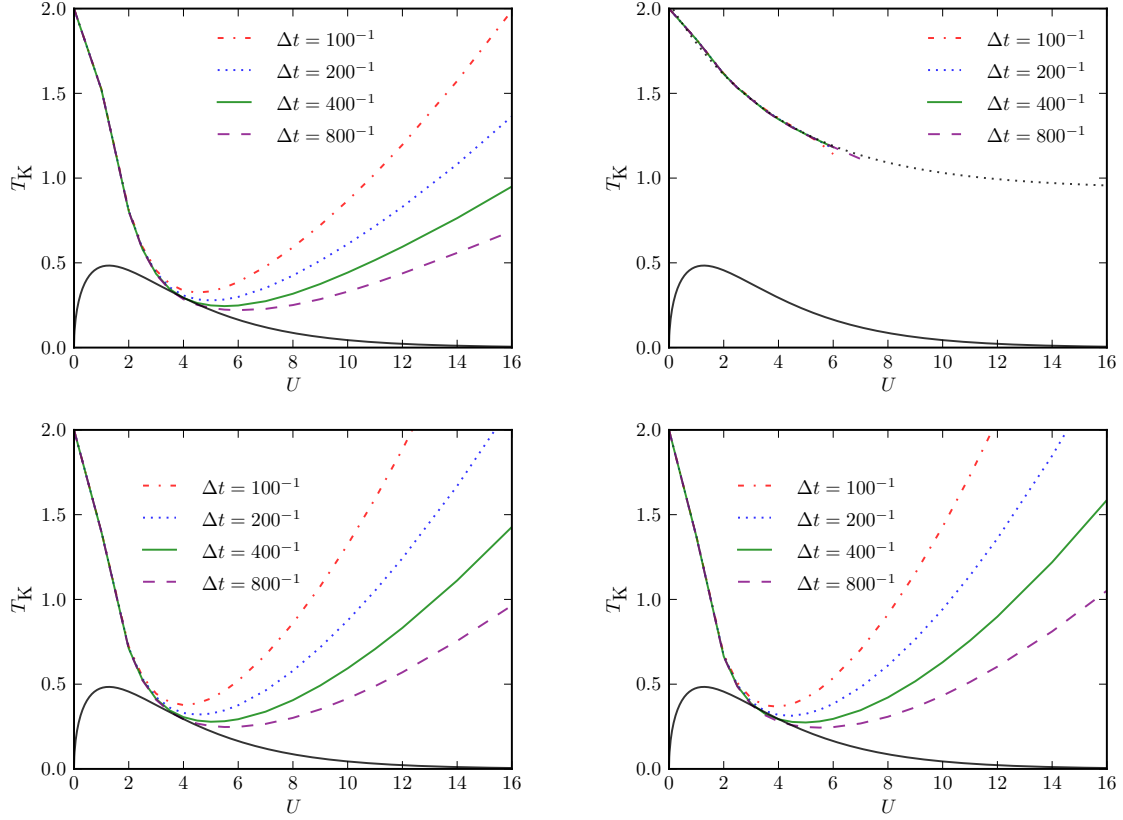


**Figure 5.6:** The Kondo temperature extracted from an exponential fit to the imaginary part of the spectral function in time (see Fig. 5.4) in the range of  $t \in [12, 14]$  as a function of the interaction strength,  $U$ , for different time-step sizes comparing with the exact analytic solution (black solid line) given in Eq. (3.15) obtained in the direct (s)- (upper left), particle-particle (t)- (upper right), particle-hole (u)- (lower left), and stu-channel (lower right).

leads and the Kondo effect. That is why the Kondo temperature seemingly rises to  $T_K = 2$  for the non-interacting case, *cf.* Eq. (4.103). For finite but small interactions, our data decreases and approaches  $U = 3$ , the exact analytic solution. Around that value, the Kondo effect starts to appear and we can speak of the Kondo temperature. In addition to this, the time-step size begins to play a role. With decreasing time-step size, our extracted Kondo temperature from the data gets closer to the analytic solution and the range where the accordance is very good increases up to  $U = 6$ . For stronger interactions, the numerical data grows whereas the exact analytic results fall off exponentially. The results in the particle hole (u)- and stu-channel are very close to each other and no significant deviation is visible. In the direct (s)-channel, the results for the width of the Kondo resonance is even better for large interaction strengths but not yet close the exact solution.

The situation for the particle-particle (t)-channel is completely different. Al-

though the extracted decay constant decreases with increasing interaction strength the data does not approach the expected Kondo temperature. In this channel, we cannot observe a Kondo effect. From this data we can also see the numerical instability that shows up for interaction strengths around  $U = 7$ . With decreasing time-step size this instability is observable at later times. We fit the following function,

$$T_{\text{K}}^{\text{fit}}(U) = \alpha e^{-\beta U} + \gamma, \quad (5.12)$$

to the data shown in the upper-right panel in Fig. 5.6 and get the best match for the parameters

$$\alpha = 1.100, \quad \beta = 0.243 \approx \pi/13, \quad \gamma = 0.934. \quad (5.13)$$

Interestingly, the data exhibit an exponential component but also a large constant offset. The behaviour of this resummation channel is not yet fully understood.

### Spectral Sum Rule

Another characteristic of the spectral function in Fourier space, besides the width we discussed before, is the height of the peak at the Fermi edge. Since we have already seen in Fig. 5.5 that the height of the peak is not the same for different interaction strengths,  $U$ , we will review the impact of the time-step size, as well as the total time of the non-equilibrium time evolution of the Anderson quantum dot. The Friedel sum rule [202] predicates that the occupation number of displaced electrons of a Fermi gas due to a charged impurity is related to the scattering phase shift. This was also applied to a system of interacting electrons in Ref. [203] and later to the Anderson model in Ref. [204]. The generalised Friedel sum rule gives a connection between the quantum dot occupation and its spectral function in Fourier space at the Fermi edge

$$\rho(0) \sim \sin^2 \left( \frac{\pi n}{2} \right), \quad (5.14)$$

taken from Ref. [150], with  $n = n_{\uparrow} + n_{\downarrow}$ , the mean total occupation number on the quantum dot. This is an exact result for zero temperature and in the particle-hole symmetric case where  $n_{\uparrow} = n_{\downarrow} = 1/2$ , this holds independent of the interaction strength,  $U$ . Obviously, the Friedel sum rule demands a constant height of the peak at the Fermi edge which contradicts the results we have shown before. This is why it needs some further investigation.

In Fig. 5.7, we show the results obtained from the non-perturbative resummation of the 2PI effective action in the direct (s)-, particle-particle (t)-, particle-hole (u)-, and stu-channel from the upper-left to lower-right panels for the value of the spectral function at zero energy as a function of the interaction strength,  $U$ , for different time-step sizes,  $\Delta t$ . For each graph, we evolved the quantum dot coupled to two leads to the time  $t_{\text{max}} = 20$  for interaction strengths from  $U = 0$  to  $U = 16$  in steps of  $\Delta U = 1$ . Although we have shown in Subsec. 5.2.1 that the numerics yield the correct quantum dot occupation in the particle-hole symmetric case, the spectral function at zero energy does not match the Friedel sum rule in Eq. (5.14) for all

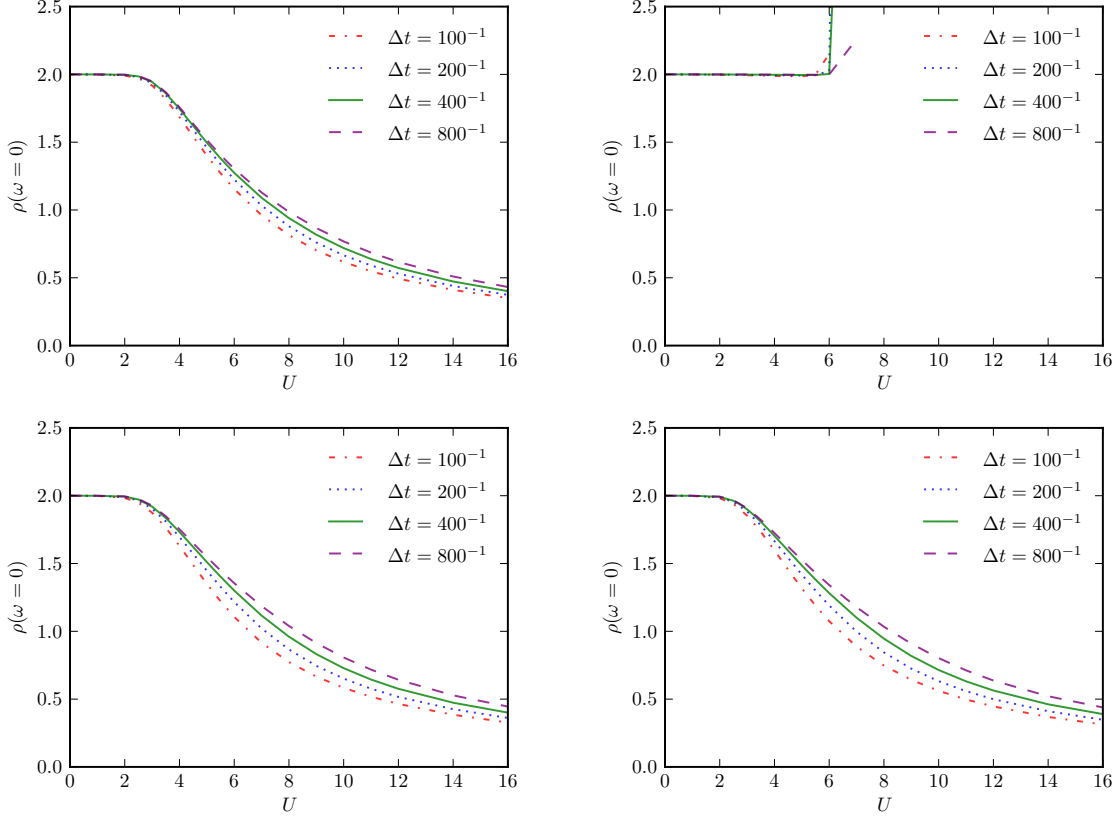


**Figure 5.7:** The value of the spectral function in Fourier space at  $\omega = 0$  as a function of the interaction strength  $U$  obtained in the direct (s)- (upper left), particle-particle (t)- (upper right), particle-hole (u)- (lower left), and stu-channel (lower right) for different time-step sizes and a total time evolution of  $t_{\max} = 20$ .

interaction strengths. For interaction strengths up to  $U = 3$ , all non-perturbative resummation channels are in perfect concordance with the expected value according to the Friedel sum rule. While the particle-particle (t)-channel also fulfils the Friedel sum rule up to  $U = 6$  until it struggles with the previously mentioned numerical instabilities, all other resummation channels fall off exponentially, and then go over into a power law decline, below  $1/2$  for interaction strengths around  $U = 16$ . When the decline sets in, the time-step size starts to play a role as in the analysis of the Kondo temperature but the effect is much smaller in comparison. The effect of the time-step size in the particle-hole (u)- and stu-channel is slightly larger than in the direct (s)-channel. This is consistent with the results for the Kondo temperature in Fig. 5.6 because the extracted Kondo temperatures in the direct (s)-channel are, for different time-step sizes, closer to each other than in the other two channels.

In Fig. 5.8, we show the influence of the total time of the non-equilibrium time evolution on the height of the spectral function at the Fermi edge for all non-perturbative resummation channels in the same order as in Fig. 5.7. We now fix

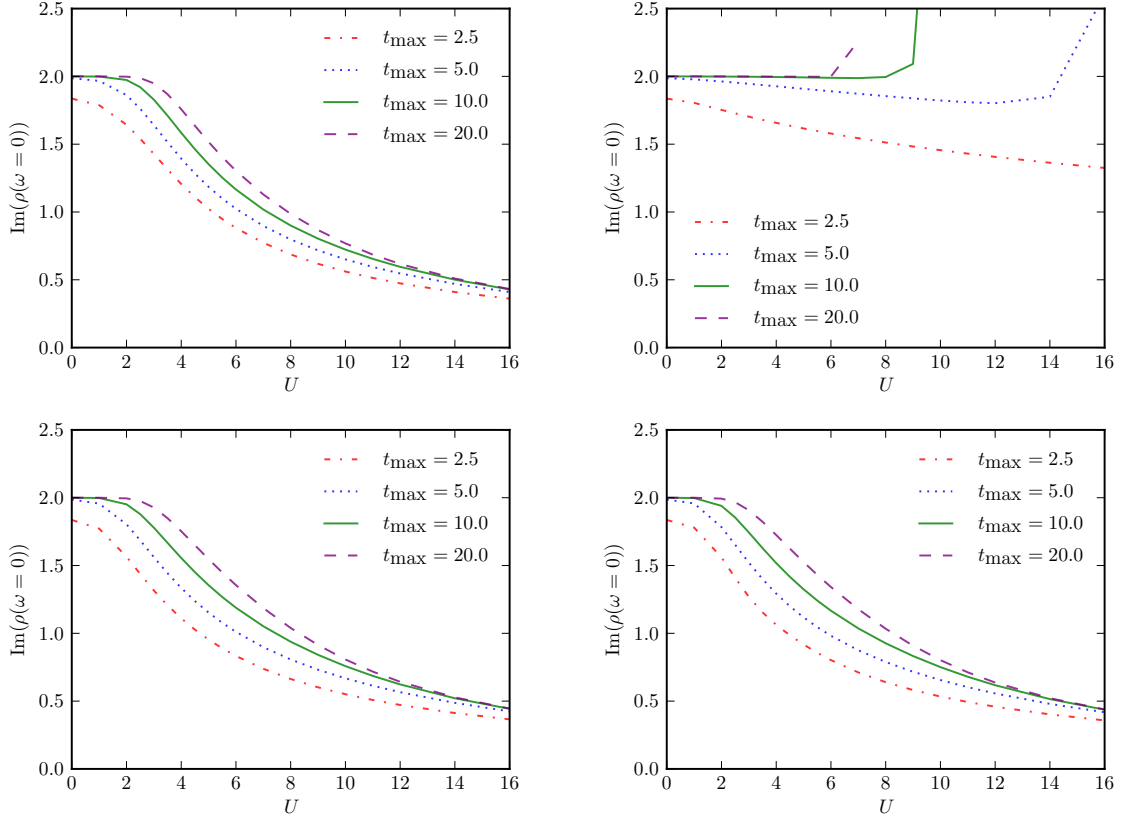


**Figure 5.8:** The value of the spectral function in Fourier space at  $\omega = 0$  as a function of the interaction strength,  $U$ , obtained in the direct (s)- (upper left), particle-particle (t)- (upper right), particle-hole (u)- (lower left), and stu-channel (lower right) for different total times,  $t_{\max}$ , and a time-step size of  $\Delta t = 800^{-1}$ .

the time-step size to  $\Delta t = 800^{-1}$  and vary the total time of the time evolution for all integer interaction strengths from  $U = 0$  to  $U = 16$ . In contrast to the dependence on the time-step size, the impact of the total time is biggest for small interactions and gets smaller for larger interaction strengths. Hence, the larger the total time, the bigger the range of interaction strengths where the Friedel sum rule is perfectly fulfilled. Unlike the width of the Kondo peak and with that the Kondo temperature is formed at times around  $t \approx 13$  for all probed interaction strengths up to  $U = 16$  the height of the peak is a real long time effect which takes much more time for larger interaction strengths.

### Time-Step Size Dependence

The dependence of the imaginary part of the stationary spectral function in time on the time-step size is shown in Fig. 5.9 obtained in the non-perturbative direct (s)-, particle-particle (t)-, particle-hole (u)-, and stu-channels, from upper left to



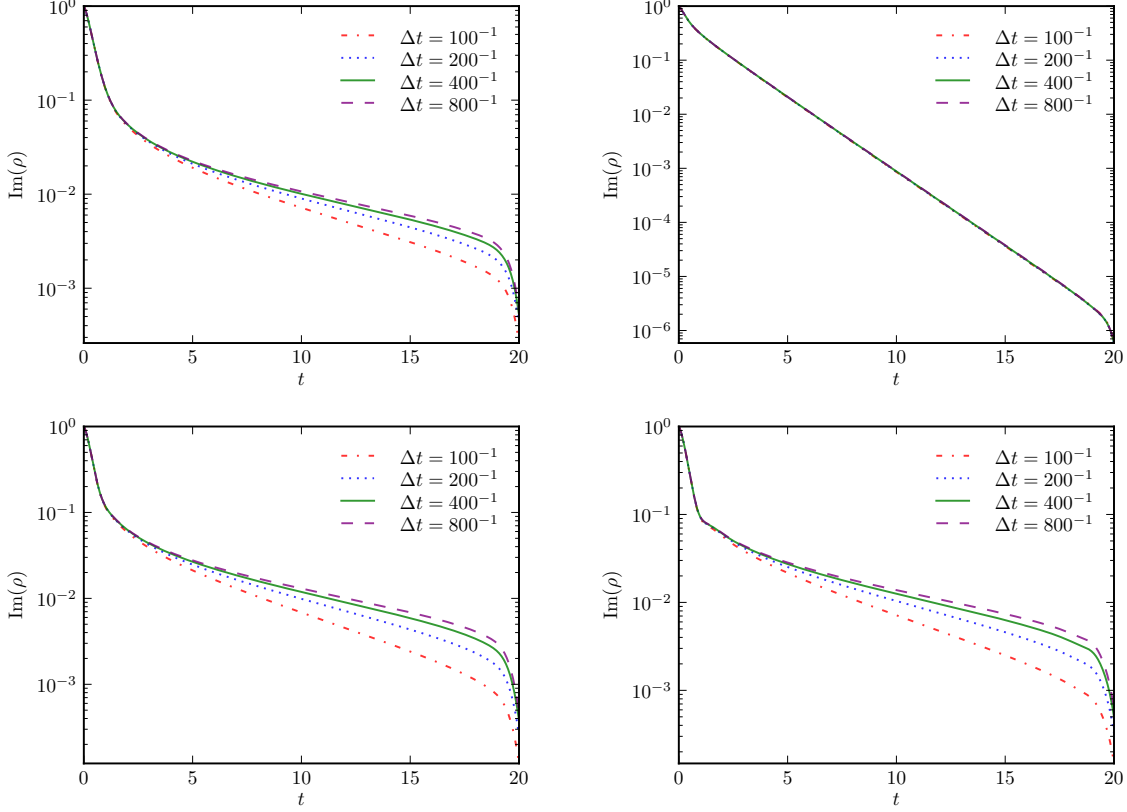


**Figure 5.9:** The imaginary part of the spectral function in time obtained in the direct (s)- (upper left), particle-particle (t)- (upper right), particle-hole (u)- (lower left), and stu-channel (lower right) with an interaction strength  $U = 5$  in the particle-hole symmetric setup at zero temperature and different time-step sizes.

lower right, in the particle-hole symmetric case,  $E_0 = -U/2$ . We evolved the system to the total time of  $t_{\max} = 20$  for time-step sizes between  $\Delta t = 100^{-1}$  and  $\Delta t = 800^{-1}$  for an interaction strength of  $U = 5$  at zero temperature. In contrast to the particle-particle (t)-channel, the effect of the time-step size plays a role in the non-perturbative resummation channels starting from relative times around  $t \approx 4$ . Therefore, it is hard numerically to achieve precise results for the tail in the spectral function and equivalently, the width of the Kondo peak. Moreover, the results for the exponential decay in the tail have not yet converged and will become smaller for even smaller time-step sizes, *cf.* Fig. 5.6. This also results in a larger area under the spectral function in time and therefore, the Kondo peak in the Fourier domain grows. In addition to this, the exponential decay in the particle-particle (t)-channel only changes a little, which is clearly different to the other channels. Only the results obtained in the stu-channel show a small plateau in the transition region between the two different exponential decays, leading to stronger pronounced side peaks in the Fourier domain.

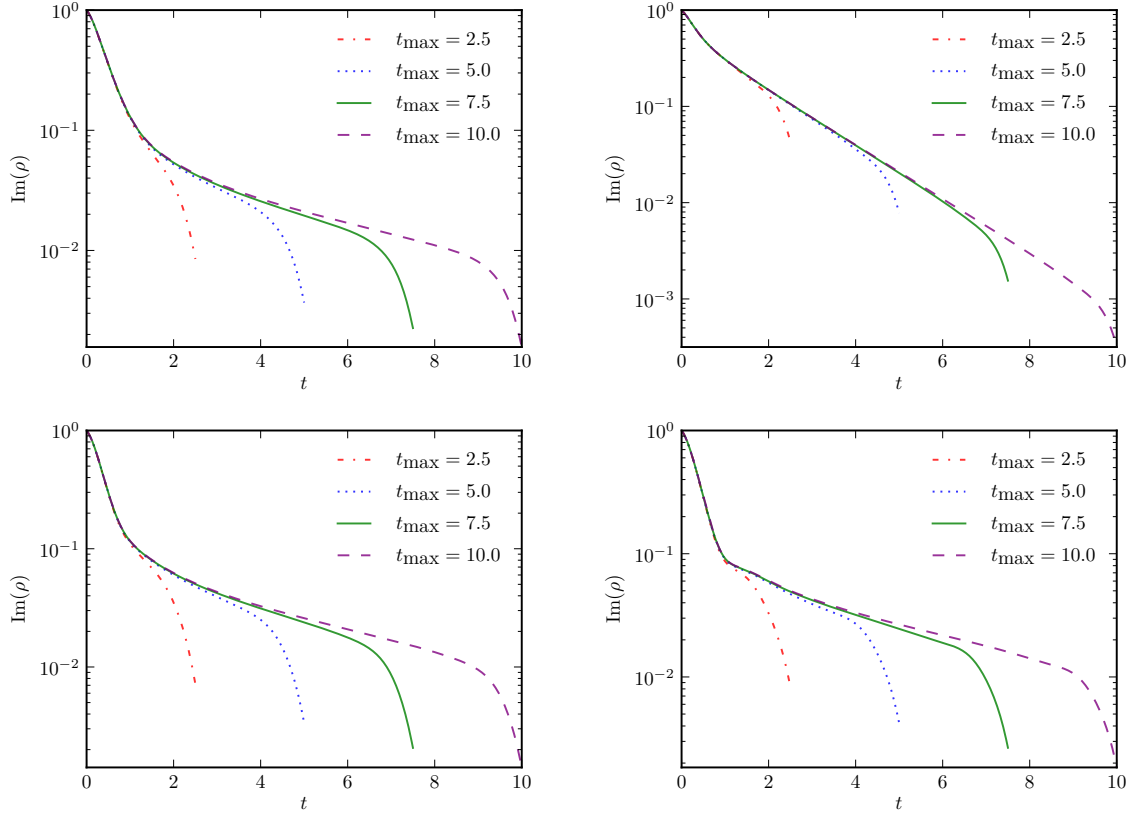


**Figure 5.10:** The imaginary part of the spectral function in time obtained in the direct (s)- (upper left), particle-particle (t)- (upper right), particle-hole (u)- (lower left), and stu-channel (lower right) with an interaction strength  $U = 5$  in the particle-hole symmetric setup at zero temperature and at different times.

### Intermediate Time Evolution

In Fig. 5.10, we show the results for the imaginary part of the spectral function in time at different times, obtained in the non-perturbative direct (s)-, particle-particle (t)-, particle-hole (u)-, and stu-channel resummations of the 2PI effective action, from upper left to lower right, in the particle-hole symmetric case,  $E_0 = -U/2$ . During the non-equilibrium time evolution of the Anderson quantum dot, we set the time-step size to  $\Delta t = 800^{-1}$ , the interaction strength  $U = 5$  and zero temperature.

Two points are note-worthy from this figure. First, the exponential decay in the tail becomes smaller with increasing total time and therefore affects the width of the Kondo peak in the Fourier domain,  $T_K$ . Second, the transition range between the two different exponential decays become broader, which is important for the Hubbard side bands. These effects are only present in the direct (s)-, particle-hole (u)-, and stu-channel resummations and most distinct in the latter. In the following section, we show the transient time-evolution in the whole real-time plane spectral

function, from which these effects are also observable. The spectral function obtained in the particle-particle channel resummation does not have these characteristics and therefore does not change much at different times.

### Transient Time Evolution

So far, we have only shown the spectral function at a certain absolute time along the relative time. Now, we present in Fig. 5.11 the imaginary part of the spectral function color coded in the whole real-time plane obtained in the non-perturbative direct (s)-, particle-particle (t)-, particle-hole (u)-, and stu-channel resummations, from top to bottom, for different interaction strengths,  $U = 2, 4, 6$ , from left to right, in the particle-hole symmetric case,  $E_0 = -U/2$ , at zero temperature. From Fig. 5.9, it can be seen that for early times the results do not depend on the time-step size in the range of  $\Delta t = 100^{-1}$  to  $\Delta t = 800^{-1}$  and therefore we set the time-step size to  $\Delta t = 50^{-1}$  for the investigation of the transient spectral function in the real-time plane.

The results obtained in the particle-particle (t)-channel resummation approximation shows only small differences between the different interaction strengths. Only a slight broadening is observable for increasing interaction strength at very early total times. Clearly, it is different in all other non-perturbative resummation channels of the 2PI effective action. The decrease of the imaginary part of the spectral function becomes faster for increasing interaction strengths. Contrarily, at smaller values the decrease is much weaker. The observable broadening for small values of the spectral function corresponds to the transition rate between the initial exponential decay, determined by the coupling to the leads,  $\Gamma$ , and the exponential decay in the tail, determined by the Kondo effect,  $T_K$ , which leads to the formation of the Hubbard side bands in the Fourier domain. This effect is stronger in the particle-hole (u)-channel in comparison to the direct (s)-channel but most pronounced in the stu-channel resummation approximation. From Fig. 5.11, we can recover the previous results but additionally, we can also observe how it evolves in real time.

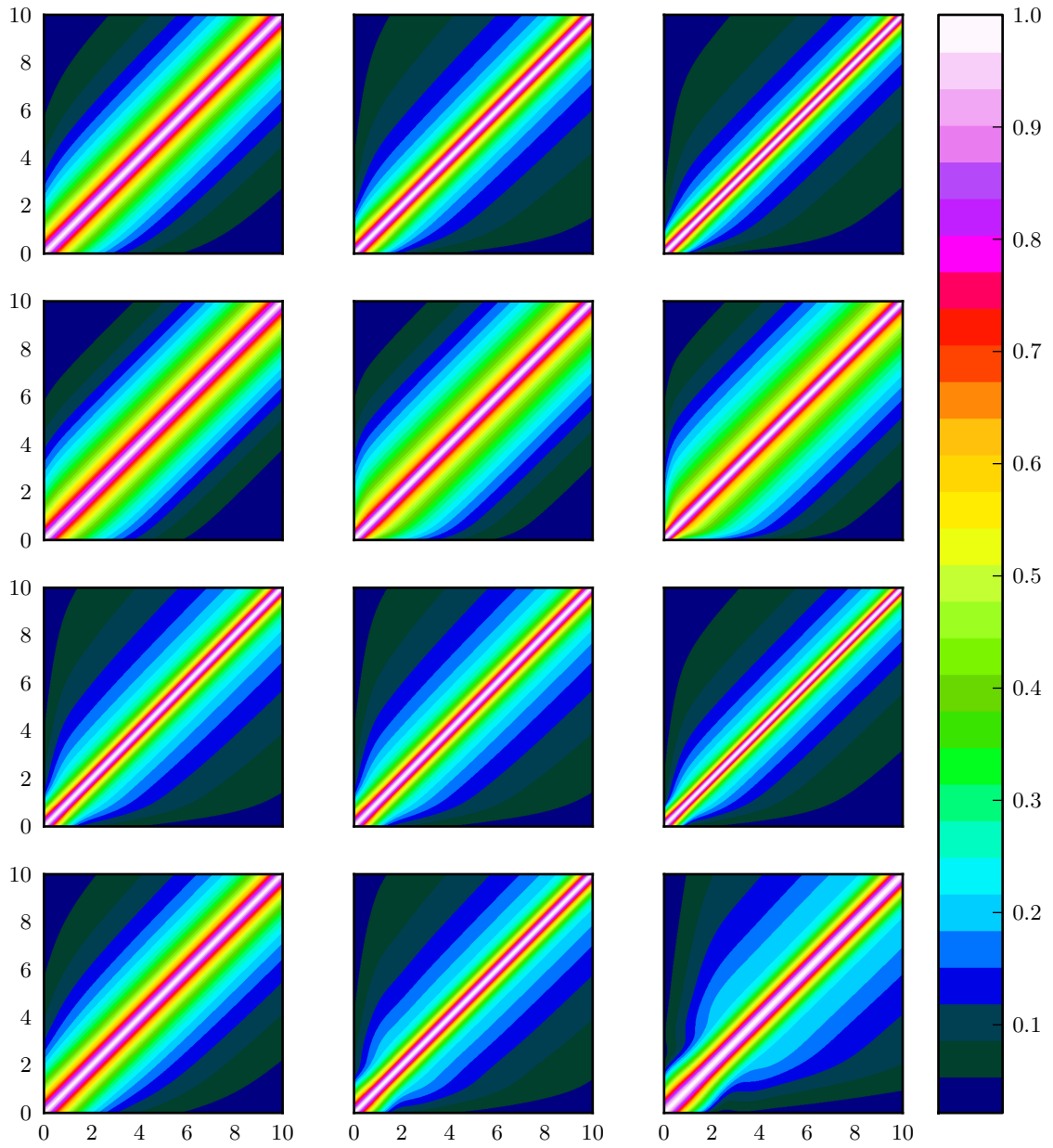


**Figure 5.11:** The transient time evolution of the imaginary part of the spectral function in the real time plane obtained in the direct (s)-, particle-particle (t)-, particle-hole (u)-, and stu-channel (from top to bottom) for different interaction strengths  $U = 2, 4, 6$  (from left to right) with a time-step size of  $\Delta t = 50^{-1}$  in the particle-hole symmetric setup at zero temperature. In particular, the formation of the Hubbard side bands is clearly observable in the stu-channel for the largest presented interaction strength,  $U = 6$ .

## 5.3 Non-Equilibrium Study of the Quantum Dot

In the previous section, we studied the quantum dot in equilibrium but with a quench in the coupling to the leads,  $\tau$ , and the interaction strength,  $U$ , which drives the system out of equilibrium, initially. In this section, we extend our study to the non-equilibrium case by applying a bias voltage to the quantum dot. The SIAM is designed to study non-equilibrium quantum transport; especially in the Kondo regime, where strong correlation effects also play a large role.

We investigate the transient current through the quantum dot as well as the current-voltage characteristics of the stationary current for interaction strengths, from small  $U = 2$  to intermediate  $U = 8$ . Afterwards, we also study the dependence of finite temperatures and magnetic fields on the stationary electrical current through the quantum dot. We compare our results for the stationary current with those obtained with functional renormalisation group (FRG) [60] and the iterative sum of path integrals (ISPI) [96–98, 205]. Similar studies have been done in Ref. [145], where 2PI results obtained in the direct (s)-channel were compared to FRG, ISPI, real-time quantum Monte Carlo (rtQMC) [151, 206–209] and time-dependent density matrix renormalisation group (tDMRG) [78–84] results. In this thesis, we extend the comparison to higher applied bias voltages and all possible non-equilibrium resummation schemes of the 2PI effective action. In Ref. [84], FRG and tDMRG, and in Ref. [148], FRG, tDMRG, ISPI, and rtQMC results were compared in the Kondo as well as the mixed valence regime.

For the non-equilibrium study of the quantum dot, we start initially with an empty and decoupled quantum dot from the thermally equilibrated leads such that the leads and quantum dot are two separated systems. This is exactly the same setup as before in the equilibrium study. Moreover this time, at the beginning of the time evolution, we instantaneously couple the non-interacting metallic leads to the quantum dot with a quench in the hybridisation parameter,  $\tau$ , interaction strength,  $U$ , and in the bias voltage,  $V$ . Without loss of generality, we assume that the chemical potential of the left lead is smaller than the right one. This leads to an electrical current from the left to the right lead and we regard this electrical current to be positive. We set the chemical potential of the non-interacting metallic leads symmetrically,  $\mu_L = -\mu_R = V/2$ , which yields a bias voltage of  $V = \mu_L - \mu_R$ . Also in this non-equilibrium setup, we assume that the leads will stay in thermal equilibrium over the entire time evolution and adjust the gate voltage so that the quantum dot is in the particle-hole symmetric point,  $E_0 = -U/2$ .

### 5.3.1 Transient Electrical Current

We start our discussion of the non-equilibrium quantum dot with the transient current. In Fig. 5.12, we show the time dependence of the electrical current,  $I$ , obtained in the direct (s)-, particle-particle (t)-, particle-hole (u)-, and stu-channels displayed in the upper left to lower right panel for different applied bias voltages,  $V$ , for an on-site interaction strength of  $U = 4$  and a time-step size of  $\Delta t = 300^{-1}$ . Since

there is a stationary electrical current before  $t = 3$ , we cut out this range from the total time evolution up to  $t_{\max} = 6$ . Before we start our time evolution (at  $t < 0$ ) the quantum dot is decoupled from the non-interacting metallic leads and is unoccupied. At the beginning of our time evolution, we immediately couple the leads to the dot and also apply the bias voltage, which initially results in zero electrical current. During the time evolution, the electrical current through the quantum dot evolves to a finite stationary value. From our results shown in Fig. 5.12, we observe three characteristic regions for all considered resummation schemes.

First, we find a linear rise in the electrical current for short time-scales. The initial slope of the electrical current is determined by the applied bias voltage,

$$\left. \frac{dI}{dt} \right|_{t=0} = 2V. \quad (5.15)$$

As we found in Subsec. 5.2.1, the initial slope of the time evolution of the occupation number of the quantum dot is independent of all probed on-site Coulomb repulsion strengths up to  $U = 16$ . This is also true for the electrical current because of an initially unoccupied quantum dot. The time range of this behaviour is longer for small bias voltages but ends at a smaller value. The effects induced by the interaction strength come into play after this linear behaviour.

Second, we find that the region after the linear rise up to the point where the electrical current becomes stationary now depends on the interaction strength as well as the applied bias voltage. For smaller interaction strengths and bias voltages, the stationary state is reached later. However, in all cases the time when the steady-state value is reached,  $t_{\text{st}}$ , is of the order of  $t_{\text{st}} \sim \Gamma^{-1}$ . This intermediate time region is characterised by the bias voltage as well as the interaction strength. On the one hand, high applied bias voltages lead to oscillations with larger amplitudes but on the other hand, larger Coulomb repulsions on the dot damp those oscillations faster. Furthermore, at larger interaction strengths the oscillations also show up for small bias voltages. In the following, we want to investigate the angular frequency in more detail. In Ref. [150] it was stated that the angular frequency depends linearly on the applied voltage and interaction strength,

$$\omega(V, U) = \frac{V + U}{2}, \quad (5.16)$$

which comes from the investigation of the interacting resonant level model (IRLM) in Ref. [91]. We extract the angular frequency by taking the derivative of the electrical current with respect to time. Then, the roots of the derivative correspond to the maxima and minima of the oscillations and from that, we can extract the angular frequency. We do this for five values of the bias voltage, from  $V = 16$  to  $V = 20$ , for fixed interaction strength. After that, we can easily fit the data to a linear function. For an interaction strength of  $U = 2$ , we get for all four non-perturbative

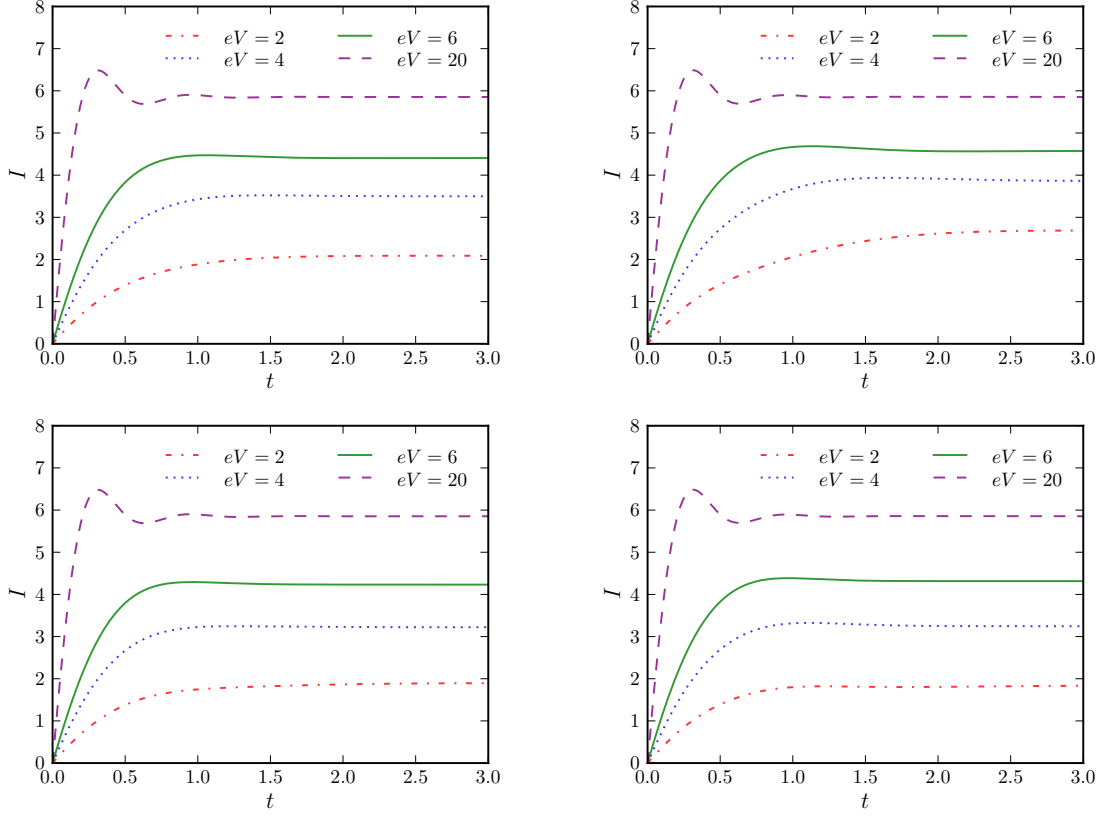


**Figure 5.12:** The transient current,  $I$ , through a quantum dot coupled to finite temperature leads at a temperature  $T = 0.1$  with an interaction strength  $U = 4$  obtained in direct (s)- (upper left), particle-particle (t)- (upper right), particle-hole (u)- (lower left), and stu-channels (lower right) with a time-step size of  $\Delta t = 300^{-1}$  for different applied bias voltages,  $V$ , in the particle-hole symmetric case,  $E_0 = -U/2$ .

resummation channels:

$$\begin{aligned}
 \text{s-channel: } \omega(V) &= 0.50 V + 0.07 \\
 \text{t-channel: } \omega(V) &= 0.50 V + 0.06 \\
 \text{u-channel: } \omega(V) &= 0.49 V + 0.14 \\
 \text{stu-channel: } \omega(V) &= 0.51 V - 0.10,
 \end{aligned} \tag{5.17}$$

and for an interaction strength of  $U = 4$ , we obtain:

$$\begin{aligned}
 \text{s-channel: } \omega(V) &= 0.51 V - 0.21 \\
 \text{t-channel: } \omega(V) &= 0.53 V - 0.75 \\
 \text{u-channel: } \omega(V) &= 0.50 V - 0.19 \\
 \text{stu-channel: } \omega(V) &= 0.54 V - 0.94.
 \end{aligned} \tag{5.18}$$

Our results are in perfect agreement with Eq. (5.16) for the dependence on the bias voltage  $\omega \sim 0.5V$ . The largest deviation,  $\Delta\omega(V) = 0.04$ , is in the stu-channel for  $U = 4$ . Contrarily, we cannot confirm the dependence on the interaction strength given in Eq. (5.16) from Ref. [150]. The results are far from the proposed dependency.

The time dependence of the electrical current can be calculated analytically at mean-field order if we assume that the occupation number is constant. In the particle hole symmetric case,  $E_0 = -U/2$ , and with symmetrically adjusted chemical potentials the stationary occupation number is  $n = 0.5$ . Therefore, the effective mass term in the spectral function at mean-field order, given in Eq. (4.103) vanishes. We insert this into Eq. (4.121) and obtain for the electrical current

$$I(t) = 4 \int_0^t du \frac{e^{-\Gamma u} \sin\left(\frac{V}{2}u\right)}{u}. \quad (5.19)$$

This is the exact solution with vanishing interaction strength. Nevertheless, it is a good approximation because at the beginning we start with an initially empty dot which switches-off effectively the interaction. From this consideration we can understand the dependence on the bias voltage.

Third, once the system has reached the stationary state, it remains there. The exact steady-state value depends on the on-site repulsive Coulomb interactions, as well as the applied bias voltage. For a fixed interaction strength the electrical current increases with the bias voltage and for a fixed bias voltage the electrical current decreases with the interaction strength. We discuss the stationary current in more detail in the next subsection.

In all resummation schemes, we can observe these characteristics. The stationary value of the electrical current in the particle-particle (t)-channel is larger than in any other.

### 5.3.2 Stationary Electrical Current and Conductance

In this subsection, we want to focus on the stationary electrical current through the quantum dot and its dependence on the applied bias voltage. In the left column of Fig. 5.13, we show our results for the electrical current obtained in the direct (s)-, particle-particle (t)-, particle-hole (u)- and stu-channel from small,  $U = 2$ , to intermediate,  $U = 8$ , interaction strengths depicted from top to bottom panel and compare them to FRG results. We sample the bias voltage in steps of  $\Delta V = 0.5$ , starting from  $eV = 1.0$  and evolve the system up to  $t_{\max} = 6$  with a time-step size of  $\Delta t = 300^{-1}$ . For smaller values of the bias voltage, we have additional data points at  $V = 0.02, 0.05, 0.2, 0.35, 0.5$  and evolved the system up to  $t_{\max} = 40$ . Moreover, we can set the current at zero bias voltage to zero because with no bias voltage there will be no net current. Therefore, every curve in each panel consists of 45 data points. The stationary values of the transient currents shown in Fig 5.12 correspond to the appropriate values of the bias voltage in the left middle panel of Fig. 5.13. In the right column, we show the corresponding differential conductance



of the left column, where we trivially continue the values to negative bias voltages of the electrical current using anti-symmetry.

In Sec. 4.5, we showed that the maximum electrical current through the quantum dot is  $I_{\max} = 2\pi$ . This will be the case for the results obtained for any approximation of the 2PI effective action because we set the value of the spectral function at equal times to  $\rho(t, t) = i$ .<sup>4</sup> This is directly connected to the integral over this function in Fourier space. For large bias voltages,  $V > U + 2\Gamma$ , our numerical results approach the maximum current asymptotically and fit perfectly with the FRG results for arbitrary interaction strengths. From the naive point of view, a significant electrical current can only flow when the bias voltage is reaching the order of the interaction strength,  $V \approx U$ , because the bias voltage then reaches the two available states in the quantum dot. This is an important requirement for charge transport.

However, from the numerical results, we can see already that for very small bias voltages an electrical current flows. This behaviour is highly non-trivial and governed by the Kondo effect. In Sec. 3.2, we argued that the Kondo effect gives rise to additional states at the Fermi edges of the leads. The range of small bias voltages is also accessible with linear response theory and therefore, the initial slope of the electrical current is known not only theoretically but also experimentally [21, 23]. Due to the Kondo effect, the electrical conductance reaches its maximum which is the conductance quantum<sup>5</sup> for zero bias voltage,  $G_{\text{dif}}(0) = G_0$ . Thus, the quantum dot shows a perfect transmission property at that point.

For the smallest probed interaction strength,  $U = 2$ , our results are in perfect accordance with FRG results in the whole range of bias voltages. Also, the mean-field results, which are independent of the interaction strength (see Sec. 4.5), give a good approximation for that interaction strength. It is clear that the results obtained in the particle-particle (t)- channel are a bit off the results obtained in the other non-perturbative resummations of the 2PI effective action and FRG results. This effect becomes more pronounced for larger interaction strengths.

The results for an interaction strength of  $U = 4$  obtained in the direct (s)-, particle-hole (u)-, and stu-channels agree very well with FRG results. However, the results obtained in the particle-particle (t)- channel are clearly off and show characteristics similar to the mean-field results. In comparison to the smaller interaction strengths, the electrical current shows more varied characteristics. This is seen in the differential conductance as two sidepeaks located at  $V = \pm U$  because the two energy levels in the quantum dot are separated by the interaction strength,  $U$ . When the bias voltage reaches that value, one of the two chemical potentials of the leads is located at the gate voltage and the other at the double-occupied level. This leads to an enhanced differential conductance. Also, the region for very small bias voltages, which is hard to access because of the long-time effects arising from the Kondo effect, is in good agreement with the prediction. The peak in the differential conductance at zero bias voltage reaches almost  $G_{\text{dif}}(0) = 2$ .

---

<sup>4</sup>It is  $\int_{-\infty}^{\infty} \frac{d\omega}{2\pi} \int_{-\infty}^{\infty} ds e^{-i\omega s} \rho(s) = \int_{-\infty}^{\infty} ds \delta(s) \rho(s) = i$ , with the relative time  $s = t - t'$ .

<sup>5</sup>The conductance quantum is defined as  $G_0 = 2\frac{e^2}{h}$ , see Sec. 4.5.

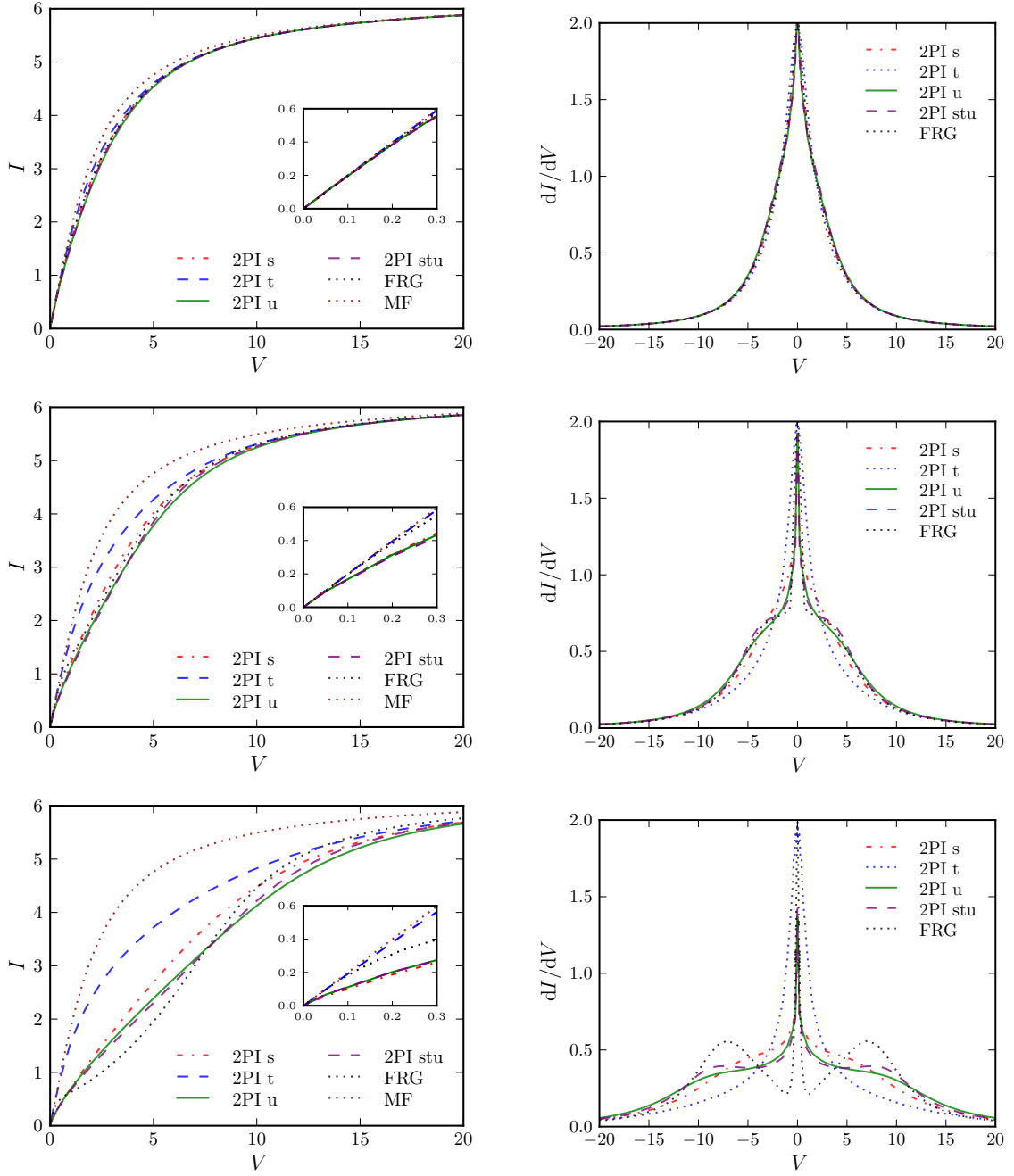


**Figure 5.13:** The stationary current,  $I$ , through a quantum dot (left column) and the differential conductance (right column) dependence on the applied bias voltage,  $V$ , obtained in different resummation channels compared to the FRG results in Ref. [148] for different interaction strengths,  $U = 2, 4, 8$  (from top to bottom) in the particle-hole symmetric case,  $E_0 = -U/2$ , and a finite temperature of  $T = 0.1$ . The system was evolved to the total time  $t_{\max} = 40$  for bias voltages  $V \leq 0.5$  and  $t_{\max} = 6$  otherwise with a time-step size of  $\Delta t = 300^{-1}$ .

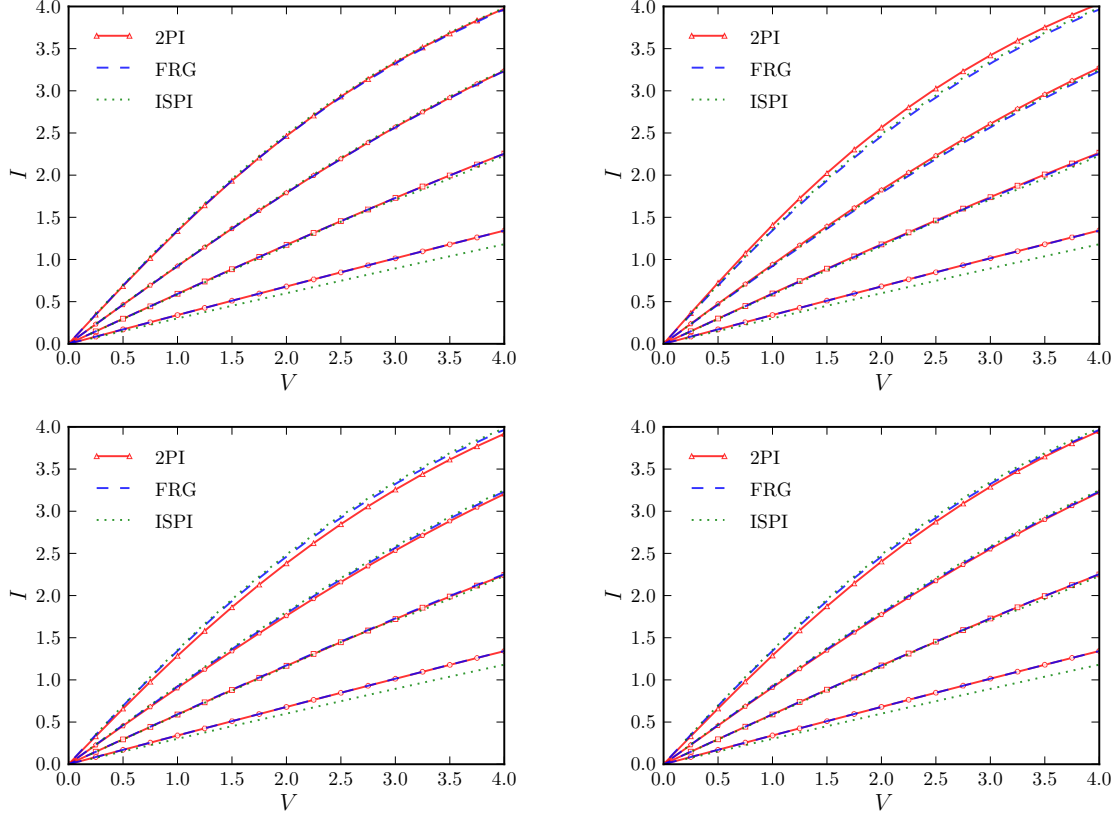


**Figure 5.14:** The stationary current,  $I$ , through the quantum dot coupled to finite temperature leads at a temperature of  $T = 0.4, 1.0, 2.0, 4.0$  corresponding to steep-to-flat slopes of the curves in the particle-hole symmetric case,  $E_0 = -U/2$ , in dependence on the applied bias voltage,  $V$ , obtained in the direct (s)- (upper left), particle-particle (t)- (upper right), particle-hole (u)- (lower left), and stu-channels (lower right) with an interaction strength  $U = 2$  compared with FRG and ISPI results in Ref. [148]. The system was evolved to the total time  $t_{\max} = 6$  with a time-step size of  $\Delta t = 300^{-1}$ .

For even larger interaction strengths,  $U = 8$ , the deviation of all non-perturbative resummation channels to the FRG results becomes clear but show the correct main characteristics apart from the results obtained in the particle-particle (t)- channel. The best agreement is found for the stu-channel. For very small bias voltages, the stationary current was not yet reached and therefore, the results in that range can be improved for longer time evolutions. We then expect to attain the correct value with the 2PI effective action. At intermediate bias voltages, our results are above the FRG results and later below. However, all non-perturbative resummation schemes reach the correct maximum electrical current asymptotically.

### 5.3.3 Temperature Dependence of the Stationary Electrical Current

In this subsection, we discuss the temperature-dependence of the electrical current. The physical setup is analogous to the previous subsection but with different values of temperature,  $T = 0.4, 1.0, 2.0, 4.0$ . We let the system evolve until  $t_{\max}$  with a time-step size of  $\Delta t = 300^{-1}$  and sample the bias voltage in steps of  $\Delta V = 0.25$ . In Fig. 5.14, we show the results obtained in the direct (s)-, particle-particle (t)-, particle-hole (u)-, and stu-channel from upper left to lower right panel and in addition to this, results from FRG and ISPI for an interaction strength of  $U = 2$ . With increasing temperature, the electrical current becomes smaller for all bias voltages.

In the direct (s)- channel, the results are in perfect agreement with the FRG results over the entire range of bias voltages. Also, results obtained in the other channels generally agree, apart from the smallest temperature,  $T = 0.4$ . While the results in the particle-particle (t)- are larger, the results from the particle-hole (u)-, and stu-channels are smaller than the FRG results. However, the deviations are small and there is still a good agreement between the different methods.

### 5.3.4 Stationary Electrical Current and Conductance with a Magnetic Field

In this subsection, we want to study the influence of an applied external magnetic field to the electrical current voltage characteristic of the quantum dot. We also choose a small interaction strength,  $U = 2$ , because we know from our previous investigation that our results agree perfectly with the results obtained from FRG. Thus, we can isolate the effect of the magnetic field and compare our results to those from FRG. The magnetic field is applied to the quantum dot before the time evolution starts and is kept switched on. We evolved the system in the particle-hole symmetric set-up until  $t_{\max} = 6$  with a time-step size of  $\Delta t = 300^{-1}$  and did this for bias voltages from  $V = 0$  to  $V = 20$  in steps of  $\Delta V = 0.5$ . Therefore, we have 41 data points for each graph representing the electrical current. For the differential conductance, we simply extended the values to negative bias voltages using anti-symmetry.

In the case of a finite applied bias voltage to the quantum dot, the Kondo resonance in the spectral function splits into two because of the Zeeman effect. Thus, the Kondo peaks are shifted away from the Fermi energies of the two leads. This leads to a smaller electrical current for small bias voltages and a smaller differential conductance even for zero bias voltage. This effect is stronger with increasing magnetic field. The conductance should rise with increasing bias voltage until the bias voltage is equal to the Zeeman splitting of the states,  $V = \mu B$ , because at that point, a split Kondo peak is located at the Fermi energy of the leads. For even higher values of the bias voltage, the differential conductance falls off. Thus, two peaks in the differential conductance are expected at  $V = \pm \mu B$ . This was proposed theoretically in Ref. [201] and shown experimentally in Ref. [23].

In Fig. 5.15, we show our results for the electrical current in the left column and

### 5.3 Non-Equilibrium Study of the Quantum Dot

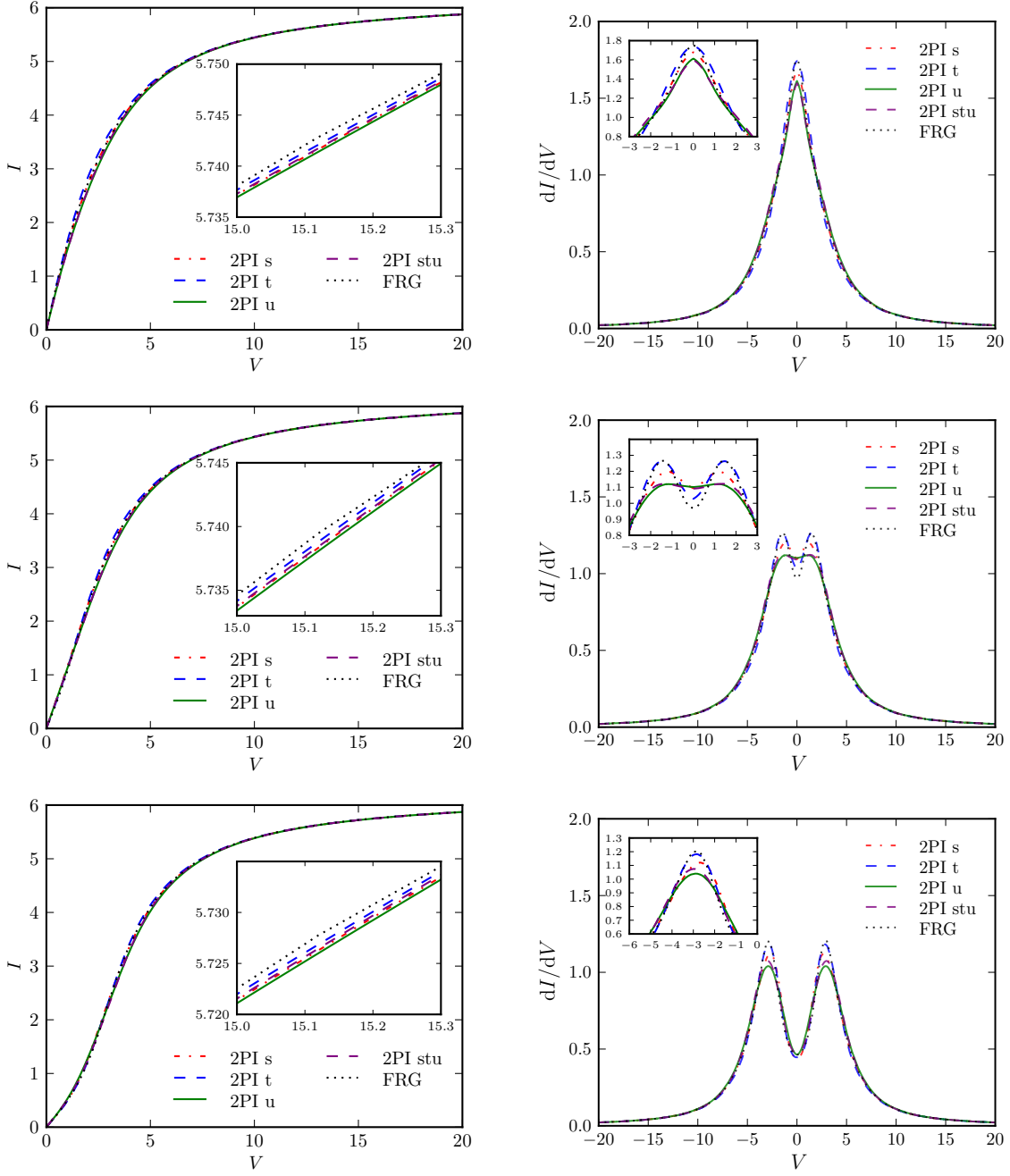


**Figure 5.15:** The stationary current,  $I$ , through a quantum dot (left column) and the differential conductance (right column) dependence on the applied bias voltage,  $V$ , obtained with an interaction strength  $U = 2$  and a finite temperature of  $T = 0.1$  in different resummation channels compared to the FRG results in Ref. [148] for different magnetic fields,  $B = 0.2, 0.6, 1.2$  (from top to bottom) in the particle-hole symmetric case,  $E_0 = -U/2$ . The system was evolved to the total time  $t_{\max} = 6$  with a time-step size of  $\Delta t = 300^{-1}$ .

the corresponding differential conductance for three different values of the magnetic field in the upper  $B = 0.2$ , middle  $B = 0.6$ , and lower panel  $B = 1.2$  of the right column. In each panel, we compare the results we obtained in the non-perturbative direct (s)-, particle-particle (t)-, particle-hole (u)-, and stu-channel resummation of the 2PI effective action to FRG results.

For all three probed magnetic fields the results obtained in the direct (s)-, particle-particle (t)-, particle-hole (u)-, and stu-channel are very close to each other. Only in the close-up of the electrical current results, which shows the results for large bias voltages, is a deviation visible. The particle-particle (t)- channel results are closest to the results obtained in FRG. The electrical current voltage characteristics are easier to see in the results for the differential conductance. The decrease of the conductance at zero bias voltage for increasing magnetic fields is clearly visible. Also, the enhanced conductance is present at the Zeeman splitting energies. The deviation between our results and FRG are at the maxima and minima of the differential conductance. However, in general, both methods show good agreement with each other.

## 5.4 Summary

In this chapter, we showed the numerical results we achieved from our numerical efforts to solve the Kadanoff–Baym equations of motion for the statistical propagator and spectral function derived from the two-particle irreducible (2PI) effective action, with the non-perturbative channel resummation approximation of the self-energy for a quantum dot with on-site Coulomb repulsion interaction, coupled to two metallic non-interacting leads described by the single impurity Anderson model (SIAM). In the first section, we presented how the Gaussian initial conditions enter our dynamical equations. Furthermore, we discussed the algorithm we used to solve the equations numerically.

In the second section, our investigation focused on the case of leads with the same chemical potentials, which is referred to as the equilibrium setup. However, we applied a quench in the tunnelling parameter and the interaction strength at the beginning of the time evolution, which drives the quantum dot out of equilibrium. During the time evolution, the system evolves into a stationary state. We started with the discussion of the occupation number of the quantum dot in the particle-hole symmetric case from small to large interaction strengths. Our results for the time evolution of the occupation number were compared to Monte-Carlo data and we found very few deviations. We also showed results for the stationary occupation over a high range of gate voltages, such that the quantum dot runs through the unoccupied, mixed valence, Kondo, and double occupied regimes. Up to large interaction strengths, we found a good agreement with the results in the literature. The main focus of this section was the time evolution of the spectral function and the investigation of its properties. We showed the spectral function as a function of time at small, intermediate and late times and found that at early times the spectral

function decays exponentially with rate on the order of the hybridisation while at later times, where the Kondo effect sets in, the exponent becomes very small. We found that for smaller time-step sizes the exponent becomes smaller and is close to the predicted Kondo temperature for interaction strengths around  $U = 4$ . For higher interaction strengths, the exponential decay becomes faster. The results obtained in the direct (s)-, particle-hole (u)-, and stu-channel are very similar to each other but the particle-particle (t)-channel starts deviating from the others at interaction strengths  $U \gtrsim 4$ .

In the third section, we applied a finite bias voltage to the quantum dot to study the electrical current voltage characteristics and the influence of different parameters, such as: interaction strength, temperature, and magnetic field. We started our investigation with the non-equilibrium time evolution of the electrical current for an interaction strength of  $U = 4$ . At small bias voltages, we observed long-time effects due to the Kondo effect. The initial rise of the electrical current is independent of the interaction strength but determined by the applied bias voltage. In a certain parameter range for the interaction strength and bias voltage, a damped oscillation is observed with an angular frequency proportional to the bias voltage,  $\omega \sim V/2$ . We compared our results for the stationary current with those from FRG and found, for small interaction strengths, a very good agreement in all non-perturbative resummation schemes. This starts to break down with increasing interaction strengths. However, the results obtained in the direct (s)-, particle-hole (u)- and stu-channel can render the characteristics of the differential conductance. Furthermore, our results for the temperature- and magnetic field-dependence of the stationary current agree perfectly with FRG results.





# Chapter 6

## Conclusion

In this thesis, we employed the real-time Schwinger–Keldysh path integral formulation to derive the two-particle irreducible (2PI) effective action to investigate the non-equilibrium time evolution of an Anderson quantum dot. From the 2PI effective action, we used the variational principle to find the exact Kadanoff–Baym equations of motion for the full propagator. These dynamic equations for the statistical propagator and spectral function are the central equations from which we numerically obtained all the results shown in this thesis.

The underlying model of our investigation is the single impurity Anderson model (SIAM), which describes a zero-dimensional quantum dot with two available energy levels and on-site Coulomb repulsion, coupled to two leads with finite temperature and chemical potential. The zero-dimensional approximation of the quantum dot is justified because real quantum dots are nanoscale devices with a discrete spectrum. Furthermore, the physics of the quantum dot depends on whether the total number of electrons are even or odd. Therefore, one orbital on the quantum dot, which can hold up to two electrons, is a very good approximation. The tunnelling between the leads and the quantum dot is taken into account exactly by integrating out the leads' fields in the path integral formulation. The commonly used wide flat band approximation for the leads' density of states is also used in this thesis. This approximation considers a constant density of states in the range of the bandwidth. In general, this is only true for two-dimensional systems, however it is also reasonable for our purposes. We assume that the leads are in thermal equilibrium and can be described by a grand canonical ensemble during the entire time evolution.

At the beginning of the time evolution, the leads and the quantum dot, which is described by a general density matrix determined by the initial occupation, are two separate systems. Initially, we set the occupation of the quantum dot to zero. Afterwards, we performed a hybridisation and interaction quench which drives the system out of equilibrium, even for equal chemical potentials in the leads. Our numerical results, obtained from solving the real-time Kadanoff–Baym equations of motion numerically in the non-perturbative direct (s)-, particle-particle (t)-, particle (u)- and stu-channel resummations, are divided into two parts, one with equal chemical potentials in the leads, and the other with an applied bias voltage.

In the case with an applied bias voltage, we extended the work given in Ref. [145] by the non-perturbative particle-particle (t)-, particle-hole (u)-, and stu-channel re-

summation schemes and also studied the transient electrical current through the quantum dot. Similar to the occupation number in the previous case, the short-time electrical current is independent of the interaction strengths and only determined by the applied bias voltage. Afterwards, interaction effects also become important and strongly influence the evolution into the stationary state. Furthermore, in this non-equilibrium case with an applied bias voltage, we found the results to be in very good accordance with other established methods, such as the functional renormalisation group and the iterative sum of path integrals up to an interaction strength of  $U \approx 4$ . For interaction strengths of  $U = 4$  and  $U = 8$ , best results were obtained in the stu-channel approximation. In the Kondo limit of small bias voltages we observed long-time effects until the electrical current reaches its stationary state. For larger interaction strengths, it takes more time. At large bias voltages, which is beyond the linear response regime, the 2PI effective action is able to render the correct asymptotic stationary currents. Moreover, we also investigated the influence of finite temperatures and magnetic fields and found a very good agreement with the results obtained from the aforementioned methods for all non-perturbative resummation channels.

In the case of equal chemical potentials in the leads, we studied the transient as well as the stationary occupation numbers, with the main focus set on the spectral function of the quantum dot. In the particle-hole symmetric setup, the expected occupation number is obtained in all non-perturbative resummation schemes. Moreover, at very short times, we found that the occupation number is independent of the interaction strength. This can be understood from direct considerations of the SIAM Hamiltonian because the on-site interaction term is given by the occupation operators for up and down spins. Since we have an initially empty quantum dot, the interaction strength should not play a role. We compared our results with those from the exact numerical Monte Carlo data given in Ref. [152] and found a very good quantitative agreement for all interaction strengths. We also studied the stationary occupation number of the quantum dot for different gate voltages, such that the quantum dot runs through the empty to the double-occupied state. In the whole range of probed gate voltages, we obtained the qualitatively correct results compared to exact analytic results. The main focus was on the time evolution of the quantum dot's spectral function in the particle-hole symmetric setup for a large range of interaction strengths. In this setup, the main features of the spectral function at late times is known but the time evolution from a certain initial state is not. This provides the opportunity to check our results at late times. One of the cardinal characteristics of the spectral function is the width of the Kondo peak, also referred to as the Kondo temperature. It is known from exact Bethe ansatz calculations in the stationary limit that the Kondo temperature decreases exponentially for large interaction strengths, *cf.* Eq. (3.15), and also experiments showed this behaviour. The reproduction of this exponential scaling is a very challenging task, where most other methods fail. Our results are in a very good accordance with the exact analytic solution up to interaction strengths of  $U = 5$  and a good accordance up to  $U = 6$ .

The main achievement of this thesis is the detailed investigation of the spectral

function, which so far has not been carried out in the literature to our knowledge. This was only possible due to the tremendous improvement of the numerics for solving the real-time integro-differential Kadanoff–Baym equations of motion to a much higher accuracy, in comparison to works which used the 2PI effective action to investigate non-equilibrium time evolution as in Refs. [116, 145]. We treated differential terms as well as the non-Markovian memory integrals in the dynamic equations consistently with a higher-order predictor-corrector algorithm. With that, we were able to calculate the time evolution starting from an arbitrary initial condition to the stationary state and find the correct exponential scaling of the Kondo temperature up to interaction strengths  $U = 6$ , which is a huge success.

Additionally, this enabled us to study the formation of the Hubbard side bands. This feature of the spectral function is most pronounced in the non-perturbative resummation of the *stu*-channel. The effects of the Hubbard side bands are due to the coupling to the leads and play an important role for short relative times. Furthermore, the formation takes place at earlier times than the Kondo effect in the absolute time. We showed the whole real-time plane of the spectral function from which this formation is clearly visible.

There is only one work in the literature [145] where the 2PI effective action was applied to the SIAM to study its non-equilibrium time evolution in the Kondo regime. In this thesis, we have demonstrated that the essential physics of the quantum dot is captured in non-linear effects solely in non-perturbative resummation schemes. We compared the different non-perturbative resummation channels and found, in most cases, the best results when we combined all standard resummation channels by summing them up to the new defined *stu*-channel. Furthermore, we demonstrated that the 2PI effective action is a very good method for tackling the very demanding long-time effects in the Kondo regime.

We obtained the best results we could achieve with the algorithm used in our numerics and the available computer power within the time constraints of this project. With our work, we have paved the way for ongoing projects in this field. Due to the exponential scaling of the Kondo temperature, there are two points that are important for larger interaction strengths. First, it is much tougher to obtain numerically precise results in that regime. This can be improved by decreasing the time step size. Second, the Kondo temperature is an energy scale of the system but also imposes a time scale. From this, it follows that the expected time for building up the tail in the spectral function increases exponentially with the interaction strength and therefore, the results are supposed to improve for larger times. However, this is a very challenging issue because both points demand an increasing number of time steps and therefore computational resources. For future work, the key point is to improve the numerics to access later times with smaller time step sizes in order to enhance the results for larger interaction strengths.



# Appendix A

## Numerical Methods

In this section, we want to review all numerical methods and concepts used in order to find solutions for non-equilibrium physics for the single impurity Anderson model described by the Kadanoff–Baym equations of motion, which are a set of coupled integro-differential equations. For this, there are two key aspects to consider. First, how to solve a differential equation and second, how to evaluate an integral numerically. We tackle the first point with a linear multistep method and the latter with quadrature rule integration methods. The employed methods can be found in standard textbooks about numerical mathematics, as in Refs. [210–212].

We limit our considerations to the one-dimensional case and simply transfer this to the Kadanoff–Baym equations of motion. Since the spectral and statistical functions of the full propagator obey symmetry relations, our calculations are restricted to the lower triangle of the real time plane, therefore we can regard our problem as quasi one-dimensional and the occurring integrals as one-dimensional convolutions.

### A.1 Linear Multistep Methods for Solving Ordinary Differential Equations

We are interested in solving ordinary differential equations. The problem is given by a differential equation and an initial value as

$$y'(t) = f(t, y(t)) \quad \text{with } y(0) = y_0. \quad (\text{A.1})$$

The goal is to find a numerical solution to this problem. Beside the one-step methods like Runge–Kutta, where only the current time is needed to calculate the next time point, there are also multistep methods, which use more than the current time. The most general form of the linear multistep method is given by

$$y_{n+1} + a_0 y_n + a_1 y_{n-1} + \dots + a_s y_{n-s} = \Delta t (b_{-1} f_{n+1} + b_0 f_n + \dots + b_s f_{n-s}) \quad (\text{A.2})$$

with constant coefficients  $a_i$  and  $b_j$  and where we have used the shorthand notation  $y_k = y(t_k)$ ,  $f_k = f(t_k, y(t_k))$  and time step size  $\Delta t$ . It is called linear because the appearing values of  $y_k$  are a linear superposition. In the case of  $b_{-1} \neq 0$ , the next point that is needed has not been calculated. On the one hand side, this makes the

algorithm more complicated because a set of linear equations must be solved at every time step but on the other hand, the algorithm is more stable. We call this method implicit or Adams–Moulton and in the case of  $b_{-1} = 0$ , explicit or Adams–Bashforth.

### A.1.1 Adams–Bashforth

The basic idea is to interpolate the function  $f$  around the current time with Lagrange polynomials

$$f(t) = \sum_{i=k-n}^k h(t_i)l_i(t), \quad (\text{A.3})$$

with

$$l_i(t) = \prod_{\substack{j \neq i \\ k-n \leq j \leq k}} \frac{t - t_j}{t_i - t_j}. \quad (\text{A.4})$$

$n$  denotes the order of the Lagrange polynomial and also the number of values of the past that are taken into consideration for the next point in the future and consequently, the order of the Adams–Bashforth algorithm. Substituting Eq. (A.3) into Eq. (A.1), we obtain

$$\begin{aligned} \int_{t_k}^{t_{k+1}} y'(t) dt &= \sum_{i=k-n}^k f_i \int_{t_k}^{t_{k+1}} l_i(t) dt, \\ y_{k+1} &= y_k + \sum_{i=k-n}^k f_i \int_{t_k}^{t_{k+1}} l_i(t) dt. \end{aligned} \quad (\text{A.5})$$

We performed this calculation for  $n \in \{0, 1, 2, 3, 4\}$ . The Adams–Bashforth formulae up to fourth order read:

$$y_{k+1} = y_k + \Delta t f_k, \quad (\text{A.6})$$

$$y_{k+1} = y_k + \frac{\Delta t}{2} (3f_k - f_{k-1}), \quad (\text{A.7})$$

$$y_{k+1} = y_k + \frac{\Delta t}{12} (23f_k - 16f_{k-1} + 5f_{k-2}), \quad (\text{A.8})$$

$$y_{k+1} = y_k + \frac{\Delta t}{24} (55f_k - 59f_{k-1} + 37f_{k-2} - 9f_{k-3}), \quad (\text{A.9})$$

$$y_{k+1} = y_k + \frac{\Delta t}{720} (1901f_k - 2774f_{k-1} + 2616f_{k-2} - 1274f_{k-3} + 251f_{k-4}). \quad (\text{A.10})$$

### A.1.2 Adams–Moulton

The calculation for the coefficients for the Adams–Moulton algorithm is very similar to Adams–Bashforth. We just have to shift the summation index by one,

$$\int_{t_k}^{t_{k+1}} y'(t) dt = \sum_{i=k+1-n}^{k+1} f_i \int_{t_k}^{t_{k+1}} l_i(t) dt, \quad (\text{A.11})$$

$$y_{k+1} = y_k + \sum_{i=k+1-n}^{k+1} f_i \int_{t_k}^{t_{k+1}} l_i(t) dt$$

and  $n$  still denotes the order of the Lagrange polynomials and the order of the Adams–Bashforth algorithm. For the first five orders we obtain:

$$y_{k+1} = y_k + \frac{\Delta t}{2} (f_{k+1} + f_k), \quad (\text{A.12})$$

$$y_{k+1} = y_k + \frac{\Delta t}{12} (5f_{k+1} + 8f_k - f_{k-1}), \quad (\text{A.13})$$

$$y_{k+1} = y_k + \frac{\Delta t}{24} (9f_{k+1} + 19f_k - 5f_{k-1} + f_{k-2}), \quad (\text{A.14})$$

$$y_{k+1} = y_k + \frac{\Delta t}{720} (251f_{k+1} + 646f_k - 264f_{k-1} + 106f_{k-2} - 19f_{k-3}), \quad (\text{A.15})$$

$$y_{k+1} = y_k + \frac{\Delta t}{1440} (475f_{k+1} + 1427f_k - 798f_{k-1} + 482f_{k-2} - 173f_{k-3} + 27f_{k-4}). \quad (\text{A.16})$$

### A.1.3 Predictor-Corrector

Implicit methods are more accurate than explicit methods but they require much more numerical effort because for every time step, an additional equation has to be solved. One way to utilise the advantages of implicit methods is to introduce a two-step procedure. In the first step, an explicit method like Adams–Bashforth is used to predict the next value and in the second step, an implicit method like Adams–Moulton is applied to correct the predicted value to increase the accuracy. The correction step can be iterated arbitrarily. Such methods are also easy to implement in the numerics.

In our numerics, we start with an Adams–Bashforth predictor of order zero and an Adams–Moulton corrector of the order one. We increase the order by one after every time step until we arrive at order two for the predictor and three for the corrector

$$y_{k+1} = y_k + \frac{\Delta t}{12} (23f_k - 16f_{k-1} + 5f_{k-2}), \quad (\text{A.17})$$

$$y_{k+1} = y_k + \frac{\Delta t}{24} (9f_{k+1} + 19f_k - 5f_{k-1} + f_{k-2}).$$

We then iterate the corrector twice.

## A.2 Integration Methods

In our numerics, we use integration methods that obey the quadrature rule. The basic concept is to approximate the function we want to integrate with a polynomial.

### A.2.1 Newton–Cotes

In the closed Newton–Cotes method, the end points of the integration interval are also taken to evaluate the integral. The integration range  $[a, b]$  is divided into  $n$  equally spaced points,  $x_i$ , with  $i \in \{1, 2, \dots, n\}$ . The integrated function,  $f$ , is approximated by a polynomial,  $p_n$ , of order  $n$ ,

$$\int_a^b f(x) dx \approx \int_a^b p_n(x) dx \quad (\text{A.18})$$

with

$$p_n(x) = \sum_{i=0}^n f(x_i) l_{in}(x). \quad (\text{A.19})$$

In the Newton–Cotes method, Lagrange polynomials  $l_{in}$  are used. From the definition in Eq. (A.4), it follows that the interpolation polynomial is equal to the function at the nodes,  $p_n(x_i) = f(x_i)$ . The integral follows:

$$\int_a^b f(x) dx \approx (b - a) \sum_{i=0}^n f(x_i) \frac{1}{b - a} \int_a^b l_{in}(x) dx. \quad (\text{A.20})$$

We define the weights  $w_i$ , such that

$$w_i = \frac{1}{b - a} \int_a^b l_{in}(x) dx. \quad (\text{A.21})$$

From the special case  $f(x) = 1$ , it is easy to see that the weights fulfil the condition

$$\sum_{i=0}^n w_i = 1. \quad (\text{A.22})$$

Then the value of the integral using the Newton–Cotes method is given by

$$\int_a^b f(x) dx \approx \sum_{i=0}^n w_i f(x_i). \quad (\text{A.23})$$

With  $n + 1$  nodes polynomials up to the order of  $n$  and  $n + 1$  for even  $n$  can be integrated exactly.



Explicitly, the first five orders of the closed Newton–Cotes formulae (trapezoid, Simpson, Simpson 3/8, Boole, and 6-point) read:

$$\int_{t_k}^{t_{k+1}} f(x) dx = \frac{\Delta t}{2} (f_k + f_{k+1}), \quad (\text{A.24})$$

$$\int_{t_k}^{t_{k+2}} f(x) dx = \frac{2\Delta t}{6} (f_k + 4f_{k+1} + f_{k+2}), \quad (\text{A.25})$$

$$\int_{t_k}^{t_{k+3}} f(x) dx = \frac{3\Delta t}{8} (f_k + 3f_{k+1} + 3f_{k+2} + f_{k+3}), \quad (\text{A.26})$$

$$\int_{t_k}^{t_{k+4}} f(x) dx = \frac{4\Delta t}{90} (7f_k + 32f_{k+1} + 12f_{k+2} + 32f_{k+3} + 7f_{k+4}), \quad (\text{A.27})$$

$$\int_{t_k}^{t_{k+5}} f(x) dx = \frac{5\Delta t}{288} (19f_k + 75f_{k+1} + 50f_{k+2} + 50f_{k+3} + 75f_{k+4} + 19f_{k+5}) \quad (\text{A.28})$$

with the shorthand notation  $f_k = f(x_k)$  and  $t_{k+i} = t_k + i\Delta t$ .

## A.2.2 Gaussian Quadrature

In contrast to the Newton–Cotes method, in the Gaussian quadrature rule the accuracy can be improved by choosing the nodes wisely, where they can be located arbitrary in the integration range. Therefore with  $n + 1$  nodes,  $x_i$ , polynomials up to the order of  $2n + 1$  can be integrated exactly. The integral of a function,  $f$ , in the limits  $[a, b]$  is given by

$$\int_a^b f(x) dx \approx \frac{b-a}{2} \sum_{i=1}^n w_i f\left(\frac{b-a}{2}x_i + \frac{a+b}{2}\right) \quad (\text{A.29})$$

with the weights  $w_i$ . The nodes,  $x_i$ , are determined by the roots of orthogonal polynomials with respect to the weighted scalar product

$$\delta_{ij} = \int_a^b P_i(x)P_j(x)w(x) dx \quad (\text{A.30})$$

with an appropriate weight function  $w$ . The weights are given by

$$w_i = \int_a^b w(x)l_{in}(x), \quad i \in \{1, \dots, n\} \quad (\text{A.31})$$

where  $l_{in}$  denotes Lagrange polynomials.

Legendre, Chebyshev, Hermite and Laguerre polynomials are commonly used. In this thesis we use Legendre polynomials, which are given by the Rodrigues formula

$$P_n(x) = \frac{1}{2^n n!} \frac{d^n}{dx^n} (x^2 - 1)^n \quad (\text{A.32})$$

and the corresponding weight function is trivial,  $w(x) = 1$ . The nodes,  $x_i$ , and weights,  $\alpha_i$ , for the fifth-order Gauß–Legendre quadrature rule are

$$x_1 = -\frac{1}{3}\sqrt{5 + 2\sqrt{\frac{10}{7}}} \quad \alpha_1 = \frac{322 - 13\sqrt{70}}{900} \quad (\text{A.33})$$

$$x_2 = -\frac{1}{3}\sqrt{5 - 2\sqrt{\frac{10}{7}}} \quad \alpha_2 = \frac{322 + 13\sqrt{70}}{900} \quad (\text{A.34})$$

$$x_3 = 0 \quad \alpha_3 = \frac{128}{225} \quad (\text{A.35})$$

$$x_4 = \frac{1}{3}\sqrt{5 - 2\sqrt{\frac{10}{7}}} \quad \alpha_4 = \frac{322 + 13\sqrt{70}}{900} \quad (\text{A.36})$$

$$x_5 = \frac{1}{3}\sqrt{5 + 2\sqrt{\frac{10}{7}}} \quad \alpha_5 = \frac{322 - 13\sqrt{70}}{900}. \quad (\text{A.37})$$

# Appendix B

## Effective Coupling

In this appendix, we want to introduce the effective coupling. Due to the resummation of the fermion bubbles to all orders, we can also write the resummed propagator in terms of an effective coupling, which is frequency dependent in Fourier space. Such calculation has been done in Ref. [121] for an ultra-cold Bose gas and in Ref. [145] for the direct (s)-channel resummation for the SIAM. In the case of spatial degrees of freedom, the effective coupling also becomes momentum dependent. We derive the effective coupling for the SIAM with zero magnetic field and equal initial occupation for the spin-up and -down propagators.

We summarise the symmetry relations for the resummed auxiliary propagator,  $G$ , and the two-fermion loop function,  $\Pi$ , for: the direct (s)-channel,

$$\begin{aligned}\Pi_{11}(t, t') &= \Pi_{22}(t, t'), & \Pi_{12}(t, t') &= \Pi_{21}(t, t') = 0, \\ G_{21}(t, t') &= G_{12}(t, t'), & G_{11}(t, t') &= G_{22}(t, t');\end{aligned}\tag{B.1}$$

particle-particle (t)-channel,

$$\begin{aligned}\Pi_{12}(t, t') &= \Pi_{21}(t, t'), & \Pi_{11}(t, t') &= \Pi_{22}(t, t') = 0, \\ G_{12}(t, t') &= G_{21}(t, t'), & G_{11}(t, t') &= G_{22}(t, t') = 0;\end{aligned}\tag{B.2}$$

and the particle-hole (u)-channel,

$$\begin{aligned}\Pi_{12}(t, t') &= \Pi_{21}(t', t), & \Pi_{11}(t, t') &= \Pi_{22}(t, t') = 0, \\ G_{12}(t, t') &= G_{21}(t', t), & G_{11}(t, t') &= G_{22}(t, t') = 0.\end{aligned}\tag{B.3}$$

We define the effective coupling,  $U_{\text{eff}}$ , in Fourier space as

$$UA_{\xi}^{\text{F}}(\omega) = -\Pi_{\xi}^{\text{F}}(\omega)U_{\text{eff},\xi}(\omega), \quad UA_{\xi}^{\text{P}}(\omega) = -\Pi_{\xi}^{\text{P}}(\omega)U_{\text{eff},\xi}(\omega)\tag{B.4}$$

with  $\xi = \text{s, t, u}$  and see Eqs. (B.10), (B.21), and (B.27) for the exact definitions of  $A_{\xi}$  and  $\Pi_{\xi}$ . On the left-hand side of Eq. (B.4) is the sum of the spin bubbles to all orders and on the right-hand side, one bubble is pulled out and the rest are shifted to the effective coupling, which is then frequency dependent in Fourier domain.

At late times, when the system overcomes the transient dynamics and reaches the stationary state, all two-point functions depend only on the difference of the time coordinates. In this case, we can use the decomposition of the convolution of two

correlation functions in the statistical, spectral, retarded and advanced parts along the Keldysh contour,  $\mathcal{C}$ , where the initial time is pushed to minus infinity,  $t_0 = -\infty$ ,

$$\begin{aligned} i(X * Y)^F &= X^R * Y^F - X^F * Y^A, \\ i(X * Y)^\rho &= X^R * Y^\rho - X^\rho * Y^A, \\ i(X * Y)^R &= X^R * Y^R, \\ i(X * Y)^A &= -X^A * Y^A, \end{aligned} \quad (\text{B.5})$$

where on the left-hand side a convolution along the Keldysh contour is implied and on the right-hand side, an ordinary time convolution. The retarded and advanced functions are defined as

$$\begin{aligned} \Pi^R(t, t') &= \theta(t - t')\Pi^\rho(t, t'), \\ \Pi^A(t, t') &= \theta(t' - t)\Pi^\rho(t, t'). \end{aligned} \quad (\text{B.6})$$

For late times, when  $\Pi^R$  and  $\Pi^A$  only depend on the difference of the times,  $\tau = t - t'$ , we can use the Fourier transform

$$\begin{aligned} \Pi^R(\omega) &= \int_{-\infty}^{\infty} d\tau e^{i\omega\tau} \theta(\tau)\Pi^\rho(\tau), \\ \Pi^A(\omega) &= \int_{-\infty}^{\infty} d\tau e^{i\omega\tau} \theta(-\tau)\Pi^\rho(\tau). \end{aligned} \quad (\text{B.7})$$

The spectral part of the two-fermion loop has the same symmetry as the full propagator,

$$\Pi^\rho(t, t') = -\Pi^{\rho*}(t', t), \quad (\text{B.8})$$

and with that follows the relation between the two functions in Eq. (B.7),

$$\Pi^{R*}(\omega) = \int_{-\infty}^{\infty} d\tau e^{-i\omega\tau} \theta(\tau)\Pi^{\rho*}(\tau) = - \int_{-\infty}^{\infty} d\tau e^{i\omega\tau} \theta(-\tau)\Pi^\rho(\tau) = -\Pi^A(\omega). \quad (\text{B.9})$$

Now, we have all the ingredients we need to derive an expression for the effective couplings in terms of  $\Pi^R$  or  $\Pi^A$  in Fourier space for the three non-perturbative resummation channels.

## B.1 Direct (s)-Channel

With the symmetries given in Eq. (B.1), we define

$$A(t, t') = U^{-1}G_{11}(t, t'), \quad B(t, t') = U^{-1}G_{21}(t, t'), \quad \Pi(t, t') = U\Pi_{11}(t, t') \quad (\text{B.10})$$

and can rewrite Eq. (4.56) as

$$\begin{aligned} A &= i\Pi * B - \Pi, \\ B &= i\Pi * A \end{aligned} \quad (\text{B.11})$$

with suppressed arguments. With the help of Eq. (B.5), we write down the statistical and advanced part of  $A$ ,

$$\begin{aligned} A^F &= \Pi^R B^F - \Pi^F B^A - \Pi^F, \\ A^A &= -\Pi^A B^A - \Pi^A \end{aligned} \quad (\text{B.12})$$

and also of  $B$ ,

$$\begin{aligned} B^F &= \Pi^R A^F - \Pi^F A^A, \\ B^A &= -\Pi^A A^A. \end{aligned} \quad (\text{B.13})$$

We insert Eq. (B.13) into the first line of Eq. (B.12), which yields

$$A^F = \Pi^R \Pi^R A^F - \Pi^R \Pi^F A^A + \Pi^F \Pi^A A^A - \Pi^F \quad (\text{B.14})$$

and isolate  $A^F$ , so that

$$A^F = \frac{A^A(\Pi^A - \Pi^R)\Pi^F}{1 - \Pi^R \Pi^R} - \frac{\Pi^F}{1 - \Pi^R \Pi^R}. \quad (\text{B.15})$$

Putting both equations together, it reads

$$A^A = \Pi^A \Pi^A A^A - \Pi^A. \quad (\text{B.16})$$

Now isolating  $A^A$ ,

$$A^A = \frac{\Pi^A}{\Pi^A \Pi^A - 1}, \quad (\text{B.17})$$

and substituting this into Eq. (B.15), gives

$$A^F = \frac{\Pi^A \Pi^A - \Pi^R \Pi^A}{(1 - \Pi^R \Pi^R)(\Pi^A \Pi^A - 1)} \Pi^F - \frac{\Pi^F}{1 - \Pi^R \Pi^R}. \quad (\text{B.18})$$

Substituting Eq. (B.18) into Eq. (B.4) yields

$$\frac{U_{\text{eff}}}{U} = \frac{1 - \Pi^R \Pi^A}{(\Pi^R \Pi^R - 1)(\Pi^A \Pi^A - 1)}. \quad (\text{B.19})$$

With the relation in Eq. (B.9), it follows that

$$\frac{U_{\text{eff}}}{U} = \frac{1 + |\Pi^R|^2}{|1 - \Pi^R \Pi^R|^2}. \quad (\text{B.20})$$

## B.2 Particle-Particle (t)-Channel

With the symmetries given in Eq. (B.2), we define

$$A(t, t') = U^{-1} G_{12}(t, t'), \quad \Pi(t, t') = U \Pi_{12}(t, t') \quad (\text{B.21})$$

and can rewrite Eq. (4.68) as

$$A = i\Pi * A - \Pi. \quad (\text{B.22})$$

We use Eq. (B.5) to decompose  $A$  into statistical and advanced parts, such that

$$\begin{aligned} A^{\text{F}} &= \Pi^{\text{R}} A^{\text{F}} - \Pi^{\text{F}} A^{\text{A}} - \Pi^{\text{F}}, \\ A^{\text{A}} &= -\Pi^{\text{A}} A^{\text{A}} - \Pi^{\text{A}}. \end{aligned} \quad (\text{B.23})$$

Next, we isolate  $A^{\text{F}}$ ,

$$A^{\text{F}} = -\frac{\Pi^{\text{F}}(1 + A^{\text{A}})}{1 - \Pi^{\text{R}}}, \quad (\text{B.24})$$

and  $A^{\text{A}}$ ,

$$A^{\text{A}} = -\frac{\Pi^{\text{A}}}{1 + \Pi^{\text{A}}}, \quad (\text{B.25})$$

insert this into Eq. (B.4), which yields

$$\frac{U_{\text{eff}}}{U} = \frac{1}{|1 - \Pi^{\text{R}}|^2}. \quad (\text{B.26})$$

### B.3 Particle-Hole (u)-Channel

With the symmetries given in Eq. (B.3), we define

$$A(t, t') = U^{-1} G_{12}(t, t'), \quad \Pi(t, t') = U \Pi_{12}(t, t') \quad (\text{B.27})$$

and can rewrite Eq. (4.80) as

$$A = i\Pi * A - \Pi. \quad (\text{B.28})$$

Since the recursion equation is the same as in the particle-particle (t)-channel, the calculation is exactly the same and therefore we arrive at the effective coupling

$$\frac{U_{\text{eff}}}{U} = \frac{1}{|1 - \Pi^{\text{R}}|^2}. \quad (\text{B.29})$$

To close, we shall comment on the effective couplings in the three different channels. In contrast to the particle-particle (t)- and particle-hole (u)-channels, where all numbers of fermion bubbles appear in the resummed auxiliary propagator, in the direct (s)-channel, only odd numbers of fermion bubbles occur because of alternating spin bubbles and differing effective couplings. The general form of the effective couplings in the particle-particle (t)-, Eq. (B.26), and particle-hole (u)-channel Eq. (B.29), are the same but the difference comes from the two-fermion bubble,  $\Pi^{\text{R}}$ .

# Appendix C

## Energy Conservation of an Isolated Quantum Dot

In this chapter, we shall calculate the energy of an isolated quantum dot, which means without a coupling to the leads,  $\tau = 0$ . In this case, no electrons can tunnel to or off the dot and therefore the occupation number and energy of the quantum dot is conserved. It is then a closed system. The 2PI effective action fulfils conservation laws for the energy, particle number and momentum for closed systems for any approximation. In Ref. [126], calculations for these conserved quantities were done for an  $\mathcal{N}$ -fold one-dimensional Fermi gas.

In Ch. 4, the most general form of the 2PI effective action was

$$\Gamma[D, G, \bar{\chi}] = -i \text{Tr} [\ln D^{-1} + D_0^{-1} D] + \frac{i}{2} \text{Tr} [\ln G^{-1} + G_0^{-1} G] + \Gamma_2[D, G] + \Gamma[\bar{\chi}]. \quad (\text{C.1})$$

To this effective action, we apply the continuous time transformation

$$t \rightarrow t + \epsilon(t), \quad (\text{C.2})$$

which vanishes on the boundary, and where  $\epsilon$  is a time-dependent infinitesimal time-translation function. The two-point Green's functions and the one-point function transforms to leading order in  $\epsilon$  are

$$\begin{aligned} \delta D(t, t') &= \epsilon(t) \partial_t D(t, t') + \epsilon(t') \partial_{t'} D(t, t'), \\ \delta G(t, t') &= \epsilon(t) \partial_t G(t, t') + \epsilon(t') \partial_{t'} G(t, t'), \\ \delta \bar{\chi}(t) &= \epsilon(t) \partial_t \bar{\chi}(t). \end{aligned} \quad (\text{C.3})$$

With that, it follows for the variation of the 2PI effective action is

$$\Gamma[D, G, \bar{\chi}] \rightarrow \Gamma[D, G, \bar{\chi}] + \delta\Gamma[D, G, \bar{\chi}] \quad \text{with} \quad \delta\Gamma = \int dt E \partial_t \epsilon(t), \quad (\text{C.4})$$

where  $E$  denotes the energy which is obtained by integrating the Noether current by parts. In general, for a model with spatial dimensions, we could have applied a more general transformation  $x^\mu \rightarrow x^\mu + \epsilon^\mu(x)$ , where  $x$  is a space-time vector. This transforms not only the time- also the space-dimensions, which implies momentum

conservation. In this case, instead of the energy,  $E$ , the energy-momentum tensor,  $T^{\mu\nu}$ , appears. Then the energy is  $E = T^{00}$ .

We begin the calculation with the one-loop part of the 2PI effective action because this term is independent of the approximation. It was shown in Ref. [126] that the first term vanishes,

$$\delta \text{Tr} [\ln D^{-1}] = \delta \text{Tr} [\ln G^{-1}] = 0, \quad (\text{C.5})$$

and we apply the transformation in Eq. (C.3) to the second term,

$$\begin{aligned} \delta \text{Tr} [G_0^{-1}G] &= \int_{\mathcal{C}} dt dt' \text{Tr} \left[ G_0^{-1}(t, t') \left( \epsilon(t) \partial_t G(t, t') + \epsilon(t') \partial_{t'} G(t, t') \right) \right] \\ &= - \int_{\mathcal{C}} dt dt' \text{Tr} \left[ G_0^{-1}(t, t') \left( G(t, t') \partial_t \epsilon(t) + G(t, t') \partial_{t'} \epsilon(t') \right) \right]. \end{aligned} \quad (\text{C.6})$$

In the last step, we integrated by parts, then in each term the derivative acts on two functions. Then, we can use the fact that the inverse free propagator,  $G_0^{-1}$ , only depends on the difference of the times by changing the variable in the derivative, which gives an additional minus sign and two terms cancel.

Due to the delta function in the free inverse propagator, we can easily perform one integration and then trace over the  $2 \times 2$  matrices. We obtain

$$\delta \text{Tr} [G_0^{-1}G] = \frac{2i}{U} \int_{\mathcal{C}} dt \left( G_{12}(t, t) + G_{21}(t, t) \right) \partial_t \epsilon(t). \quad (\text{C.7})$$

Similarly, we get for the fermionic term

$$\delta \text{Tr} [D_0^{-1}D] = i \sum_{\sigma} E_{0\sigma} n_{\sigma}(t). \quad (\text{C.8})$$

For the 2PI part of the effective action contribution to the energy, we use the knowledge from classical field theory in Ref. [213],

$$T_{\mu\nu}(x) = \frac{2}{\sqrt{-g(x)}} \frac{\delta \Gamma_2[D, G, g^{\mu\nu}]}{\delta g^{\mu\nu}(x)}, \quad (\text{C.9})$$

where  $g^{\mu\nu}$  denotes the space-time metric and  $g$  is the determinant of the metric. The metric enters the  $\Gamma_2$  by scaling each interaction vertex with  $\sqrt{-g(x)}$ . The derivative of this with respect to the metric is

$$\frac{\delta \sqrt{-g(x)}}{\delta g^{\mu\nu}(y)} = -\frac{1}{2} \sqrt{-g(x)} g_{\mu\nu}(x) \delta(x - y). \quad (\text{C.10})$$

From Ref. [110], we can also use a shorter but equivalent prescription,

$$T^{\mu\nu}(x) = g^{\mu\nu} \left. \frac{\delta \Gamma_2}{\delta \xi(x)} \right|_{\xi=1}, \quad (\text{C.11})$$

where we then scale each vertex with  $\xi$  in lieu of  $g^{\mu\nu}$ . In our case, the energy momentum tensor,  $T^{\mu\nu}$ , is just the energy,  $E$ , and the space-time vector,  $x$ , with time  $t$ .



## C.1 Mean Field

We have already calculated the energy contribution from the one-loop part of the effective action. Thus, the energy contribution from the double-bubble diagram in the 2PI part of the effective action now needs to be calculated. We obtain

$$\begin{aligned} E_{\Gamma_2}^{\text{MF}}(t) &= \frac{\delta}{\delta\xi(t)} \left( -U \int_{\mathcal{C}} dx \xi(t) D_{\uparrow}(x, x) D_{\downarrow}(x, x) \right) \Big|_{\xi=1} \\ &= U D_{\uparrow}(t, t) D_{\downarrow}(t, t) \\ &= U n_{\uparrow}(t) n_{\downarrow}(t). \end{aligned} \quad (\text{C.12})$$

In the last step, we used the relation in the second line of Eq. (4.12). Putting this together with Eq. (C.8), we obtain the total energy of the quantum dot at mean-field approximation,

$$E^{\text{MF}}(t) = \sum_{\sigma} E_{0\sigma} n_{\sigma}(t) + U n_{\uparrow}(t) n_{\downarrow}(t). \quad (\text{C.13})$$

## C.2 Second Order

Only the energy contribution from the basketball diagram is unknown at this stage, which is

$$\begin{aligned} E_{\Gamma_2}^{\text{2nd}}(t) &= \frac{\delta}{\delta\xi(t)} \frac{i}{2} U^2 \int_{\mathcal{C}} dx \xi(x) \int_{\mathcal{C}} dy \xi(y) D_{\uparrow}(x, y) D_{\uparrow}(y, x) D_{\downarrow}(x, y) D_{\downarrow}(y, x) \Big|_{\xi=1} \\ &= -iU^2 \int_{\mathcal{C}} dx D_{\uparrow}(x, t) D_{\uparrow}(t, x) D_{\downarrow}(x, t) D_{\downarrow}(t, x). \end{aligned} \quad (\text{C.14})$$

The aim is to write the energy contribution in terms of the statistical propagators,  $F_{\sigma}$ , and spectral functions,  $\rho_{\sigma}$ . Obviously, the term without a sign function does not contribute because it vanishes along the Keldysh contour. Moreover, terms with two or four sign functions also vanish because of the same time arguments<sup>1</sup>. Therefore, only terms with one or three sign functions contribute to the total energy. This fulfils the spectral part of the four full fermion propagators,  $D$ . In the first step, we introduce  $B_{\sigma}(x, t) = D(x, t)D(t, x)$  and decompose this into its statistical and spectral components. We obtain

$$\begin{aligned} B_{\sigma}^{\text{F}}(x, t) &= D(x, t)D(t, x) \Big|^{\text{F}} = |F_{\sigma}|^2(x, t) - \frac{1}{4} |\rho_{\sigma}|^2(x, t) \\ B_{\sigma}^{\rho}(x, t) &= D(x, t)D(t, x) \Big|^{\rho} = \rho_{\sigma}(x, t) F_{\sigma}^*(x, t) + \rho_{\sigma}^*(x, t) F_{\sigma}(x, t), \end{aligned} \quad (\text{C.15})$$

and using this, we can easily write down the spectral part of the four full fermion propagators,  $D$ , as

$$B_{\sigma}(x, t) B_{\bar{\sigma}}(x, t) \Big|^{\rho} = B_{\sigma}^{\rho}(x, t) B_{\bar{\sigma}}^{\text{F}}(x, t) + B_{\sigma}^{\text{F}}(x, t) B_{\bar{\sigma}}^{\rho}(x, t). \quad (\text{C.16})$$

<sup>1</sup>From  $\text{sgn}(x-t)\text{sgn}(x-t) = 1$  and  $\text{sgn}(x-t)\text{sgn}(t-x) = -1$ , the argument becomes clear.

We put this into Eq. (C.14) and get

$$E_{\Gamma_2}^{2\text{nd}}(t) = -\frac{U^2}{2} \int_0^t dx \left( B_\sigma^{\text{F}}(x, t) B_\sigma^\rho(x, t) + B_\sigma^\rho(x, t) B_\sigma^{\text{F}}(x, t) \right). \quad (\text{C.17})$$

The total energy at second order reads

$$\begin{aligned} E^{2\text{nd}}(t) &= \sum_\sigma E_{0\sigma} n_\sigma(t) + U n_\uparrow(t) n_\downarrow(t) \\ &\quad - \frac{U^2}{2} \sum_\sigma \int_0^t dt' \left( |F_\sigma|^2(t', t) - \frac{1}{4} |\rho_\sigma|^2(t', t) \right) 2\Re \left( \rho_{\bar{\sigma}}(t', t) F_\sigma^*(x, t) \right), \end{aligned} \quad (\text{C.18})$$

where the last term gives a loop correction to the energy.

### C.3 Direct (s)-Channel

Besides the leading-order resummation diagram, there is an additional term coming from the expectation values of the bosonic fields. The variation of that term is

$$\begin{aligned} \delta\Gamma[\bar{\chi}] &= \frac{1}{U} \delta \int_{\mathcal{C}} dt \bar{\chi}_1 \bar{\chi}_2 = \frac{1}{U} \int_{\mathcal{C}} dt \bar{\chi}_2 \epsilon(t) \partial_t \bar{\chi}_1 + \frac{1}{U} \int_{\mathcal{C}} dt \bar{\chi}_1 \epsilon(t) \partial_t \bar{\chi}_2 \\ &= -\frac{1}{U} \int_{\mathcal{C}} \bar{\chi}_1 \bar{\chi}_2 \partial_t \epsilon(t). \end{aligned} \quad (\text{C.19})$$

In the last step, we integrated one term by parts but we have to bear in mind that the derivative then acts on the other two terms. Therefore, we have in total three terms and two of them cancel each other. The energy contribution of this term reads

$$E_{\bar{\chi}}(t) = U n_\uparrow(t) n_\downarrow(t), \quad (\text{C.20})$$

which is exactly the mean-field result.

From the leading-order resummation Feynman diagram, we derive

$$\begin{aligned} E_{\Gamma_2}^{\text{s}}(t) &= \frac{\delta}{\delta\xi(t)} \frac{i}{2} \sum_\sigma \int_{\mathcal{C}} \xi(x) dx \int_{\mathcal{C}} \xi(y) dy D_\sigma(x, y) D_\sigma(y, x) G_{\sigma\sigma}(x, y) \Big|_{\xi=1} \\ &= i \sum_\sigma \int_{\mathcal{C}} dx D_\sigma(x, t) D_\sigma(t, x) G_{\sigma\sigma}(x, t). \end{aligned} \quad (\text{C.21})$$

Taking the derivative with respect to the metric gives two terms but due to the symmetry of the auxiliary bosonic propagator,  $G$ , both terms can be summed up, which results in the second line. Using the same argument as above, we can argue that only the spectral part of the integrand contributes to the energy. It reads

$$\begin{aligned} D_\sigma(x, t) D_\sigma(t, x) G_{\sigma\sigma}(x, t) \Big|^p &= \left( \rho_\sigma(x, t) F_\sigma^*(x, t) + \rho_\sigma^*(x, t) F_\sigma(x, t) \right) G_{\sigma\sigma}^{\text{F}}(x, t) \\ &\quad + \left( |F_\sigma|^2(x, t) - \frac{1}{4} |\rho_\sigma|^2(x, t) \right) G_{\sigma\sigma}^\rho(x, t). \end{aligned} \quad (\text{C.22})$$

With this, we have the full expression for the energy of an isolated quantum dot in the direct channel,

$$\begin{aligned}
 E^s(t) &= \sum_{\sigma} E_{0\sigma} n_{\sigma}(t) + U n_{\sigma}(t) n_{\bar{\sigma}}(t) - \frac{1}{U} \sum_{\sigma} G_{\sigma\bar{\sigma}}(t, t) \\
 &\quad - \sum_{\sigma} \int_0^t dz \left[ 2\Re \left( \rho_{\sigma}^*(t, z) F_{\sigma}(t, z) \right) G_{\sigma\sigma}^F(t, z) \right. \\
 &\quad \left. + \left( |F_{\sigma}|^2(t, z) - \frac{1}{4} |\rho_{\sigma}|^2(t, z) \right) G_{\sigma\sigma}^{\rho}(t, z) \right]. \tag{C.23}
 \end{aligned}$$

## C.4 Particle-Particle (t)-Channel

The energy contribution from the leading-order resummation Feynman diagram reads

$$\begin{aligned}
 E_{\Gamma_2}^t(t) &= \frac{\delta}{\delta \xi(t)} \frac{i}{2} \sum_{\sigma} \int_{\mathcal{C}} \xi(x) dx \int_{\mathcal{C}} \xi(y) dy D_{\sigma}(x, y) D_{\bar{\sigma}}(x, y) G_{\sigma\bar{\sigma}}(y, x) \Big|_{\xi=1} \\
 &= \frac{i}{2} \sum_{\sigma} \int_{\mathcal{C}} dx \left( D_{\sigma}(t, x) D_{\bar{\sigma}}(t, x) G_{\sigma\bar{\sigma}}(x, t) \right. \\
 &\quad \left. + D_{\sigma}(x, t) D_{\bar{\sigma}}(x, t) G_{\sigma\bar{\sigma}}(t, x) \right). \tag{C.24}
 \end{aligned}$$

As before, only the spectral part is non-vanishing along the Keldysh contour. The spectral part of the first term of the integrand is given by

$$\begin{aligned}
 D_{\sigma}(t, x) D_{\bar{\sigma}}(t, x) G_{\sigma\bar{\sigma}}(x, t) \Big|_{\xi=1} &= \left( \rho_{\sigma}(t, x) F_{\bar{\sigma}}(t, x) + F_{\sigma}(t, x) \rho_{\bar{\sigma}}(t, x) \right) G_{\sigma\bar{\sigma}}^F(x, t) \\
 &\quad + \left( F_{\sigma}(t, x) F_{\bar{\sigma}}(t, x) - \frac{1}{4} \rho_{\sigma}(t, x) \rho_{\bar{\sigma}}(t, x) \right) G_{\sigma\bar{\sigma}}^{\rho}(x, t). \tag{C.25}
 \end{aligned}$$

For the second term we get the same result but with interchanged time arguments. The order of the time arguments can be changed with a complex conjugation, which gives a minus sign because of terms including one or three spectral functions and another because of the sign function in front. Summing both up, we get twice the real part of Eq. (C.25).

The total energy of an isolated quantum dot in the particle-particle (t)-channel reads

$$\begin{aligned}
 E^t(t) &= \sum_{\sigma} E_{0\sigma} n_{\sigma}(t) + U n_{\sigma}(t) n_{\bar{\sigma}}(t) - \frac{1}{U} \sum_{\sigma} G_{\sigma\bar{\sigma}}(t, t) \\
 &\quad - \sum_{\sigma} \Re \left\{ \int_0^t dz \left[ 2\rho_{\sigma}(t, z) F_{\bar{\sigma}}(t, z) G_{\sigma\bar{\sigma}}^F(t, z) \right. \right. \\
 &\quad \left. \left. + \left( F_{\sigma}(t, z) F_{\bar{\sigma}}(t, z) - \frac{1}{4} \rho_{\sigma}(t, z) \rho_{\bar{\sigma}}(t, z) \right) G_{\sigma\bar{\sigma}}^{\rho}(t, z) \right] \right\}. \tag{C.26}
 \end{aligned}$$

## C.5 Particle-Hole (u)-Channel

Similar to the particle-particle (t)-channel, we obtain from the leading-order resummation Feynman diagram

$$\begin{aligned}
 E_{\Gamma_2}^u(t) &= \frac{\delta}{\delta\xi(t)} \frac{i}{2} \sum_{\sigma} \int_{\mathcal{C}} \xi(x) dx \int_{\mathcal{C}} \xi(y) dy D_{\sigma}(x, y) D_{\bar{\sigma}}(y, x) G_{\sigma\bar{\sigma}}(x, y) \Big|_{\xi=1} \\
 &= \frac{i}{2} \sum_{\sigma} \int_{\mathcal{C}} dx \left( D_{\sigma}(t, x) D_{\bar{\sigma}}(x, t) G_{\sigma\bar{\sigma}}(t, x) \right. \\
 &\quad \left. + D_{\sigma}(x, t) D_{\bar{\sigma}}(t, x) G_{\sigma\bar{\sigma}}(x, t) \right). \tag{C.27}
 \end{aligned}$$

The spectral component of the first term reads

$$\begin{aligned}
 D_{\sigma}(t, x) D_{\bar{\sigma}}(x, t) G_{\sigma\bar{\sigma}}(t, x) \Big|^{\rho} &= \left( \rho_{\sigma}(t, x) F_{\bar{\sigma}}(x, t) + F_{\sigma}(t, x) \rho_{\bar{\sigma}}(x, t) \right) G_{\sigma\bar{\sigma}}^{\text{F}}(t, x) \\
 &\quad + \left( F_{\sigma}(t, x) F_{\bar{\sigma}}(x, t) - \frac{1}{4} \rho_{\sigma}(t, x) \rho_{\bar{\sigma}}(x, t) \right) G_{\sigma\bar{\sigma}}^{\rho}(t, x). \tag{C.28}
 \end{aligned}$$

Analogously to the particle-particle (t)-channel, we can sum up both terms in Eq. (C.27) by using the symmetry relations. Therefore, the total energy is given by

$$\begin{aligned}
 E^u(t) &= \sum_{\sigma} E_{0\sigma} n_{\sigma}(t) + U n_{\downarrow} n_{\uparrow} - \frac{1}{U} \sum_{\sigma} G_{\sigma\bar{\sigma}}(t, t) \\
 &\quad - \sum_{\sigma} \Re \left\{ \int_0^t dz \left[ \left( \rho_{\sigma}(t, z) F_{\bar{\sigma}}^*(t, z) + F_{\sigma}(t, z) \rho_{\bar{\sigma}}^*(t, z) \right) G_{\sigma\bar{\sigma}}^{\text{F}}(t, z) \right. \right. \\
 &\quad \left. \left. + \left( F_{\sigma}(t, z) F_{\bar{\sigma}}^*(t, z) - \frac{1}{4} \rho_{\sigma}(t, z) \rho_{\bar{\sigma}}^*(t, z) \right) G_{\sigma\bar{\sigma}}^{\rho}(t, z) \right] \right\}. \tag{C.29}
 \end{aligned}$$

# Bibliography

- [1] R. D. Schaller and V. I. Klimov, High efficiency carrier multiplication in PbSe nanocrystals: Implications for solar energy conversion, *Phys. Rev. Lett.* **92**, 186601 (2004).
- [2] A. H. Ip, S. M. Thon, S. Hoogland, O. Voznyy, D. Zhitomirsky, R. Debnath, L. Levina, L. R. Rollny, G. H. Carey, A. Fischer, K. W. Kemp, I. J. Kramer, Z. Ning, A. J. Labelle, K. W. Chou, A. Amassian, and E. H. Sargent, Hybrid passivated colloidal quantum dot solids, *Nat. Nanotechnol.* **7**, 577 (2012).
- [3] C.-H. M. Chuang, P. R. Brown, V. Bulović, and M. G. Bawendi, Improved performance and stability in quantum dot solar cells through band alignment engineering, *Nat. Mater.* **13**, 796 (2014).
- [4] N. Kirstaedter, N. N. Ledentsov, M. Grundmann, D. Bimberg, V. M. Ustinov, S. S. Ruvimov, M. V. Maximov, P. S. Kop'ev, Z. I. Alferov, P. Werner, U. Gösele, and J. Heydenreich, Low threshold, large  $T_o$  injection laser emission from (InGa)As quantum dots, *Electron. Lett.* **30**, 1416 (1994).
- [5] T. Yoshie, A. Scherer, J. Hendrickson, G. Khitrova, H. M. Gibbs, G. Rupper, C. Ell, O. B. Shchekin, and D. G. Deppe, Vacuum Rabi splitting with a single quantum dot in a photonic crystal nanocavity, *Nature* **432**, 200 (2004).
- [6] N. N. Ledentsov, Quantum dot laser, *Semicond. Sci. Technol.* **26**, 014001 (2011).
- [7] T.-H. Kim, K.-S. Cho, E. K. Lee, S. J. Lee, J. Chae, J. W. Kim, D. H. Kim, J.-Y. Kwon, G. Amaratunga, S. Y. Lee, B. L. Choi, Y. Kuk, J. M. Kim, and K. Kim, Full-colour quantum dot displays fabricated by transfer printing, *Nat. Photon.* **5**, 176 (2011).
- [8] C.-Y. Zhang, H.-C. Yeh, M. T. Kuroki, and T.-H. Wang, Single-quantum-dot-based DNA nanosensor, *Nat. Mater.* **4**, 826 (2005).
- [9] M.-K. So, C. Xu, A. M. Loening, S. S. Gambhir, and J. Rao, Self-illuminating quantum dot conjugates for in vivo imaging, *Nat. Biotech.* **24**, 339 (2006).
- [10] M. Atatüre, J. Dreiser, A. Badolato, A. Högele, K. Karrai, and A. Imamoglu, Quantum-dot spin-state preparation with near-unity fidelity, *Science* **312**, 551 (2006).

## Bibliography

- [11] H. Kamada, H. Gotoh, J. Temmyo, T. Takagahara, and H. Ando, Exciton Rabi oscillation in a single quantum dot, *Phys. Rev. Lett.* **87**, 246401 (2001).
- [12] X. Li, Y. Wu, D. Steel, D. Gammon, T. H. Stievater, D. S. Katzer, D. Park, C. Piermarocchi, and L. J. Sham, An all-optical quantum gate in a semiconductor quantum dot, *Science* **301**, 809 (2003).
- [13] M. Kroutvar, Y. Ducommun, D. Heiss, M. Bichler, D. Schuh, G. Abstreiter, and J. J. Finley, Optically programmable electron spin memory using semiconductor quantum dots, *Nature* **432**, 81 (2004).
- [14] D. Press, T. D. Ladd, B. Zhang, and Y. Yamamoto, Complete quantum control of a single quantum dot spin using ultrafast optical pulses, *Nature* **456**, 218 (2008).
- [15] A. Zrenner, E. Beham, S. Stuffer, F. Findeis, M. Bichler, and G. Abstreiter, Coherent properties of a two-level system based on a quantum-dot photodiode, *Nature* **418**, 612 (2002).
- [16] J. M. Elzerman, R. Hanson, L. H. Willems van Beveren, B. Witkamp, L. M. K. Vandersypen, and L. P. Kouwenhoven, Single-shot read-out of an individual electron spin in a quantum dot, *Nature* **430**, 431 (2004).
- [17] R. Hanson, L. H. W. van Beveren, I. T. Vink, J. M. Elzerman, W. J. M. Naber, F. H. L. Koppens, L. P. Kouwenhoven, and L. M. K. Vandersypen, Single-shot readout of electron spin states in a quantum dot using spin-dependent tunnel rates, *Phys. Rev. Lett.* **94**, 196802 (2005).
- [18] D. P. DiVincenzo, Quantum computation, *Science* **270**, 255 (1995).
- [19] A. Imamoglu, D. D. Awschalom, G. Burkard, D. P. DiVincenzo, D. Loss, M. Sherwin, and A. Small, Quantum information processing using quantum dot spins and cavity QED, *Phys. Rev. Lett.* **83**, 4204 (1999).
- [20] P. W. Anderson, Localized Magnetic States in Metals, *Phys. Rev.* **124**, 41 (1961).
- [21] D. Goldhaber-Gordon, H. Shtrikman, D. Mahalu, D. A. Magder, U. Meirav, and M. A. Kastner, Kondo effect in a single-electron transistor, *Nature* **391**, 156 (1998).
- [22] D. Goldhaber-Gordon, J. Göres, M. A. Kastner, H. Shtrikman, D. Mahalu, and U. Meirav, From the Kondo regime to the mixed-valence regime in a single-electron transistor, *Phys. Rev. Lett.* **81**, 5225 (1998).
- [23] S. M. Cronenwett, T. H. Oosterkamp, and L. P. Kouwenhoven, A tunable Kondo effect in quantum dots, *Science* **281**, 540 (1998).

- [24] V. Fateev and P. Wiegmann, The exact solution of the  $s - d$  exchange model with arbitrary impurity spin  $S$  (Kondo problem), *Phys. Lett. A* **81**, 179 (1981).
- [25] N. Kawakami and A. Okiji, Exact expression of the ground-state energy for the symmetric Anderson model, *Phys. Lett. A* **86**, 483 (1981).
- [26] A. M. Tsvelick and P. B. Wiegmann, Exact results in the theory of magnetic alloys, *Adv. Phys.* **32**, 453 (1983).
- [27] A. M. Tsvelick and P. B. Wiegmann, Exact solution of the Anderson model. II. Thermodynamic properties at finite temperatures, *J. Phys. C* **16**, 2321 (1983).
- [28] N. Andrei, K. Furuya, and J. H. Lowenstein, Solution of the Kondo problem, *Rev. Mod. Phys.* **55**, 331 (1983).
- [29] A. Komnik and A. O. Gogolin, Mean-field results on the Anderson impurity model out of equilibrium, *Phys. Rev. B* **69**, 153102 (2004).
- [30] L. Mühlbacher, D. F. Urban, and A. Komnik, Anderson impurity model in nonequilibrium: Analytical results versus quantum Monte Carlo data, *Phys. Rev. B* **83**, 075107 (2011).
- [31] A. Oguri, Fermi-liquid theory for the Anderson model out of equilibrium, *Phys. Rev. B* **64**, 153305 (2001).
- [32] B. S. Shastry, E. Perepelitsky, and A. C. Hewson, Extremely correlated Fermi liquid study of the  $U = \infty$  Anderson impurity model, *Phys. Rev. B* **88**, 205108 (2013).
- [33] G.-H. Ding and B. Dong, Finite-frequency current fluctuations and self-consistent perturbation theory for electron transport through a quantum dot, *Phys. Rev. B* **87**, 235303 (2013).
- [34] R. M. Konik, H. Saleur, and A. Ludwig, Transport in quantum dots from the integrability of the Anderson model, *Phys. Rev. B* **66**, 125304 (2002).
- [35] A. C. Hewson, Renormalized perturbation calculations for the single-impurity Anderson model, *J. Phys. Cond. Mat.* **13**, 10011 (2001).
- [36] A. C. Hewson, J. Bauer, and A. Oguri, Non-equilibrium differential conductance through a quantum dot in a magnetic field, *J. Phys. Cond. Mat.* **17**, 5413 (2005).
- [37] K. Edwards and A. C. Hewson, A new renormalization group approach for systems with strong electron correlation, *J. Phys. Cond. Mat.* **23**, 045601 (2011).

## Bibliography

- [38] K. Edwards, A. C. Hewson, and V. Pandis, Perturbational scaling theory of the induced magnetization in the impurity Anderson model, *Phys. Rev. B* **87**, 165128 (2013).
- [39] A. Rosch, J. Kroha, and P. Wölfle, Kondo effect in quantum dots at high voltage: Universality and scaling, *Phys. Rev. Lett.* **87**, 156802 (2001).
- [40] A. Rosch, J. Paaske, J. Kroha, and P. Wölfle, Nonequilibrium transport through a Kondo dot in a magnetic field: Perturbation theory and poor man's scaling, *Phys. Rev. Lett.* **90**, 076804 (2003).
- [41] A. Rosch, T. A. Costi, J. Paaske, and P. Wölfle, Spectral function of the Kondo model in high magnetic fields, *Phys. Rev. B* **68**, 014430 (2003).
- [42] A. Rosch, J. Paaske, J. Kroha, and P. Wölfle, The Kondo effect in non-equilibrium quantum dots: Perturbative renormalization group, *J. Phys. Soc. Jpn.* **74**, 118 (2005).
- [43] T. A. Costi, A. C. Hewson, and V. Zlatic, Transport coefficients of the Anderson model via the numerical renormalization group, *J. Phys. Cond. Mat.* **6**, 2519 (1994).
- [44] R. Bulla, A. C. Hewson, and T. Pruschke, Numerical renormalization group calculations for the self-energy of the impurity Anderson model, *J. Phys. Cond. Mat.* **10**, 8365 (1998).
- [45] R. Peters, T. Pruschke, and F. B. Anders, Numerical renormalization group approach to Green's functions for quantum impurity models, *Phys. Rev. B* **74**, 245114 (2006).
- [46] A. Weichselbaum and J. von Delft, Sum-rule conserving spectral functions from the numerical renormalization group, *Phys. Rev. Lett.* **99**, 076402 (2007).
- [47] R. Bulla, T. A. Costi, and T. Pruschke, Numerical renormalization group method for quantum impurity systems, *Rev. Mod. Phys.* **80**, 395 (2008).
- [48] S. Schmitt and F. B. Anders, Comparison between scattering-states numerical renormalization group and the Kadanoff–Baym–Keldysh approach to quantum transport: Crossover from weak to strong correlations, *Phys. Rev. B* **81**, 165106 (2010).
- [49] I. Weymann, Finite-temperature spintronic transport through Kondo quantum dots: Numerical renormalization group study, *Phys. Rev. B* **83**, 113306 (2011).
- [50] R. Žitko and T. Pruschke, Energy resolution and discretization artifacts in the numerical renormalization group, *Phys. Rev. B* **79**, 085106 (2009).



- [51] R. Žitko, Quantitative determination of the discretization and truncation errors in numerical renormalization-group calculations of spectral functions, *Phys. Rev. B* **84**, 085142 (2011).
- [52] Z. Osolin and R. Žitko, Padé approximant approach for obtaining finite-temperature spectral functions of quantum impurity models using the numerical renormalization group technique, *Phys. Rev. B* **87**, 245135 (2013).
- [53] K. G. Wilson, The renormalization group: Critical phenomena and the Kondo problem, *Rev. Mod. Phys.* **47**, 773 (1975).
- [54] S. Andergassen, T. Enss, and V. Meden, Kondo physics in transport through a quantum dot with Luttinger-liquid leads, *Phys. Rev. B* **73**, 153308 (2006).
- [55] L. Bartosch, H. Freire, J. J. R. Cardenas, and P. Kopietz, A functional renormalization group approach to the Anderson impurity model, *J. Phys. Cond. Mat.* **21**, 305602 (2009).
- [56] A. Isidori, D. Roosen, L. Bartosch, W. Hofstetter, and P. Kopietz, Spectral function of the Anderson impurity model at finite temperatures, *Phys. Rev. B* **81**, 235120 (2010).
- [57] P. Kopietz, L. Bartosch, L. Costa, A. Isidori, and A. Ferraz, Ward identities for the Anderson impurity model: Derivation via functional methods and the exact renormalization group, *J. Phys. A* **43**, 385004 (2010).
- [58] S. Streib, A. Isidori, and P. Kopietz, Solution of the Anderson impurity model via the functional renormalization group, *Phys. Rev. B* **87**, 201107 (2013).
- [59] R. Gezzi, T. Pruschke, and V. Meden, Functional renormalization group for nonequilibrium quantum many-body problems, *Phys. Rev. B* **75**, 045324 (2007).
- [60] S. G. Jakobs, V. Meden, and H. Schoeller, Nonequilibrium functional renormalization group for interacting quantum systems, *Phys. Rev. Lett.* **99**, 150603 (2007).
- [61] C. Karrasch, R. Hedden, R. Peters, T. Pruschke, K. Schönhammer, and V. Meden, A finite-frequency functional renormalization group approach to the single impurity Anderson model, *J. Phys. Cond. Mat.* **20**, 345205 (2008).
- [62] S. G. Jakobs, M. Pletyukhov, and H. Schoeller, Nonequilibrium functional renormalization group with frequency-dependent vertex function: A study of the single-impurity Anderson model, *Phys. Rev. B* **81**, 195109 (2010).
- [63] C. Karrasch, M. Pletyukhov, L. Borda, and V. Meden, Functional renormalization group study of the interacting resonant level model in and out of equilibrium, *Phys. Rev. B* **81**, 125122 (2010).

## Bibliography

- [64] H. Schmidt and P. Wölfle, Transport through a Kondo quantum dot: Functional RG approach, *Ann. Phys.* **19**, 60 (2010).
- [65] M. Kinza, J. Ortloff, J. Bauer, and C. Honerkamp, Alternative functional renormalization group approach to the single impurity Anderson model, *Phys. Rev. B* **87**, 035111 (2013).
- [66] V. Janiš, Stability of self-consistent solutions for the Hubbard model at intermediate and strong coupling, *Phys. Rev. B* **60**, 11345 (1999).
- [67] V. Janiš and P. Augustinský, Analytic impurity solver with Kondo strong-coupling asymptotics, *Phys. Rev. B* **75**, 165108 (2007).
- [68] V. Janiš and P. Augustinský, Kondo behavior in the asymmetric Anderson model: Analytic approach, *Phys. Rev. B* **77**, 085106 (2008).
- [69] P. Augustinský and V. Janiš, Multiorbital simplified parquet equations for strongly correlated electrons, *Phys. Rev. B* **83**, 035114 (2011).
- [70] S. Smirnov and M. Grifoni, Slave-boson Keldysh field theory for the Kondo effect in quantum dots, *Phys. Rev. B* **84**, 125303 (2011).
- [71] S. Smirnov and M. Grifoni, Kondo effect in interacting nanoscopic systems: Keldysh field integral theory, *Phys. Rev. B* **84**, 235314 (2011).
- [72] S. Smirnov and M. Grifoni, Spin-channel Keldysh field theory for weakly interacting quantum dots, *Phys. Rev. B* **85**, 195310 (2012).
- [73] S. Smirnov and M. Grifoni, Keldysh effective action theory for universal physics in spin- $\frac{1}{2}$  Kondo dots, *Phys. Rev. B* **87**, 121302 (2013).
- [74] S. Smirnov and M. Grifoni, Nonequilibrium Kondo transport through a quantum dot in a magnetic field, *New J. Phys.* **15**, 073047 (2013).
- [75] A. O. Gogolin and A. Komnik, Towards full counting statistics for the Anderson impurity model, *Phys. Rev. B* **73**, 195301 (2006).
- [76] T. L. Schmidt, A. Komnik, and A. O. Gogolin, Hanbury Brown–Twiss correlations and noise in the charge transfer statistics through a multiterminal Kondo dot, *Phys. Rev. Lett.* **98**, 056603 (2007).
- [77] M. Ganahl, P. Thunström, F. Verstraete, K. Held, and H. G. Evertz, Chebyshev expansion for impurity models using matrix product states, *Phys. Rev. B* **90**, 045144 (2014).
- [78] A. J. Daley, C. Kollath, U. Schollwöck, and G. Vidal, Time-dependent density-matrix renormalization-group using adaptive effective Hilbert spaces, *J. Stat. Mech.* **2004**, P04005 (2004).

- [79] P. Schmitteckert, Nonequilibrium electron transport using the density matrix renormalization group method, *Phys. Rev. B* **70**, 121302 (2004).
- [80] S. R. White and A. E. Feiguin, Real-time evolution using the density matrix renormalization group, *Phys. Rev. Lett.* **93**, 076401 (2004).
- [81] K. A. Al-Hassanieh, A. E. Feiguin, J. A. Riera, C. A. Büsser, and E. Dagotto, Adaptive time-dependent density-matrix renormalization-group technique for calculating the conductance of strongly correlated nanostructures, *Phys. Rev. B* **73**, 195304 (2006).
- [82] E. Boulat, H. Saleur, and P. Schmitteckert, Twofold advance in the theoretical understanding of far-from-equilibrium properties of interacting nanostructures, *Phys. Rev. Lett.* **101**, 140601 (2008).
- [83] L. G. G. V. Dias da Silva, F. Heidrich-Meisner, A. E. Feiguin, C. A. Büsser, G. B. Martins, E. V. Anda, and E. Dagotto, Transport properties and Kondo correlations in nanostructures: Time-dependent DMRG method applied to quantum dots coupled to Wilson chains, *Phys. Rev. B* **78**, 195317 (2008).
- [84] F. Heidrich-Meisner, A. E. Feiguin, and E. Dagotto, Real-time simulations of nonequilibrium transport in the single-impurity Anderson model, *Phys. Rev. B* **79**, 235336 (2009).
- [85] F. B. Anders and A. Schiller, Real-time dynamics in quantum-impurity systems: A time-dependent numerical renormalization-group approach, *Phys. Rev. Lett.* **95**, 196801 (2005).
- [86] F. B. Anders and A. Schiller, Spin precession and real-time dynamics in the Kondo model: Time-dependent numerical renormalization-group study, *Phys. Rev. B* **74**, 245113 (2006).
- [87] F. B. Anders, A numerical renormalization group approach to non-equilibrium Green functions for quantum impurity models, *J. Phys. Cond. Mat.* **20**, 195216 (2008).
- [88] F. B. Anders, Steady-state currents through nanodevices: A scattering-states numerical renormalization-group approach to open quantum systems, *Phys. Rev. Lett.* **101**, 066804 (2008).
- [89] D. Roosen, M. R. Wegewijs, and W. Hofstetter, Nonequilibrium dynamics of anisotropic large spins in the Kondo regime: Time-dependent numerical renormalization group analysis, *Phys. Rev. Lett.* **100**, 087201 (2008).
- [90] H. Schoeller and J. König, Real-time renormalization group and charge fluctuations in quantum dots, *Phys. Rev. Lett.* **84**, 3686 (2000).

## Bibliography

- [91] S. Andergassen, M. Pletyukhov, D. Schuricht, H. Schoeller, and L. Borda, Renormalization group analysis of the interacting resonant-level model at finite bias: Generic analytic study of static properties and quench dynamics, *Phys. Rev. B* **83**, 205103 (2011).
- [92] O. Kashuba and H. Schoeller, Transient dynamics of open quantum systems, *Phys. Rev. B* **87**, 201402 (2013).
- [93] L. Mühlbacher and E. Rabani, Real-time path integral approach to nonequilibrium many-body quantum systems, *Phys. Rev. Lett.* **100**, 176403 (2008).
- [94] M. Schiró and M. Fabrizio, Real-time diagrammatic Monte Carlo for nonequilibrium quantum transport, *Phys. Rev. B* **79**, 153302 (2009).
- [95] E. Gull, D. R. Reichman, and A. J. Millis, Numerically exact long-time behavior of nonequilibrium quantum impurity models, *Phys. Rev. B* **84**, 085134 (2011).
- [96] S. Weiss, J. Eckel, M. Thorwart, and R. Egger, Iterative real-time path integral approach to nonequilibrium quantum transport, *Phys. Rev. B* **77**, 195316 (2008).
- [97] S. Weiss, J. Eckel, M. Thorwart, and R. Egger, Erratum: Iterative real-time path integral approach to nonequilibrium quantum transport [*Phys. Rev. B*, 195316 (2008)], *Phys. Rev. B* **79**, 249901 (2009).
- [98] S. Weiss, R. Hütten, D. Becker, J. Eckel, R. Egger, and M. Thorwart, Iterative path integral summation for nonequilibrium quantum transport, *Phys. Status Solidi B* **250**, 2298 (2013).
- [99] N. Lanatà and H. U. R. Strand, Time-dependent and steady-state Gutzwiller approach for nonequilibrium transport in nanostructures, *Phys. Rev. B* **86**, 115310 (2012).
- [100] P. Wang, Solving real time evolution problems by constructing excitation operators, *AIP Advances* **2**, 012194 (2012).
- [101] P. Wang, The excitation operator approach to non-Markovian dynamics of quantum impurity models in the Kondo regime, *Eur. Phys. J.* **86**, 1 (2013).
- [102] D. Segal, A. J. Millis, and D. R. Reichman, Nonequilibrium transport in quantum impurity models: Exact path integral simulations, *Phys. Chem. Chem. Phys.* **13**, 14378 (2011).
- [103] J. M. Luttinger and J. C. Ward, Ground-state energy of a many-fermion system. II, *Phys. Rev.* **118**, 1417 (1960).

- [104] G. Baym, Self-consistent approximations in many-body systems, *Phys. Rev.* **127**, 1391 (1962).
- [105] J. M. Cornwall, R. Jackiw, and E. Tomboulis, Effective action for composite operators, *Phys. Rev. D* **10**, 2428 (1974).
- [106] J. Berges and J. Cox, Thermalization of quantum fields from time-reversal invariant evolution equations, *Phys. Lett. B* **517**, 369 (2001).
- [107] J. Berges, Controlled nonperturbative dynamics of quantum fields out of equilibrium, *Nucl. Phys. A* **699**, 847 (2002).
- [108] J. Berges and J. Serreau, Parametric Resonance in Quantum Field Theory, *Phys. Rev. Lett.* **91**, 111601 (2003).
- [109] F. Cooper, J. F. Dawson, and B. Mihaila, Quantum dynamics of phase transitions in broken symmetry  $\lambda\varphi^4$  field theory, *Phys. Rev. D* **67**, 056003 (2003).
- [110] A. Arrizabalaga, J. Smit, and A. Tranberg, Equilibration in  $\varphi^4$  theory in  $3+1$  dimensions, *Phys. Rev. D* **72**, 025014 (2005).
- [111] A. Giraud and J. Serreau, Decoherence and thermalization of a pure quantum state in quantum field theory, *Phys. Rev. Lett.* **104**, 230405 (2010).
- [112] G. Aarts, G. F. Bonini, and C. Wetterich, Exact and truncated dynamics in nonequilibrium field theory, *Phys. Rev. D* **63**, 025012 (2000).
- [113] G. Aarts, D. Ahrensmeier, R. Baier, J. Berges, and J. Serreau, Far-from-equilibrium dynamics with broken symmetries from the  $1/N$  expansion of the 2PI effective action, *Phys. Rev. D* **66**, 045008 (2002).
- [114] G. Aarts and J. M. Martínez Resco, Transport coefficients from the two particle irreducible effective action, *Phys. Rev. D* **68**, 085009 (2003).
- [115] G. Aarts and A. Tranberg, Nonequilibrium dynamics in the  $O(N)$  model to next-to-next-to-leading order in the  $1/N$  expansion, *Phys. Rev. D* **74**, 025004 (2006).
- [116] A. M. Rey, B. L. Hu, E. Calzetta, A. Roura, and C. W. Clark, Nonequilibrium dynamics of optical-lattice-loaded Bose–Einstein-condensate atoms: Beyond the Hartree-Fock-Bogoliubov approximation, *Phys. Rev. A* **69**, 033610 (2004).
- [117] T. Gasenzer, J. Berges, M. G. Schmidt, and M. Seco, Nonperturbative dynamical many-body theory of a Bose–Einstein condensate, *Phys. Rev. A* **72**, 063604 (2005).
- [118] K. Temme and T. Gasenzer, Nonequilibrium dynamics of condensates in a lattice with the two-particle-irreducible effective action in the  $1/\mathcal{N}$  expansion, *Phys. Rev. A* **74**, 053603 (2006).

## Bibliography

- [119] J. Berges and T. Gasenzer, Quantum versus classical statistical dynamics of an ultracold Bose gas, *Phys. Rev. A* **76**, 033604 (2007).
- [120] A. Branschädel and T. Gasenzer, 2PI nonequilibrium versus transport equations for an ultracold Bose gas, *J. Phys. B* **41**, 135302 (2008).
- [121] C. Scheppach, J. Berges, and T. Gasenzer, Matter-wave turbulence: Beyond kinetic scaling, *Phys. Rev. A* **81**, 033611 (2010).
- [122] J. Berges, S. Borsányi, and J. Serreau, Thermalization of fermionic quantum fields, *Nucl. Phys. B* **660**, 51 (2003).
- [123] J. Berges, S. Borsányi, and C. Wetterich, Prethermalization, *Phys. Rev. Lett.* **93**, 142002 (2004).
- [124] J. Berges, J. Pruschke, and A. Rothkopf, Instability-induced fermion production in quantum field theory, *Phys. Rev. D* **80**, 023522 (2009).
- [125] M. Kronenwett and T. Gasenzer, Non-thermal equilibration of a one-dimensional Fermi gas, *ArXiv:1006.3330* (2010).
- [126] M. Kronenwett and T. Gasenzer, Far-from-equilibrium dynamics of an ultracold Fermi gas, *Appl. Phys. B* **102**, 469 (2011).
- [127] M. Kronenwett, *Far-from-equilibrium dynamics of ultra-cold Fermi gases*, PhD thesis, Heidelberg University, 2011.
- [128] T. Gasenzer and J. M. Pawłowski, Towards far-from-equilibrium quantum field dynamics: A functional renormalisation-group approach, *Phys. Lett. B* **670**, 135 (2008).
- [129] T. Gasenzer, S. Keßler, and J. Pawłowski, Far-from-equilibrium quantum many-body dynamics, *Eur. Phys. J. C* **70**, 423 (2010).
- [130] L. Hedin, New method for calculating the one-particle Green's function with application to the electron-gas problem, *Phys. Rev.* **139**, A796 (1965).
- [131] L. Hedin and S. Lundqvist, Effects of electron-electron and electron-phonon interactions on the one-electron states of solids, *Solid State Phys.* **23**, 1 (1970).
- [132] K. S. Thygesen and A. Rubio, Nonequilibrium GW approach to quantum transport in nano-scale contacts, *J. Chem. Phys.* **126**, 091101 (2007).
- [133] K. S. Thygesen and A. Rubio, Conserving GW scheme for nonequilibrium quantum transport in molecular contacts, *Phys. Rev. B* **77**, 115333 (2008).
- [134] F. Aryasetiawan and S. Biermann, Generalized Hedin's equations for quantum many-body systems with spin-dependent interactions, *Phys. Rev. Lett.* **100**, 116402 (2008).

- [135] C. D. Spataru, M. S. Hybertsen, S. G. Louie, and A. J. Millis, GW approach to Anderson model out of equilibrium: Coulomb blockade and false hysteresis in the  $I$ - $V$  characteristics, *Phys. Rev. B* **79**, 155110 (2009).
- [136] C. D. Spataru, Scaling properties of the Anderson model in the Kondo regime studied by  $\sigma G\sigma W$  formalism, *Phys. Rev. B* **82**, 195111 (2010).
- [137] P. Lipavský, V. Špička, and B. Velický, Generalized Kadanoff–Baym ansatz for deriving quantum transport equations, *Phys. Rev. B* **34**, 6933 (1986).
- [138] Q. T. Vu and H. Haug, Time-dependent screening of the carrier-phonon and carrier-carrier interactions in nonequilibrium systems, *Phys. Rev. B* **62**, 7179 (2000).
- [139] A. Marini, Competition between the electronic and phonon–mediated scattering channels in the out–of–equilibrium carrier dynamics of semiconductors: An ab-initio approach, *J. Phys: Conf. Proc.* **427**, 012003 (2013).
- [140] G. Pal, Y. Pavlyukh, W. Hübner, and H. C. Schneider, Optical absorption spectra of finite systems from a conserving Bethe–Salpeter equation approach, *Eur. Phys. J. B* **79**, 327 (2011).
- [141] D. Hochstuhl and M. Bonitz, Time-dependent restricted active space configuration interaction theory applied to the photoionization of neon, *J. Phys: Conf. Proc.* **427**, 012007 (2013).
- [142] K. Balzer, S. Hermanns, and M. Bonitz, The generalized Kadanoff–Baym ansatz. Computing nonlinear response properties of finite systems, *J. Phys: Conf. Proc.* **427**, 012006 (2013).
- [143] M. Bonitz, S. Hermanns, and K. Balzer, Dynamics of Hubbard nano-clusters following strong excitation, *Contrib. Plasma Phys.* **53**, 778–787 (2013).
- [144] S. Latini, E. Perfetto, A.-M. Uimonen, R. van Leeuwen, and G. Stefanucci, Charge dynamics in molecular junctions: Nonequilibrium Green’s function approach made fast, *Phys. Rev. B* **89**, 075306 (2014).
- [145] D. Sexty, T. Gasenzer, and J. Pawłowski, Real-time effective-action approach to the Anderson quantum dot, *Phys. Rev. B* **83**, 165315 (2011).
- [146] A.-M. Uimonen, E. Khosravi, A. Stan, G. Stefanucci, S. Kurth, R. van Leeuwen, and E. K. U. Gross, Comparative study of many-body perturbation theory and time-dependent density functional theory in the out-of-equilibrium Anderson model, *Phys. Rev. B* **84**, 115103 (2011).
- [147] X. Wang, C. D. Spataru, M. S. Hybertsen, and A. J. Millis, Electronic correlation in nanoscale junctions: Comparison of the GW approximation to a numerically exact solution of the single-impurity Anderson model, *Phys. Rev. B* **77**, 045119 (2008).

## Bibliography

- [148] J. Eckel, F. Heidrich-Meisner, S. G. Jakobs, M. Thorwart, M. Pletyukhov, and R. Egger, Comparative study of theoretical methods for non-equilibrium quantum transport, *New J. Phys.* **12**, 043042 (2010).
- [149] M. Nuss, E. Arrigoni, M. Aichhorn, and W. von der Linden, Variational cluster approach to the single-impurity Anderson model, *Phys. Rev. B* **85**, 235107 (2012).
- [150] M. Nuss, M. Ganahl, H. G. Evertz, E. Arrigoni, and W. von der Linden, Steady-state and quench-dependent relaxation of a quantum dot coupled to one-dimensional leads, *Phys. Rev. B* **88**, 045132 (2013).
- [151] P. Werner, T. Oka, M. Eckstein, and A. J. Millis, Weak-coupling quantum Monte Carlo calculations on the Keldysh contour: Theory and application to the current-voltage characteristics of the Anderson model, *Phys. Rev. B* **81**, 035108 (2010).
- [152] T. L. Schmidt, P. Werner, L. Mühlbacher, and A. Komnik, Transient dynamics of the Anderson impurity model out of equilibrium, *Phys. Rev. B* **78**, 235110 (2008).
- [153] J. Berges, Far-from-equilibrium quantum fields in particle physics and cosmology, Vorlesungsskript SS 2012, 2012.
- [154] J. Berges, Introduction to nonequilibrium quantum field theory, *AIP Conf. Proc.* **739**, 3 (2005).
- [155] G. Baym and L. P. Kadanoff, Conservation laws and correlation functions, *Phys. Rev.* **124**, 287 (1961).
- [156] L. V. Keldysh, Diagram technique for nonequilibrium processes, [*Sov. Phys. JETP* **20**, 1018 (1965)] *Zh. Eksp. Teor. Fiz.* **47**, 1515 (1964).
- [157] J. Schwinger, Brownian motion of a quantum oscillator, *J. Math. Phys.* **2**, 407 (1961).
- [158] P. M. Bakshi and K. T. Mahanthappa, Expectation value formalism in quantum field theory. I, *J. Math. Phys.* **4**, 1 (1963).
- [159] P. M. Bakshi and K. T. Mahanthappa, Expectation value formalism in quantum field theory. II, *J. Math. Phys.* **4**, 12 (1963).
- [160] K. T. Mahanthappa, Multiple production of photons in quantum electrodynamics, *Phys. Rev.* **126**, 329 (1962).
- [161] P. C. Martin and J. Schwinger, Theory of many-particle systems. I, *Phys. Rev.* **115**, 1342 (1959).



- [162] R. Kubo, Statistical-mechanical theory of irreversible processes. I. General theory and simple applications to magnetic and conduction problems, *J. Phys. Soc. Jpn.* **12**, 570 (1957).
- [163] J. D. Bjorken, Applications of the chiral  $U(6) \otimes U(6)$  algebra of current densities, *Phys. Rev.* **148**, 1467 (1966).
- [164] K. Johnson and F. E. Low, Current algebras in a simple model, *Prog. Theor. Phys. Suppl.* **37**, 74 (1966).
- [165] R. P. Feynman, Space-time approach to non-relativistic quantum mechanics, *Rev. Mod. Phys.* **20**, 367 (1948).
- [166] M. E. Peskin and D. V. Schroeder, *An introduction to quantum field theory (frontiers in physics)*, Westview Press, 1995.
- [167] M. Srednicki, *Quantum field theory*, Cambridge University Press, 1 edition, 2007.
- [168] J. Berges,  $n$ -particle irreducible effective action techniques for gauge theories, *Phys. Rev. D* **70**, 105010 (2004).
- [169] R. P. Feynman, The theory of positrons, *Phys. Rev.* **76**, 749 (1949).
- [170] F. J. Dyson, The  $S$  matrix in quantum electrodynamics, *Phys. Rev.* **75**, 1736 (1949).
- [171] J. Schwinger, On the Green's functions of quantized fields. I, *Proc. Natl. Acad. Sci.* **37**, 452 (1951).
- [172] O. V. Konstantinov and V. I. Perel', A diagram technique for evaluating transport quantities, *Sov. Phys. JETP* **12**, 142 (1959).
- [173] H. B. Callen and T. A. Welton, Irreversibility and generalized noise, *Phys. Rev.* **83**, 34 (1951).
- [174] J. Nygard, D. H. Cobden, and P. E. Lindelof, Kondo physics in carbon nanotubes, *Nature* **408**, 342 (2000).
- [175] M. T. Björk, C. Thelander, A. E. Hansen, L. E. Jensen, M. W. Larsson, L. R. Wallenberg, and L. Samuelson, Few-electron quantum dots in nanowires, *Nano Lett.* **4**, 1621 (2004).
- [176] L. P. Kouwenhoven, D. G. Austing, and S. Tarucha, Few-electron quantum dots, *Rep. Prog. Phys.* **64**, 701 (2001).
- [177] N. S. Wingreen and Y. Meir, Anderson model out of equilibrium: Noncrossing-approximation approach to transport through a quantum dot, *Phys. Rev. B* **49**, 11040 (1994).

## Bibliography

- [178] W. D. Haas and G. V. D. Berg, The electrical resistance of gold and silver at low temperatures, *Physica* **3**, 440 (1936).
- [179] C. Zener, Interaction between the  $d$  shells in the transition metals, *Phys. Rev.* **81**, 440 (1951).
- [180] K. Yosida, Magnetic properties of Cu-Mn alloys, *Phys. Rev.* **106**, 893 (1957).
- [181] J. Friedel, Metallic alloys, *Il Nuovo Cimento* **7**, 287 (1958).
- [182] J. R. Schrieffer and P. A. Wolff, Relation between the Anderson and Kondo Hamiltonians, *Phys. Rev.* **149**, 491 (1966).
- [183] J. Kondo, Resistance minimum in dilute magnetic alloys, *Prog. Theor. Phys.* **32**, 37 (1964).
- [184] A. A. Abrikosov, Electron scattering on magnetic impurities in metals and anomalous resistivity effects, *Physics* **2**, 5 (1965).
- [185] H. Suhl, Dispersion theory of the Kondo effect, *Phys. Rev.* **138**, A515 (1965).
- [186] Y. Nagaoka, Self-consistent treatment of Kondo's effect in dilute alloys, *Phys. Rev.* **138**, A1112 (1965).
- [187] J. Kondo,  $s - d$  scattering at low temperatures, *Prog. Theor. Phys.* **34**, 204 (1965).
- [188] P. W. Anderson, A poor man's derivation of scaling laws for the Kondo problem, *J. Phys. C* **3**, 2436 (1970).
- [189] H. Bethe, Zur Theorie der Metalle, *Z. Phys.* **71**, 205 (1931).
- [190] P. Coleman, Heavy fermions: electrons at the edge of magnetism, in *Handbook of Magnetism and Advanced Magnetic Materials. Vol 1: Fundamentals and Theory*, edited by H. Kronmuller and S. Parkin, page 95, John Wiley and Sons, 2007.
- [191] G. C. Wick, The evaluation of the collision matrix, *Phys. Rev.* **80**, 268 (1950).
- [192] D. R. Hartree, The wave mechanics of an atom with a non-Coulomb central field, *Proc. Cambridge Phil. Soc.* **24**, 89 (1928).
- [193] V. Fock, Näherungsmethode zur Lösung des quantenmechanischen Mehrkörperproblems, *Z. Phys.* **61**, 126 (1930).
- [194] N. N. Bogoliubov, On the theory of superfluidity, *J. Phys. (USSR)* **11**, 23 (1947).
- [195] M. Born, Zur Quantenmechanik der Stoßvorgänge, *Z. Phys.* **37**, 863 (1926).

- [196] R. L. Stratonovich, On a method of calculating quantum distribution functions, *Sov. Phys. Dokl.* **2**, 416 (1957).
- [197] J. Hubbard, Calculation of partition functions, *Phys. Rev. Lett.* **3**, 77 (1959).
- [198] Y. Meir and N. S. Wingreen, Landauer formula for the current through an interacting electron region, *Phys. Rev. Lett.* **68**, 2512 (1992).
- [199] R. Landauer, Spatial variation of currents and fields due to localized scatterers in metallic conduction, *IBM J. Res. Dev.* **1**, 223 (1957).
- [200] B. J. van Wees, H. van Houten, C. W. J. Beenakker, J. G. Williamson, L. P. Kouwenhoven, D. van der Marel, and C. T. Foxon, Quantized conductance of point contacts in a two-dimensional electron gas, *Phys. Rev. Lett.* **60**, 848 (1988).
- [201] Y. Meir, N. S. Wingreen, and P. A. Lee, Low-temperature transport through a quantum dot: The Anderson model out of equilibrium, *Phys. Rev. Lett.* **70**, 2601 (1993).
- [202] J. Friedel, XIV. The distribution of electrons round impurities in monovalent metals, *Philos. Mag.* **43**, 153 (1952).
- [203] J. S. Langer and V. Ambegaokar, Friedel sum rule for a system of interacting electrons, *Phys. Rev.* **121**, 1090 (1961).
- [204] D. C. Langreth, Friedel sum rule for Anderson's model of localized impurity states, *Phys. Rev.* **150**, 516 (1966).
- [205] D. Becker, S. Weiss, M. Thorwart, and D. Pfannkuche, Non-equilibrium quantum dynamics of the magnetic Anderson model, *New J. Phys.* **14**, 073049 (2012).
- [206] C. H. Mak and R. Egger, A multilevel blocking approach to the sign problem in real-time quantum Monte Carlo simulations, *J. Chem. Phys.* **110**, 12 (1999).
- [207] R. Egger, L. Mühlbacher, and C. H. Mak, Path-integral Monte Carlo simulations without the sign problem: Multilevel blocking approach for effective actions, *Phys. Rev. E* **61**, 5961 (2000).
- [208] L. Mühlbacher and R. Egger, Crossover from nonadiabatic to adiabatic electron transfer reactions: Multilevel blocking Monte Carlo simulations, *J. Chem. Phys.* **118**, 179 (2003).
- [209] P. Werner, T. Oka, and A. J. Millis, Diagrammatic Monte Carlo simulation of nonequilibrium systems, *Phys. Rev. B* **79**, 035320 (2009).
- [210] J. Boyd, *Chebyshev and Fourier spectral methods*, Dover Publ Inc, 2003.

## Bibliography

- [211] E. Hairer and G. Wanner, *Solving ordinary differential equations. I. Stiff and differential-algebraic problems*, Springer, Heidelberg, New York, 2008.
- [212] E. Hairer and G. Wanner, *Solving ordinary differential equations. II. Stiff and differential-algebraic problems*, Springer, Heidelberg, New York, 2010.
- [213] C. W. Misner, K. S. Thorne, and J. A. Wheeler, *Gravitation*, Freeman, San Francisco, 1973.

# Danksagung

Im Laufe der letzten Jahre haben viele Menschen einen Beitrag dazu geleistet, dass diese Arbeit nun endlich in Druck geht. Zuallererst möchte ich mich bei meinem Betreuer Thomas Gasenzer bedanken für seine Betreuung und sein Vertrauen mir dieses spannende aber auch sehr herausfordernde Thema angeboten zu haben. Ebenso möchte ich mich bei Selim Jochim für die Zweitbegutachtung dieser Arbeit bedanken. Darüber hinaus bedanke ich mich bei den weiteren Prüfern Michael G. Schmidt und Werner Aeschbach-Hertig.

Einen wichtigen Beitrag zum Voranbringen dieses Projektes hat Alexander Liashvili geleistet, während er seine Masterarbeit bei uns in der Arbeitsgruppe anfertigte. Danke für die perfekte Zusammenarbeit!

Ganz besonders möchte ich mich bei dem unermüdlichen Bartholomew Andrews bedanken für sein ständiges Lesen und sprachliches Verbessern und auch für die gemeinsame Zeit während seines Aufenthalts in Heidelberg.

Ich bedanke mich vielmals bei Markus Karl, Boris Nowak, Steven Mathey, Tilman Enss, Henning Soller, Isara Chantesana, Andreas Samberg und Matthias Kronenwett für ihre Korrekturen und Anregungen, wodurch diese Arbeit erheblich verbessert wurde.

Des Weiteren bedanke ich mich bei den noch unerwähnten jetzigen wie auch ehemaligen Kollegen Sebastian Erne, Enrico Brehm, Konrad Schade, Martin Trappe, Roman Hennig, Jan Schole, Jan Zill, Nicolai Philip, Cedric Bodet, Simon Sailer und Thorge Müller. Alle bisher genannten Kollegen haben mit ihrer Freundlichkeit und Solidarität ein Arbeitsklima entstehen lassen, das seinesgleichen sucht. Man hat sich gegenseitig weitergeholfen auch wenn man selbst in Zeitnot war. Durch gemeinsame Aktivitäten außerhalb des Instituts haben sich manche Freundschaften entwickelt, die ich nicht mehr missen möchte. Vielen Dank dafür!

Ich bedanke mich vielmals bei der Landesgraduiertenförderung und dem Institut für Theoretische Physik der Universität Heidelberg für die finanzielle Unterstützung. Ebenso gilt mein Dank dem Sekretariat des Instituts für die Hilfe und Unterstützung bei allen bürokratischen Angelegenheiten.

Zu guter Letzt geht kein Weg daran vorbei, meine Familie hervorzuheben, die immer bedingungslos hinter mir stand und mich immer unterstützt hat, und auch vor allem in schwierigen Zeiten und die gab es während der letzten Jahre mehr als genug. Vielen Dank für all eure Hilfe und Unterstützung! Abschließend möchte ich mich bei meiner wunderbaren Frau Hui Sun bedanken. Du hast mir durch deine Zuneigung und Wärme immer wieder neue Energie gegeben, um diese Arbeit weiter voranzubringen und mich in schweren Zeiten ermuntert, meine Ziele nicht aus den Augen zu verlieren. Danke, dass du stets an meiner Seite bist!